



universität  
wien

# DIPLOMARBEIT

Titel der Diplomarbeit

Lattice Boltzmann Simulation of Nucleation in Binary Fluids

angestrebter akademischer Grad

Magister/Magistra der Naturwissenschaften (Mag. rer.nat.)

|                                     |  |
|-------------------------------------|--|
| Verfasserin / Verfasser:            | Carina Natalia Karner                  |
| Matrikel-Nummer:                    | a0504714                               |
| Studienrichtung (lt. Studienblatt): | Diplomstudium Physik 411               |
| Betreuerin / Betreuer:              | Univ. Prof. Mag. Dr. Christoph Dellago |

Wien, am 13.5.2011

---

# Contents

|          |  |           |
|----------|--|-----------|
| <b>1</b> | <b>Introduction</b>  | <b>5</b>  |
| <b>2</b> | <b>Spinodal Decomposition and Nucleation in Binary Fluids</b>                            | <b>7</b>  |
| 2.1      | Introduction to the Theory of Phase Transitions . . . . .                                | 7         |
| 2.1.1    | Ginzburg-Landau Theory . . . . .   | 14        |
| 2.2      | Introduction to Nucleation Theory . . . . .  | 18        |
| 2.2.1    | Cluster Dynamics . . . . .   | 19        |
| 2.2.2    | Classical Nucleation Theory . . . . .  | 20        |
| 2.2.3    | Concepts beyond Classical Nucleation Theory . . . . .                                    | 24        |
| 2.3      | Landau theory of Spinodal Decomposition and Nucleation . . .                             | 25        |
| 2.3.1    | Cahn-Hilliard equation . . . . .   | 25        |
| 2.3.2    | Predictions and Performance of the Cahn Hilliard Theory                                  | 27        |
| <b>3</b> | <b>The Lattice Boltzmann Method</b>  | <b>31</b> |
| 3.1      | The Boltzmann Equation . . . . .   | 32        |
| 3.1.1    | Derivation of the Boltzmann equation . . . . .   | 32        |
| 3.1.2    | Moments of the Distribution Function . . . . .   | 36        |
| 3.1.3    | Maxwellian Equilibrium Distribution . . . . .  | 36        |
| 3.1.4    | The H-Theorem . . . . .  | 37        |
| 3.1.5    | Relaxation Time Approximation . . . . .  | 38        |
| 3.2      | The Lattice Boltzmann Equation . . . . .   | 39        |
| 3.2.1    | The Lattice . . . . .  | 40        |
| 3.2.2    | Moments of the Distribution Function . . . . .   | 41        |
| 3.2.3    | The Structure of the Lattice Boltzmann Equation: Col-<br>lisions and Streaming . . . . . | 42        |
| 3.2.4    | Chapman Enskog Expansion: From Lattice Boltzmann<br>to Navier-Stokes . . . . .           | 42        |
| 3.3      | Modelling Lattice Boltzmann . . . . .  | 45        |
| 3.3.1    | The Kinetic Equation and the Lattice . . . . .   | 45        |
| 3.3.2    | Derivation of the Equilibrium Distribution . . . . .                                     | 45        |
| 3.3.3    | Boundary Conditions . . . . .  | 47        |

|          |   |           |
|----------|---|-----------|
| 3.3.4    | Implementation . . . . .  | 49        |
| 3.4      | Fluctuating Lattice Boltzmann Method . . . . .                                  | 50        |
| 3.4.1    | Multi-Relaxation-Time Model (MRT) . . . . .                                     | 50        |
| 3.4.2    | Introduction of Fluctuations . . . . .  | 52        |
| <b>4</b> | <b>Simulation and Results</b>   | <b>55</b> |
| 4.1      | Deterministic Lattice Boltzmann Model for Binary Fluids . . . .                 | 55        |
| 4.2      | Validity of the Deterministic Model . . . . .                                   | 58        |
| 4.2.1    | Phase Behaviour . . . . .   | 58        |
| 4.2.2    | Influence of $\kappa$ . . . . .   | 62        |
| 4.2.3    | Structure Factor . . . . .  | 64        |
| 4.3      | Fluctuating Lattice Boltzmann Model for Binary Fluids . . . .                   | 67        |
| 4.4      | Analysis and Results . . . . .  | 68        |
| 4.4.1    | Cluster Analysis Tools . . . . .  | 68        |
| 4.4.2    | Influence of $\kappa$ on the Nucleation Process . . . . .                       | 70        |
| 4.4.3    | Influence of the Fluctuation Amplitude on the Nucle-<br>ation Process . . . . . | 78        |
| 4.5      | Summary . . . . .   | 84        |
| <b>A</b> | <b>Zusammenfassung</b>  | <b>87</b> |
| <b>B</b> | <b>Abstract</b>   | <b>89</b> |
| <b>C</b> | <b>Curriculum Vitae</b>   | <b>91</b> |



# Chapter 1

## Introduction

Condensed matter materials, which are composed of two different species of molecules, colloids or other entities, are widely known as binary materials. Binary alloys, binary colloids and water-oil-mixtures are prominent examples for this class of materials. In this thesis we deal with binary fluids that are miscible under certain temperatures and mole-fractions only. Beyond those temperatures and mole-fractions, these fluids will unmix.

This phase separation transition then proceeds either via spinodal decomposition or via nucleation. When undergoing spinodal decomposition, the binary fluid exhibits a characteristic coarsening behaviour. Shortly after the finite temperature quench from the mixed state, distinct domains of the different species form. After this initial phase separation, the domains start to grow until, the fluid is fully phase separated.

On the other hand, when undergoing a nucleation process, a free energy barrier separates the actual state of the fluid from the phase separated equilibrium state. We observe that, due to thermal fluctuations, small droplets of the species with the minor mole-fraction appear now and then. Most of them will vanish again. Only if one droplet manages to cross the free energy barrier, it starts to grow until the fluid is separated.

The aim of this thesis is to model the nucleation process of a binary fluid with the lattice Boltzmann method. As starting point we use the lattice Boltzmann model of a binary fluid of ref. [54]. Since nucleation is a fluctuation induced process, thermal fluctuations need to be included into the binary fluid model. This is done by implementing the fluctuating lattice Boltzmann algorithm introduced by ref. [20]. As the lattice Boltzmann method is a mesoscopic method for modelling fluid flow and nucleation is a microscopic process, it is not obvious that nucleation can be observed in our model. So, we examined our results thoroughly, in order to show that nucleation can be modelled via lattice Boltzmann.

This thesis is organised as follows: Chapter 2 concentrates on reviewing the physical aspects of the problem. We start with summarizing the theory of phase transitions and then move on to review classical nucleation theory. In the last part of this chapter, we introduce the Ginzburg-Landau theory of spinodal decomposition and nucleation.

In Chapter 3 the lattice Boltzmann method is reviewed.

In Chapter 4, we finally present the details of the simulation, the results and the interpretation of the results.

## Chapter 2

# Spinodal Decomposition and Nucleation in Binary Fluids

In the following section, we review the theory of phase transitions. After that, we present methods and results of classical nucleation theory and in the last part of this chapter we introduce the Ginzburg-Landau theory of spinodal decomposition and nucleation.

### 2.1 Introduction to the Theory of Phase Transitions

In nature, materials usually appear in more than one phase. Which phase a material takes on depends on external conditions such as temperature, pressure and electrical or magnetic fields. Temperature, for example, controls whether water appears as water steam, as liquid water or as ice. Yet, the physics of phase transitions distinguishes between a lot more phases than just the aggregate phases, solid, liquid and gaseous. Examples are the ferromagnetic transition, where a paramagnetic material transforms into a ferromagnetic one when cooled under the Curie temperature, the conductor-superconductor transition and the phase separation of binary fluids.

The theory of phase transitions tries to find a common framework that is capable of describing all those different types of phase transitions. Basic concepts of the theory of phase transitions are the phase diagram, the order parameter and the classification of phase transitions.

The main literature sources for this section are [8, 50, 35, 7].

**Classification of Phase Transitions** An early attempt to classify phase transitions dates back to Paul Ehrenfest [21]. According to this formalism

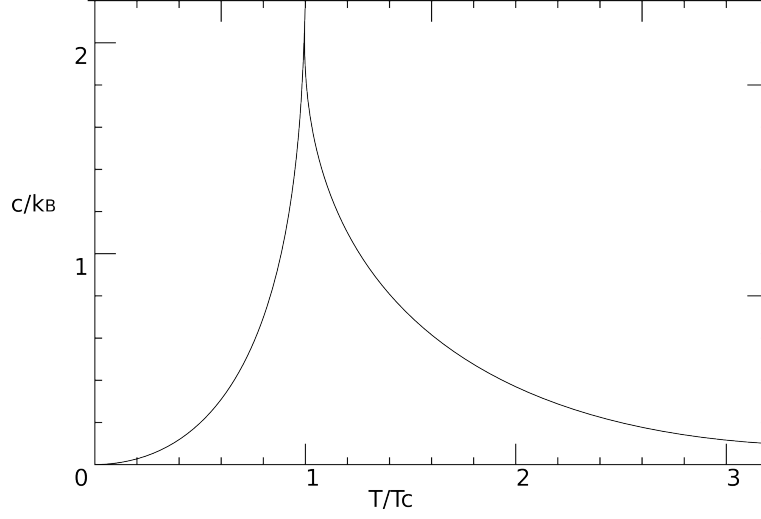


Figure 2.1: The specific heat  $c$  of a two-dimensional Ising model diverges at  $T = T_c$

a phase transitions is of order  $n$  if the  $n^{th}$  derivative of a thermodynamic potential after a control parameter is discontinuous, while all derivatives of order  $m < n$  are continuous.

Unfortunately, the Ehrenfest classification has got a loophole: Many of the so called second order phase transitions do actually diverge but do not show a discontinuity

As illustration [8], consider the two dimensional Ising ferromagnet. By applying transfer matrix methods, we find that the specific heat  $c_B = -\beta^2 \frac{\partial^2 \mu}{\partial \beta^2}$  of the Ising model diverges at  $T \rightarrow T_c$ , but does not show a discontinuity at  $T = T_c$  (see figure 2.1).

A more recent approach classifies transitions to be of first order if the phase change process either releases or absorbs latent heat [35]. A system is said to absorb latent heat if an addition of energy does not lead to a temperature change, thus the added energy is used for structural changes. In this approach, all other Ehrenfest-types of phase transitions are called "continuous" phase transitions.

**Order Parameter** An order parameter is an observable that distinguishes between the different phases of a system. For every phase it takes on a typical value. So by measuring the order parameter we can tell in which phase the system is. The order parameter can be of scalar, vector or even tensor form [7]. Since there is no recipe for finding them, we need to define valid order parameters for every new system afresh. In addition, note that an or-

---

| Transition                           | Order Parameter                                      |
|--------------------------------------|--|
| demixing of a binary fluid           | density difference: $\phi = \rho_A - \rho_B$         |
| He-I-He-II                           | Bose-Einstein condensate wave function $\phi = \Phi$ |
| ferromagnetic transition in solids   | spontaneous magnetization: $\vec{\phi} = \vec{M}$    |
| conductor-superconductor transition  | polarization $\vec{\phi} = \vec{P}$                  |
| ferro electrical transition          | Cooper-pair amplitude: $\phi = \Delta$               |
| elastic phase transitions            | deformation $\phi = \epsilon$                        |
| liquid-solid melting/crystallisation | reciprocal lattice vector: $\vec{\phi} = \vec{G}$    |

Table 2.1: Examples for order parameters and phase transitions, table partly taken from ([50], p.340).

der parameter need not be unique. Sometimes there are many different valid order parameters for one system [7].

Examples for order parameters are the reciprocal lattice vector in melting or crystallization transition, the spontaneous magnetization in the ferromagnetic transition and the density difference in binary fluids. For more examples, see the table above.

**Phase Diagram** We already know that a change in external parameters may yield a phase change. Therefore, we are interested in the phase limiting curves. These curves, which are dependent on a pair or even a triple of control parameters, separate regions of different phases. At a phase limiting curve, the adjacent phases are in coexistence [50]. The resulting diagram is called phase diagram. See figures 2.3 and 2.2 for illustration.

**Example 1: Liquid-Gas Transition in Water** The order parameter of the liquid-gas transition is given by

$$\phi(\vec{x}) = \rho(\vec{x}) - \rho_{gas}(\vec{x}). \quad (2.1)$$

This is a scalar density difference field, where  $\rho(\vec{x})$  is the actual density field of the system while  $\rho_{gas}(\vec{x})$  is the corresponding density of gas at the temperature and pressure at the point  $\vec{x}$ . Note that  $\rho(\vec{x})$  is a fluctuating

quantity whose time average tends to zero for every point  $\vec{x}$  as the phase limiting curve is approached [8].

To gather more information on the gas-liquid phase transition of water we

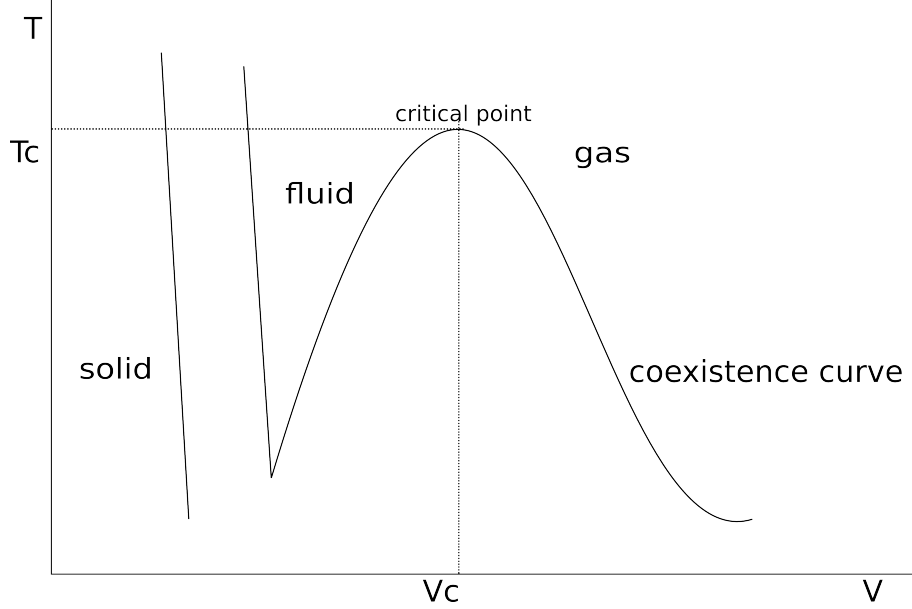


Figure 2.2: The pressure-volume phase diagram of water

take a look at the pressure-temperature phase diagram (figure 2.3). Besides the phase coexistence curves we notice the so called triple point and the critical point. At the triple point all three phases are in coexistence. Below the critical point, latent heat is absorbed during the transition and therefore the transition is first order. At critical point however, the latent heat absorption is zero (see figure 2.4) and the liquid-gas transition becomes a continuous phase transition [8].

**Example 2: Phase Separation of a Symmetric Binary Fluid** Now we take a first look at the system we will focus throughout the whole thesis: binary fluids which are only miscible under certain combinations of temperatures and mole-fractions. The order parameter of such binary fluid systems is given by the density difference between fluid A and fluid B [5, 7]:

$$\phi(\vec{x}) = \rho_A(\vec{x}) - \rho_B(\vec{x}). \quad (2.2)$$

We begin with the special case where the fluid mixture contains an equal amount of fluid A and fluid B. Then, the order parameter is zero on the space average and a temperature quench will result in a second order phase

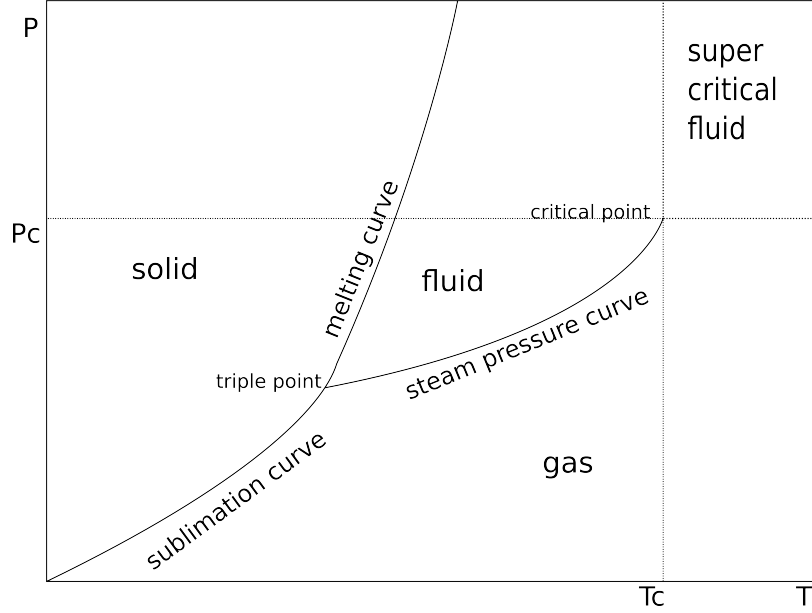


Figure 2.3: The pressure-temperature phase diagram of water

transition. In contrast, crossing the coexistence line when the space averaged density difference is not zero will lead to a first order phase transition. In both cases, in the course of the phase transition, the order parameter will take on the positive values at volume elements where fluid A dominates and negative values at points mainly occupied by fluid B.

The phase diagram in figure 2.5 shows two curves, where the outer line is called binodal and the inner line spinodal. If the liquid is cooled down between the binodal and the spinodal line, we observe phase separation via nucleation and if the liquid is cooled down below the spinodal line, the phase separation proceeds via spinodal decomposition [5, 7].

**Correlation Functions** In order to confirm the theory of phase transitions experimentally we need quantities that can also be measured in experiments. The two-point correlation function and the connected two-point correlation function are such quantities [8]. In the theory of phase transitions the two point correlation function is defined as the scalar product of the order parameter at a reference point  $\vec{x}$  and at the point  $\vec{x} + \vec{s}$

$$G^{(2)}(\vec{x} + \vec{s}) = \langle \phi(\vec{x}), \phi(\vec{x} + \vec{s}) \rangle. \quad (2.3)$$

The two-point correlation function measures the agreement of the order parameter between two points. Experimentally the correlation function is obtained by scattering measurements. The scattered particles could be photons,

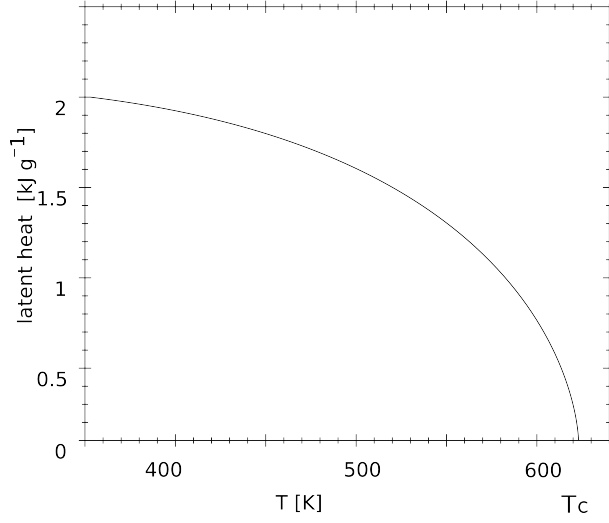


Figure 2.4: Latent heat of water as function of temperature. In this plot one can observe how the latent goes to zero as the critical point is approached. At the critical point the latent heat vanishes completely.

phonons, neutrons or electrons. In addition to the two-point correlation function we also define the connected two-point correlation function as

$$G_c^{(2)}(\vec{x} + \vec{s}) = \langle \phi(\vec{x}), \phi(\vec{x} + \vec{s}) \rangle - |\langle \phi(\vec{x} + \vec{s}) \rangle|^2. \quad (2.4)$$

Above  $T_c$ ,  $G_c^{(2)}$  is equal to  $G^{(2)}$  since  $\langle \phi \rangle = 0$ . Below  $T_c$ , the connected two-point correlation function measures only the fluctuations in the order parameter. Since  $G^{(2)}$  becomes rather large below  $T_c$ , this definition of  $G_c^{(2)}$  is quite practicable.

**Universality, Critical Exponents and Scaling Invariance** Second order phase transitions exhibit a variety of interesting properties as universality, critical exponents and scaling invariance.

The systems we presented so far, have nothing in common as far as their microscopic structure is concerned. Yet near the critical point, their phase transitions share common features. In fact, experimental results indicate that the observables of apparently different systems can be described by the same power laws in the vicinity of the critical point. This observation is called universality [8].

In addition, we can group the systems into so called universality classes, where systems with same spatial and same order parameter dimensionality share one universality class. Having done so, we can make another interesting observation: According to further experiments, systems which are in the



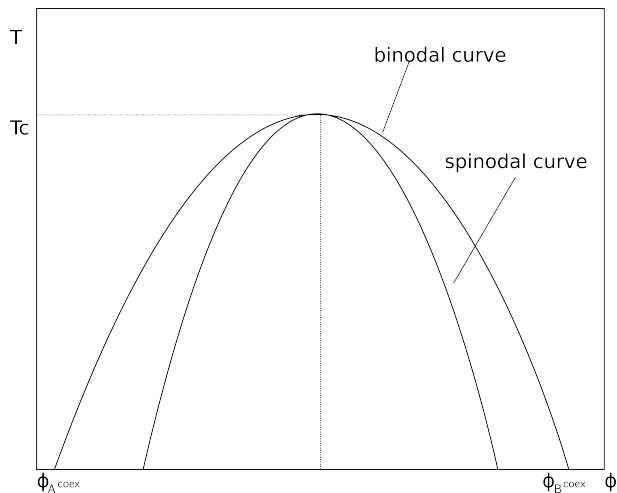


Figure 2.5: The temperature density-difference phase diagram of a symmetric binary fluid.

same universality class appear to have the same power law exponents, which are called critical exponents.

One explanation for this universal behaviour could be the large scale fluctuations of the order parameter near the critical point [8]. When the critical point is approached, those fluctuations diverge. To account for this phenomenological result, near to the critical point when  $0 \neq |T - T_c|/T_c \ll 1$  still holds, the two point correlation function is given by

$$G_c^{(2)} \approx \exp[-r/\xi], \quad (2.5)$$

where  $\xi$  is the correlation length. This relation for the two point correlation function tells us that the system regularly fluctuates up the length scale of  $\xi$ , whereas fluctuations larger than  $\xi$  rarely occur. When approaching the critical point the correlation length has been found to follow a power law

$$\xi \approx |T - T_c|^\nu. \quad (2.6)$$

where  $\nu$  approximately  $2/3$ . Subsequently at  $T = T_c$  the correlation length is infinite, which means, that there are fluctuations up to an infinite length scale. Due to those long scale fluctuations near the critical point microscopic details of the system become irrelevant as the only length scale that matters now is the one of the fluctuations [8].

Note that this is just a hand waving explanation and the phenomenon of universality is still far from understood. For one thing seems quite contradictory: Although the microscopic forces are the ones that drive the system

|                           | ferromagnet  | liquid   | critical behaviour   |
|---------------------------|--|--|--|
| order parameter           | $\vec{M}$  | $\rho_{gas,liq} - \rho_c$                                  | $(-\tau)^\beta$ at $T < T_c$                                       |
| isothermal susceptibility | $\chi_T = (\frac{\partial M}{\partial H})_T$             | $\kappa_T = \frac{1}{-V}(\frac{\partial V}{\partial P})_T$ | $\chi_T, \kappa_T \propto  \tau ^{-\gamma}$                        |
| specific heat             | $C_{H=0} = C_{B=0} = T(\frac{\partial S}{\partial T})_H$ | $C_V = T(\frac{\partial S}{\partial T})_V$                 | $C_{H=0}, C_{B=0} \propto  \tau ^{-\alpha}$<br>at $T \gtrless T_c$ |

Table 2.2: As one can see in this table, the critical exponents of a second order gas/liquid transition and a ferromagnetic transition are the same. Table taken from ([50], p.388)

to the phase transition, they seem to become irrelevant in the vicinity of the critical point.

Another observation made in second order phase transitions is scale invariance [8]. A quantity is called scale invariant, if it is invariant under the scaling transformation

$$m \rightarrow m\lambda, \quad (2.7)$$

where  $m$  is a physical property of the system and  $\lambda$  is a scaling factor. An example for scale invariance is the self similar domain growth in the ferromagnetic transition and in the spinodal decomposition of binary materials. In binary fluids, the pattern carved by the domains of the two components remains statistically the same during the phase transition. The only thing that changes is the length scale (see figure 2.6). Hence, the correlation function  $f$  of the order parameter is given by [61]

$$\langle \phi(\vec{x} + \vec{s}, t), \phi(\vec{x}, t) \rangle = f(\vec{s}/R(t)), \quad (2.8)$$

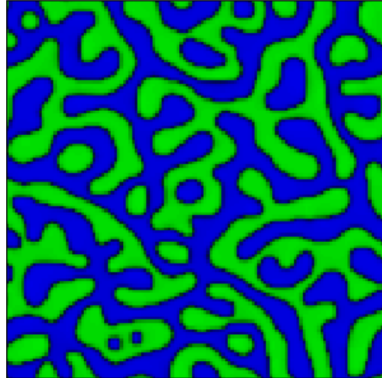
where  $R(t)$  is a typical length scale of the this system which grows according to a power law with an exponent  $\alpha$

$$R(t) \approx (t - t_0)^\alpha. \quad (2.9)$$

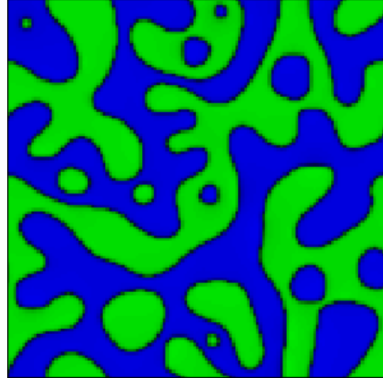
Note that for binary systems where hydrodynamics is important, like for example in binary fluids the scale invariance breaks down for late times, where hydrodynamic growth plays a role [61].

### 2.1.1 Ginzburg-Landau Theory

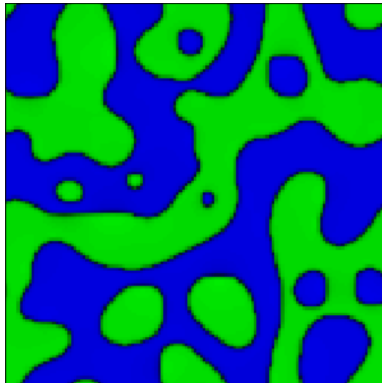
We already know that for describing the system behaviour near a critical point the microscopic details of the system are irrelevant. Hence we neglect



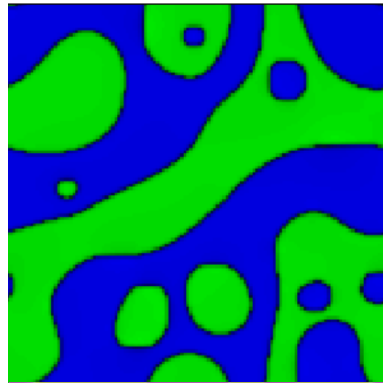
$t = 2000$



$t = 5000$



$t = 7000$



$t = 10000$

Figure 2.6: Scale invariance of a two-dimensional symmetric lattice-Boltzmann binary fluid. The critical exponent  $\alpha$  of this system is  $1/3$  for intermediate times  $t$ . For later times hydrodynamic flow becomes important and  $\alpha$  changes gradually to  $2/3$  resulting in a break-down of scale invariance [61]. For further simulation details, see chapter 4.

the microscopic structure and introduce continuous and averaged order parameters. So instead of for instance looking at the distribution of single water and gas molecules, we introduce a mean density difference by averaging over the water-gas distributions in a small  $D$ -dimensional volume [8].

**Ginzburg-Landau Functional** Recalling the ensemble concept of statistical mechanics, we introduce the probability functional  $\mathcal{P}[\phi_1(\vec{x})]$  that returns the probability that the order parameter  $\phi(\vec{x})$  has the special form  $\phi_1(\vec{x})$ . This probability functional is assumed to have the form [8]

$$\mathcal{P}[\phi(\vec{x})] \propto \exp[-\beta\mathcal{F}[\phi(\vec{x})]], \quad (2.10)$$

with  $\mathcal{F}[\phi(\vec{x})]$  as the Ginzburg-Landau free energy functional

$$\mathcal{F}[\phi(\vec{x})] = \mathcal{F}_0 + \int d^D x \left[ a\phi(\vec{x})^2 + \frac{1}{2}b\phi(\vec{x})^4 + c(\nabla\phi(\vec{x}))^2 - h(\vec{x})\phi(\vec{x}) \right], \quad (2.11)$$

where  $a, b, c$  with  $b, c > 0$  are coefficients,  $D$  is the dimension of the order parameter,  $\mathcal{F}_0$  is a constant and  $h(\vec{x})$  denotes an external field. Due to the form of the probability functional we conclude that the Ginzburg-Landau functional is a kind of coarse grained Hamilton function for the order parameter [8, 50]. Note that this form of the free energy functional results from a Taylor expansion. If necessary, more terms from the series expansion can be included to the functional.

Ginzburg-Landau functionals can be defined for various kinds of phase transitions. The form of the functional depends on the symmetry of the order parameter and has to be adapted for every system anew [7]. Using the probability functional we even can define a Ginzburg-Landau partition function:

$$Z = Z_0(T) \int \mathcal{D}[\phi(\vec{x})] \exp[-\beta\mathcal{F}[\phi(\vec{x})]], \quad (2.12)$$

where the expression  $\int \mathcal{D}[\phi(\vec{x})] \exp[-\beta\mathcal{F}[\phi(\vec{x})]]$  denotes the sum over all valid forms of  $\phi(\vec{x})$ , each multiplied by its weight  $\exp[-\beta\mathcal{F}[\phi(\vec{x})]]$ . The question which forms of  $\phi(\vec{x})$  are valid is discussed in ref. [8].

**Metastability and Instability** According to basic thermodynamics the equilibrium free energy  $\mathcal{F}(\phi)$  is a convex function of its order parameter  $\phi$  [7]. Taking a look at figure 2.7, we observe that the free energy functional of this plot exhibits two minima and therefore it is not a convex function of its order parameter. Since the given functional can not be the equilibrium free energy, we construct a new equilibrium free energy by connecting

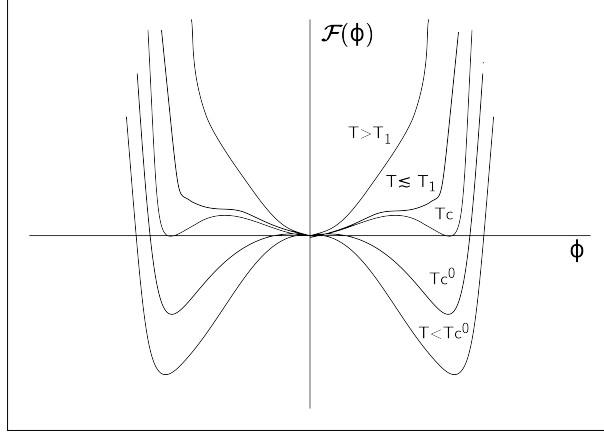


Figure 2.7: Ginzburg-Landau free energy functional of a first order phase transition for different temperatures  $T$ .  $T_1$  is the so called super heating temperature, i.e for temperatures  $T > T_1$ , there is only one minimum and the phase with  $\phi = 0$  is stable. For Temperatures  $T_1 \geq T > T_c$ , where  $T_c$  is the critical the phase with  $\phi = 0$  is metastable, whereas for phases with  $T_c > T \geq T_c^0$ , where  $T_c^0$  is the so called supercooling temperature, the phase with  $\phi \neq 0$  is metastable. For temperatures  $T < T_c^0$  the phase with  $\phi = 0$  becomes unstable. See [50] for detailed information.

the two minima. This procedure is called double-tangent construction. In the literature [7] everything lying above the new equilibrium free energy is interpreted as unstable or metastable branch of the free energy (see figure 2.8). To be precise, the part of this branch where  $\frac{\partial^2 \mathcal{F}}{\partial \phi^2} > 0$  is interpreted as the metastable region, whereas the part where  $\frac{\partial^2 \mathcal{F}}{\partial \phi^2} < 0$  is interpreted as the unstable region.

In Cahn-Hilliard theory, which will be introduced in section 2.3, an adapted Ginzburg-Landau free energy functional for binary fluids is used. Due to a temperature quench under the coexistence line the system is driven out of equilibrium and the free energy functional develops two minima and takes on a form similar to figure 2.7. Depending on the depth of the temperature quench the system is either pushed into the metastable or the unstable region. If quenched into the metastable region, the phase separation transition proceeds via nucleation and if quenched into the unstable region, the phase separation transition proceeds via spinodal decomposition [6].

**Ginzburg Criterion** We know that Ginzburg-Landau theory defines order parameters as averaged quantities of a system. Far away from the critical point, this approximation works out quite well. But when drawing closer to the critical point, fluctuations become more and more important. Since

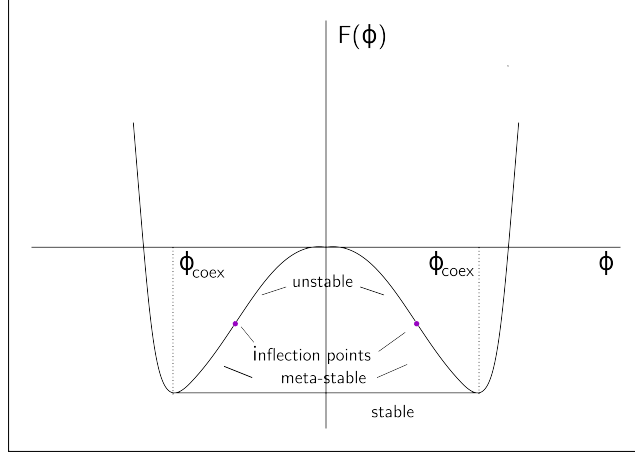


Figure 2.8: Free energy of a first order transition for a temperature  $T < T_c$ . The line connecting the coexistence values is the constructed stable branch of the free energy function, the part of  $F(\phi)$  lying above this line is then interpreted as the metastable and unstable branch. The region where  $\frac{\partial F}{\partial \phi} > 0$ , i.e. the region between the coexistence values  $\phi_{coex}$  and the inflection point is called metastable, whereas the region where  $\frac{\partial F}{\partial \phi} < 0$ , i.e. the region between the inflection points is called unstable.

fluctuations are not included in the Ginzburg-Landau theory, somewhere in the neighbourhood of the critical point the theory will break down [8]. The Ginzburg criterion tells us how near to the critical point Ginzburg-Landau theory is applicable. The criterion states that the theory is valid as long as the mean square of the critical fluctuations  $\delta\phi$  is smaller than equilibrium value of the squared order parameter  $\phi$ ,

$$\langle \delta\phi(\vec{x})^2 \rangle < \langle \phi(\vec{x})^2 \rangle. \quad (2.13)$$

Note that the question why this criterion is a good measure for the break down of the Ginzburg-Landau theory has been answered mathematically only in the framework of renormalization group theory [8].

## 2.2 Introduction to Nucleation Theory

We already know that, if we quench a system under the binodal but above the spinodal line, we will observe nucleation. According to experiments and renormalization group theory, nucleation is regarded to be a fluctuation induced first order phase transition [7]. We observe that, due to thermal fluctuations, small droplets will appear every now and then. Most of them will vanish again since between the metastable state and the stable phase separated state there is a free energy barrier. To overcome this barrier, a

---

sufficiently large, so called critical cluster is required. If one nucleus manages to cross the barrier, the metastable state decays and the system arrives at a stable state, where the free energy has a minimum again.

The main literature sources for this section are [42, 41, 7] for the cluster-dynamics subsection, [3, 7] for the subsection on classical nucleation theory, and [41] for the subsection on density functional methods.

### 2.2.1 Cluster Dynamics

First we are interested in how the clusters of the new phase grow or shrink. But, before writing down equations, we discuss the term "cluster". In nucleation theory literature, one finds many different cluster definitions. Reiss et al. for example [46], define a cluster of  $n$  atoms as a "spherical entity in which the  $n$  atoms are contained with the center of mass as center". The volume of this cluster is then proportional to  $n$ . For Stillinger [51] on the other hand a cluster "consists of all atoms lying within a certain distance  $r_c$  of at least one other atom in the cluster".

Now let us assume we observe a nucleating system. We choose one of the above cluster definitions and strive to formalize our observations. One way to do this is to introduce a cluster-rate equation. To simplify matters, we assume that the only way a cluster can grow or shrink is by gaining or losing a monomer, i.e. a single molecule. This means that coalescence, the process where droplets containing more than one molecule collide with each other, is neglected.

We introduce the rate equations [42]

$$\begin{aligned} \frac{\partial n(p, t)}{\partial t} &= \beta(p-1)n(p-1, t) - \gamma(p)n(p, t) \\ &\quad - \beta(p)n(p, t) + \gamma(p+1)n(p+1, t), \quad \text{for } p \geq 2, \end{aligned} \quad (2.14)$$

and

$$\frac{\partial n(1, t)}{\partial t} = -\beta(1)n(1, t) + \gamma(2)n(2, t) \quad \text{for } p = 1, \quad (2.15)$$

where  $n(p, t)$  is the number density of clusters of size  $p$  at the time  $t$ ,  $\beta(p)$  is the growth rate constant at which a nuclei with  $p$  particles gains another monomer and  $\gamma(p)$  is the shrink rate constant, the rate at which a nuclei with  $p$  particles loses one monomer. Note that this time-local rate equation describes a Markov process, since the change of the number density at time  $t + \delta t$ , only depends on the number density  $n(p, t)$  at time  $t$  and not on prior times. The fact that we use rate constants in the equations has one

side effect: the equation can only model nucleation events where there is no temperature change.

To proceed further, we introduce the flux  $J_+(p, t)$  and the flux  $J_-(p, t)$ , where  $J_+(p, t)$  is the net rate at which clusters with  $p$  particles grow to clusters with  $p + 1$  particles

$$J_+(p, t) = \beta(p)n(p, t) - \gamma(p+1)n(p+1, t), \quad (2.16)$$

and  $J_-(p, t)$  is the rate at which  $p$ -particle clusters shrink to  $p - 1$  particle clusters

$$J_-(p, t) = \beta(p-1)n(p-1, t) - \gamma(p)n(p, t). \quad (2.17)$$

We can write the rate equations in terms of  $J_-$  and  $J_+$ ,

$$\frac{\partial n(p, t)}{\partial t} = J_-(p, t) - J_+(p, t). \quad (2.18)$$

Now, we turn to the steady state case, where all fluxes have the same constant flux:

$$J_+(p, t) = J_-(p, t) = J = \text{const} \quad \forall p, t. \quad (2.19)$$

This flux constant is called nucleation rate. Applying a few mathematical tricks, we get the following expression for  $J$ :

$$J = n(1) \left( \sum_{p=1}^{\infty} \frac{1}{\beta(p)f(p)} \right)^{-1}, \quad (2.20)$$

with

$$f(p) = \prod_{j=1}^{p-1} \frac{\beta(j)}{\gamma(j+1)}. \quad (2.21)$$

### 2.2.2 Classical Nucleation Theory

Classical nucleation theory makes two big approximations [7]. The first one, also known as capillarity approximation assumes that droplets are macroscopic objects where the free energy consists of a volume and a surface term. In an isotropic system, the energy minimizing form is given by a sphere. Therefore the free energy barrier of a droplet as function of its radius  $R$  has the form [3]

$$\Delta F(R) = \frac{4\pi R^3}{3} \rho \Delta \mu + 4\pi R^2 \gamma, \quad (2.22)$$

where  $\Delta \mu < 0$  is the difference in the chemical potential between the old equilibrium phase and the new metastable one and  $\gamma$  is the surface tension of



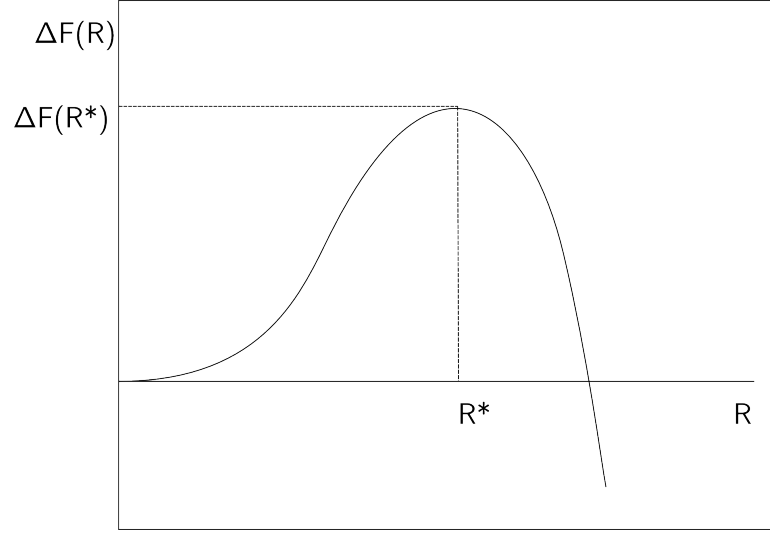


Figure 2.9: schematic plot of the free energy barrier  $\Delta F(R)$  as function of the cluster radius  $R$  within classical nucleation theory.  $R^*$  denotes the size of critical cluster and  $\Delta F(R^*)$  the height of the barrier.

a flat, planar and infinite two-phase interface. This surface tension approximation is the second big assumption of classical nucleation theory. Taking a closer look at the equation, we observe that for small droplets, the surface term wins over the volume term, whereas for large droplets the volume term wins over the surface term. Hence, small droplets can only grow via thermal fluctuations and therefore most of them will vanish again after some time. Only, if one droplet reaches the critical radius, the radius matching to the maximum of the free energy,

$$\max[\Delta F(R)] = \Delta F(R^*) = \frac{16\pi}{3} \frac{\gamma^3}{\Delta\mu^2}, \quad \text{where } R^* = \frac{-2\gamma}{\Delta\mu}, \quad (2.23)$$

it will grow due to the volume term of the free energy and the metastable state will decay to a new equilibrium.

**Nucleation Rate** Now, we derive the nucleation rate in the framework of classical nucleation theory (see refs. [7, 42]). We start again from the rate equation for  $p \geq 2$

$$\begin{aligned} \frac{\partial n(p, t)}{\partial t} &= \beta(p-1)n(p-1, t) - \gamma(p)n(p, t) \\ &\quad - \beta(p)n(p, t) + \gamma(p+1)n(p+1, t). \end{aligned} \quad (2.24)$$

We turn to the thermal equilibrium situation, where we assume detailed balance holds between growth and shrinking, i.e

$$\beta(p)n^{eq}(p) = \gamma(p+1)n^{eq}(p+1) \equiv \Omega(p, 1), \quad (2.25)$$

where  $n^{eq}$  denotes the equilibrium number density. We see that in thermal equilibrium we only need one rate constant  $\Omega(p, p+1)$ . The rate equation for  $p \geq 2$  in terms of the new rate constant is given by

$$\begin{aligned} \frac{\partial n(p, t)}{\partial t} &= \Omega(p-1, 1) \left( \frac{n(p-1, t)}{n^{eq}(p-1)} - \frac{n(p, t)}{n^{eq}(p)} \right) \\ &+ \Omega(p, 1) \left( \frac{n(p+1, t)}{n^{eq}(p)} - \frac{n(p, t)}{n^{eq}(p)} \right). \end{aligned} \quad (2.26)$$

In the next step we divide by  $n^{eq}$  and Taylor expand this expression around  $n(p, t)$  up to second order

$$\frac{n(p+1, t)}{n^{eq}(p+1)} = \frac{n(p, t)}{n^{eq}(p)} + \frac{\partial}{\partial p} \left( \frac{n(p, t)}{n^{eq}(p)} \right) + \frac{1}{2} \frac{\partial^2}{\partial p^2} \left( \frac{n(p, t)}{n^{eq}(p)} \right), \quad (2.27)$$

$$\frac{n(p-1, t)}{n^{eq}(p-1)} = \frac{n(p, t)}{n^{eq}(p)} - \frac{\partial}{\partial p} \left( \frac{n(p, t)}{n^{eq}(p)} \right) + \frac{1}{2} \frac{\partial^2}{\partial p^2} \left( \frac{n(p, t)}{n^{eq}(p)} \right). \quad (2.28)$$

We also do a Taylor expansion around  $\Omega$  up to first order

$$\Omega(p-1, 1) = \Omega(p, 1) - \frac{\partial}{\partial p} \Omega(p, 1) \quad (2.29)$$

Combining the last six equations we get the following partial differential equation

$$\frac{\partial n(p, t)}{\partial t} = \frac{\partial}{\partial p} \left[ \Omega(p, 1) \frac{\partial}{\partial p} \left( \frac{n(p, t)}{n^{eq}(p)} \right) \right] \equiv -\frac{\partial}{\partial p} J(p), \quad (2.30)$$

where  $J(p)$  is again the cluster flux. Note that this equation has the form of a continuity equation. To proceed further, we use droplet model of Fisher in order to get an expression for  $n(p)^{eq}$ :

$$n(p)^{eq} = n_0 \exp \left( \frac{-\Delta F_p}{k_B T} \right), \quad (2.31)$$

where  $\Delta F(p)$  is the free energy as function of the cluster size. In ref. [7] a more general rate equation is given, which is also able to describe coalescence

---

of clusters. They introduce a reaction rate  $D(p)$  that can be viewed as generalized rate constant,

$$D(p) = \frac{1}{n^{eq}} \sum_{p'} p'^2 \Omega(p, p'). \quad (2.32)$$

The continuity equations then changes to

$$\begin{aligned} \frac{\partial n(p, t)}{\partial t} &= \frac{\partial}{\partial p} \left[ n^{eq}(p) R(p) \frac{\partial}{\partial p} \left( \frac{n(p, t)}{n^{eq}(p)} \right) \right] \\ &= \frac{\partial}{\partial p} \left[ R(p) \frac{\partial n(p, t)}{\partial p} - \frac{\partial}{\partial p} \left( \frac{\Delta F(p)}{k_B T} \right) R(p) n(p, t) \right]. \end{aligned} \quad (2.33)$$

From equations 2.30 and 2.33 a nucleation rate can be calculated,

$$J = \rho D(p^*) \left( -\frac{1}{2\pi k_B T} \frac{d^2 \Delta F}{dp^2} \Big|_{p^*} \right)^{1/2} \exp \left( -\frac{\Delta F^*}{k_B T} \right), \quad (2.34)$$

where  $k_B$  denotes the Boltzmann constant and  $\rho$  is the fluid density. The factor before the exponential function is often given as  $J_0$  and is called Arrhenius factor,

$$J_0 = \rho D(p^*) \left( -\frac{1}{2\pi k_B T} \frac{d^2 \Delta F}{dp^2} \Big|_{p^*} \right)^{1/2}. \quad (2.35)$$

**Criticism** Although Classical nucleation theory can give a qualitative explanation for the nucleation phenomenon, its predictions often don't match with experimental results [29]. For example, the nucleation rates calculated within classical nucleation theory are much smaller than nucleation rates obtained by experimental measurements [30, 29]. What is more, for many systems classical nucleation theory predicts lower critical supersaturations than experiments at high temperatures, while it predicts higher critical supersaturations than experiments at low temperatures [48, 27, 62, 52, 43]. Only the size of the critical nucleus agrees with experimental findings [29, 57]. Note in this context, that although simulation and density functional theory yield a better overall agreement with experiment, there are still orders of magnitude between simulation and density functional theory results compared to experimental data [30].

One reason for the discrepancies between experiment and the classical nucleation theory are the rather coarse approximations classical theory makes [7]. First of all, classical nucleation theory treats clusters as macroscopic objects by assigning macroscopic quantities such as a surface tension or a bulk free

energy to them. These macroscopic concepts are applicable for large clusters, but for small clusters those assumptions break down as clusters with 30 atoms or molecules can't be described as macroscopic objects. Furthermore, in the classical equation for the free energy we use the surface tension of a flat interface  $\gamma$ . This may be a good approximation for large clusters with a weak curvature, but it is certainly not a good one for small clusters with a strong curvature.

### 2.2.3 Concepts beyond Classical Nucleation Theory

Due to the mentioned shortcomings of classical nucleation theory, in recent years, various improvements to the classical theory and also new theoretical approaches have been suggested. Since it would go beyond the scope of this thesis to review the whole literature on nucleation theory and simulation, we just stick to one example from theory. But note that there are successful computer simulation techniques that go beyond classical nucleation theory, like for example umbrella sampling [56] and transition path sampling [10].

**Density Functional Methods** In the density functional approach to nucleation theory the free energy is a functional  $\mathcal{F}[\rho(\vec{x})]$  that depends on a density field  $\rho(\vec{x})$  [42]. Density functional methods are not fully microscopic but are able to capture mesoscopic processes. In contrast to classical nucleation theory, the density of the nuclei can now differ from its bulk density. In addition, instead of taking the value of the surface tension of planar interface, within density functional theory we can take account of the curvature of the nuclei. We can calculate the density field of the critical nuclei  $\rho^*(\vec{x})$  by taking the functional derivative :

$$\frac{\delta \mathcal{F}[\rho(\vec{x})]}{\delta \phi} = 0, \quad \text{at } \rho(\vec{x}) = \rho^*(\vec{x}). \quad (2.36)$$

From  $\rho^*$  we can easily obtain  $\mathcal{F}[\rho^*(\vec{x})]$  and successively we can calculate the nucleation rate

$$J = J_0 \exp[-\Delta \mathcal{F}[\rho^*]/k_B T], \quad (2.37)$$

where the Arrhenius factor  $J_0$  is the same as in classical nucleation theory. The oldest density functional theory is the Cahn-Hilliard Theory [13, 12, 14] which we will discuss in the next section. For more recent works on density functional theory, take a look at [55, 41, 42, 39].

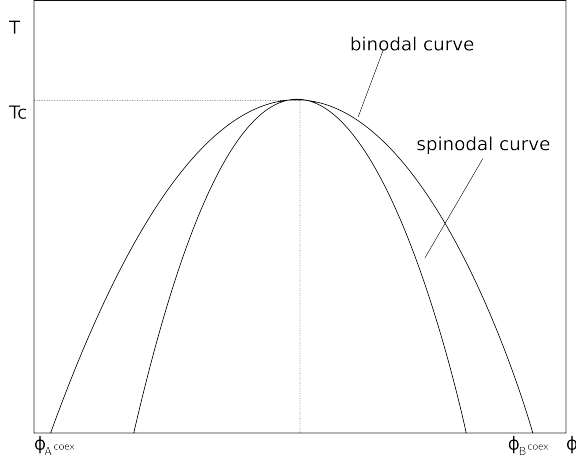


Figure 2.10: The Phase diagram of a binary fluid

## 2.3 Landau theory of Spinodal Decomposition and Nucleation

In this section we present Cahn-Hilliard theory of spinodal decomposition and nucleation in binary fluids. In the early 1960's Cahn and Hilliard [13, 12, 14] introduced a Ginzburg-Landau free energy functional for non-uniform systems and thereby derived an evolution equation for spinodal decomposition and nucleation. Since a Cahn-Hilliard model is used for the lattice Boltzmann model in this thesis, we will go into detail here. The main literature sources for this section are [13, 7, 6, 5, 14].

### 2.3.1 Cahn-Hilliard equation

Cahn and Hilliard assumed that the free energy functional of a non-uniform system has the following form:

$$\mathcal{F}[\phi(\vec{x}, t)] = \int d^3x f_0[\phi(\vec{x}, t)] + \kappa[\nabla\phi(\vec{x}, t)]^2, \quad (2.38)$$

where  $\mathcal{F}[\phi]$  denotes the free energy functional of the inhomogeneous system in non-equilibrium,  $f_0[\phi]$  is the free energy density of the homogeneous system in equilibrium,  $\kappa$  stands for a continuous function of the concentration-gradient and  $\phi(\vec{x}, t)$  denotes the density difference field. The special form of the free energy functional is motivated by the idea that the local free energy density of an inhomogeneous systems is composed of the local concentration plus the concentration of the nearer environment [13]. Note that the square

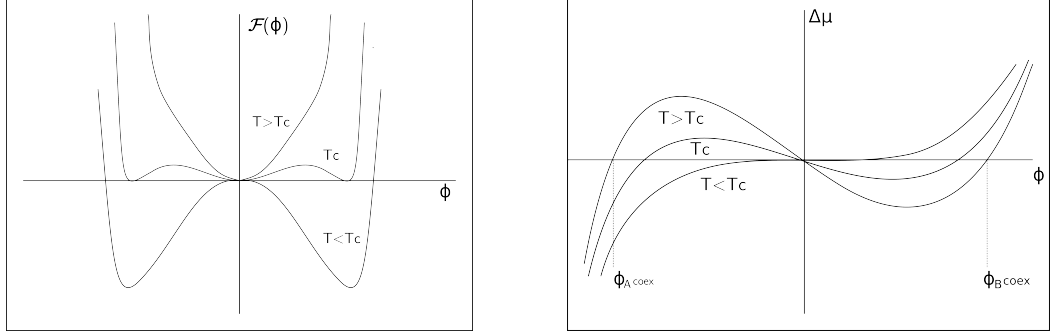


Figure 2.11: The free energy functional (on the left) and the chemical potential (on the right) of a binary fluid as function of the order parameter  $\phi$ .

gradient term is a good approximation for system where the equilibrium density difference between fluid A and fluid B is not too high. Models that allow high density difference are introduced in refs. [41, 42]. The chemical potential  $\mu(\vec{r})$  follows from a functional derivative in the usual way:

$$\mu(\vec{x}) = \frac{\delta \mathcal{F}}{\delta \phi(\vec{x}, t)} = \left( \frac{\partial f(\phi(\vec{x}, t))}{\partial \phi(\vec{x}, t)} \right)_T - \kappa \nabla^2 \phi(\vec{x}, t) \quad (2.39)$$

Furthermore, the the density difference is conserved in the Volume V,

$$\frac{1}{V} \int_V \phi(\vec{x}, t) d^3x = \text{const.} \quad (2.40)$$

This leads to a continuity equation with a concentration current  $\vec{j}$

$$\frac{\partial \phi(\vec{x}, t)}{\partial t} + \nabla \cdot \vec{j}(\vec{x}, t) = 0, \quad (2.41)$$

which is given by

$$\vec{j}(\vec{x}, t) = -\Gamma \nabla \mu(\vec{x}), \quad (2.42)$$

where the mobility  $\Gamma$  is a diffusion coefficient. Note, that in most applications  $\Gamma$  set to be constant. If we combine equations 2.41 and 2.42 we get

$$\frac{\partial \phi(\vec{x}, t)}{\partial t} = \Gamma \nabla^2 \mu(\vec{x}). \quad (2.43)$$

Inserting the functional derivative expression for the chemical potential, we finally arrive at the Cahn-Hilliard equation,

$$\frac{\partial \phi(\vec{r}, t)}{\partial t} = \Gamma \nabla^2 \left[ \left( \frac{\partial f(\phi(\vec{x}, t))}{\partial \phi(\vec{x}, t)} \right)_T - \kappa \nabla^2 \phi(\vec{x}, t) \right]. \quad (2.44)$$

---

**Mathematical Properties** The Cahn-Hilliard equation is a partial differential equation that has the form of a continuity equation. Due to the non-linear term  $\left(\frac{\partial f(c(\vec{r},t))}{\partial c(\vec{r},t)}\right)_T$  and the fourth order term  $\Gamma\kappa\nabla^4\phi(\vec{r},t)$ , proving the global existence and finding an analytical solution are tough problems. Only in 1986 Elliot and Songmu [23] proved existence and uniqueness for one and two dimensional Cahn-Hilliard equations with a constant mobility and a polynomial as free energy density. Nowadays there exists proofs of existence and uniqueness for various Cahn-Hilliard-equation types [24, 9, 44, 34, 63]. But unfortunately there hasn't been found an analytical solution for the full non-linear problem of any of those Cahn-Hilliard equation types yet [37].

**Linear Cahn Hilliard Equation** There also exists a linearised version of the Cahn-Hilliard equation. To obtain this linearised equation we need to exchange  $\phi(\vec{x},t)$  with  $\delta\phi(\vec{x},t)$ , which is the deviation of  $\phi(\vec{x},t)$  from its average value  $\bar{\phi}$ , i.e  $\delta\phi(\vec{x},t) = \phi(\vec{x},t) - \bar{\phi}$ . We get

$$\frac{\partial\delta\phi}{\partial t} = \Gamma\nabla^2 \left[ \left( \frac{\partial f(\phi(\vec{x},t))}{\partial \phi(\vec{x},t)} \right)_T \Big|_{\phi=\bar{\phi}} - \kappa\nabla^2\phi(\vec{x},t) \right]. \quad (2.45)$$

The argumentation for this linearisation is that at early stages of the phase separating transition, the deviation of  $\phi(\vec{x},t)$  from its average  $\bar{\phi}$  is very small [7]. Note that for the linear Cahn Hilliard equation an analytical solution can be found.

### 2.3.2 Predictions and Performance of the Cahn Hilliard Theory

Since for the fully non-linear Cahn-Hilliard equation no analytical solution exists, there have been a lot of attempts to solve the Cahn-Hilliard equation numerically [4, 22, 17]. In addition analytical predictions about the behaviour of possible solutions have been made [38, 2, 7, 5, 6].

**Spinodal Decomposition** If phase separation proceeds via spinodal decomposition, the binary fluid exhibits a characteristic coarsening behaviour. Shortly after the finite quench from the mixed state into the spinodal region, distinct domains of fluid A and fluid B are already formed. After this initial phase separation, the domains start to grow, while the pattern carved by the domains remains statistically the same (for more details, see section 2.1).

In order to quantify this scaling behaviour the structure factor given by

$$S(\vec{k}, t) = \left\langle \left| \sum_{\vec{x}} \exp[i\vec{k}\vec{x}] \phi(\vec{x}, t) \right|^2 \right\rangle. \quad (2.46)$$

proves to be a useful tool. Monte-Carlo simulations of the Cahn-Hilliard equation [33] and various simulations with Ising models [7, 11, 32, 26] have been carried out and the structure factor has been calculated. Afterwards the structure factor  $S(\vec{x}, t)$  of these numerical systems has been compared to the structure factor of the linear Cahn-Hilliard equation with constant mobility and a quadratic polynomial as free energy density.

According to [7], linear theory predicts exponential growth of the structure factor

$$S(\vec{k}, t) = S(\vec{k}, 0) \exp[2\omega(\vec{k})t], \quad (2.47)$$

with a so called amplification factor  $\omega(\vec{k})$

$$\omega(\vec{k}) = -k_B T \Gamma k^2 \left( \frac{\partial f(\phi)}{\partial \phi} \right)_T \bigg|_{\phi=\bar{\phi}}. \quad (2.48)$$

Note that  $S(\vec{k}, 0)$  denotes the structure factor at the time  $t = 0$  before the quench. From equation 2.47 follows that fluctuations with wave vector  $\vec{k}$  grow exponentially with time if  $\omega(\vec{k}) > 0$  and decay exponentially with time if  $\omega(\vec{k}) < 0$ . In addition

$$S(\vec{k}, t) = \text{const}, \quad \text{for } \vec{k} \text{ with } \omega(\vec{k}) = 0, \quad (2.49)$$

holds.

In computer simulations, where models with short range interactions [11, 32] were used, the structure factor also grew with time as this reflects the coarsening behaviour of the fluid but the growth was slower compared to the predicted exponential growth. In addition no wave vector value  $\vec{k}$  has been found where  $S(\vec{k}, t) = \text{const}$  holds. On the other hand, simulations with long range interactions yielded a better agreement with linear theory as the structure factor growth in those simulations behaves at least at early times exponential [26].

**Nucleation** The free energy barrier in Cahn-Hilliard theory is given by [14]

$$\Delta\mathcal{F}[\phi(\vec{x})] = \int dV f(\phi(\vec{x})) - f(\phi(\vec{x} + \kappa(\nabla\phi(\vec{x})))^2, \quad (2.50)$$



---

where  $\bar{\phi}$  denotes the average density difference, which is also the initial density difference of the mixed state and therefore  $f(\bar{\phi})$  is the initial free energy density in the mixed state. As stated in the subsection 2.2.3 we can obtain the critical density field  $\phi^*(\vec{x})$  by taking the functional derivative

$$\frac{\delta \mathcal{F}[\phi(\vec{x})]}{\delta \phi} = 0, \quad \text{at } \phi(\vec{x}) = \phi^*(\vec{x}). \quad (2.51)$$

Near the coexistence curve, for isotropic systems and systems with cubic symmetry, Cahn-Hilliard Theory of nucleation coincides with classical nucleation theory [7, 14]. But as we quench further into the metastable region, the more Cahn-Hilliard theory differs from classical nucleation theory. For one thing, the free energy barrier decreases gradually and finally becomes zero as the spinodal is approached. In addition, when drawing nearer to the spinodal line the nucleus first decreases, approaches a minimum and then starts to grow again and at the spinodal the size of the critical nucleus reaches infinity. Furthermore, at the spinodal the order parameter values inside the critical nuclei barely differ from the order parameter values outside the nuclei [7, 14]. While the initial decreasing of the critical nucleus size is in agreement with the classical nucleation theory, the subsequent growth is not. Of course, physically the divergence of the size of the critical nucleus does not make any sense. To account for this break-down and other shortcomings of Cahn-Hilliard theory Binder suggested in ref. [6] to use an extended Ginzburg-Criterion to estimate the applicability of Cahn-Hilliard theory in the vicinity of the spinodal line.

**Ginzburg Criterion** The conventional Ginzburg criterion estimates how near to the critical point Landau theory is applicable [8]. For illustration we take a look at binary fluid models with logarithmic free energy densities

$$f[\phi] = T\phi \ln[\phi] + T(1 - \phi) \ln[1 - \phi] + 2T_c\phi(1 - \phi). \quad (2.52)$$

According to ref. [6] the conventional Ginzburg criterion for those models is given by

$$\lambda^D \left(1 - \frac{T}{T_c}\right)^{2-D/2} \gg 1, \quad (2.53)$$

where  $\lambda$  denotes the interaction range and  $D$  denotes the spatial dimension. As long as the left side is much bigger than one, the approximations made by Landau theory remain valid.

Then ref. [6] introduces a more generalized Ginzburg criterion that additionally tells how near to the spinodal line Cahn-Hilliard theory is valid. The

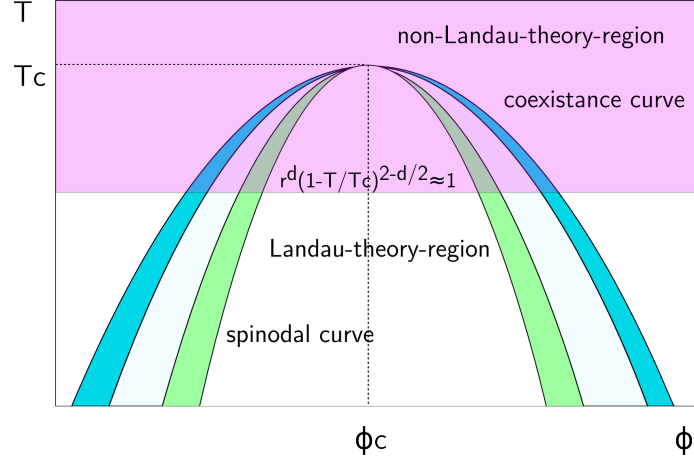


Figure 2.12: This is the phase diagram of a binary fluid. The pink highlighted area denotes the region where Landau theory is not applicable according to the conventional Ginzburg-criterion. In the blue area we observe classical nucleation, whereas in the green area we observe the gradual transition from nucleation to spinodal decomposition. This plot is taken from ref.[6]

motivation for this generalized Ginzburg criterion comes from the observation that Cahn-Hilliard theory is definitely applicable as long as the nucleation barrier is large compared to  $k_B T$ , but breaks down when the free energy barrier is of the same magnitude as  $k_B T$ . This more general Ginzburg criterion for the model defined in equation ( 2.52) is then given by

$$\lambda^D \left(1 - \frac{T}{T_c}\right)^{D-D/2} \left| \frac{\phi}{\phi_{sp}} - 1 \right|^{3-D/2} \gg 1, \quad (2.54)$$

where  $\phi_{sp}$  denotes the order parameter at the spinodal.

## Chapter 3

# The Lattice Boltzmann Method

Given a simple fluid, we want to find a model that mimics the physical behaviour of this system as well as possible. Depending on what we are interested in, we have a few possibilities.

In the macroscopic picture our fluid is treated as continuum and quantities such as velocity and density become smooth vector-fields. The associated problem for this setting consists in solving partial differential equations for those vector fields, such as the Navier-Stokes and the continuity equation. In this ansatz we gain macroscopic information about the flow of our fluid, the density and the pressure, but the microscopic information is thrown away.

In molecular dynamics, on the other hand, the liquid is modelled as many particle system with a suitable model interaction potential. The Newtonian equations of motion are then solved in small time steps for every particle. Molecular dynamics is an adequate method if we are interested in the microscopic dynamics of our fluid.

The lattice Boltzmann method finally serves as a method that throws some of the microscopic information away, but not all of it. As special discretization of the discrete Boltzmann equation [64], the basic idea of lattice Boltzmann is to use discrete distribution functions and solve the Boltzmann equation in every time step.

Therefore we will begin with a review of some Boltzmann equation basics and then move on to explain the lattice Boltzmann method.

## 3.1 The Boltzmann Equation

In this section we derive the Boltzmann equation and discuss several topics related to this equation. The derivation closely follows [25]. The main literature sources for this section are [25, 31, 15, 53].

### 3.1.1 Derivation of the Boltzmann equation

Consider a fluid in a certain initial state and with a conserved total number of particles  $N$ . We are interested in the time evolution of this system. Instead of calculating the time evolution for individual particles, a particle distribution function  $f(\vec{x}, \vec{v}, t)$  is introduced. The underlying vector-space is the six-dimensional phase space denoted as  $\mu$ -phase space. In this framework  $f(\vec{x}, \vec{v}, t)d^3\vec{x}d^3\vec{v}$  denotes the number of particles in the six-dimensional cube  $[\vec{x} - \Delta\vec{x}, \vec{x} + \Delta\vec{x}] \times [\vec{v} - \Delta\vec{v}, \vec{v} + \Delta\vec{v}]$  around  $(\vec{x}, \vec{v})$  at the time  $t$ .

If no collisions are present in the system, the number of particles  $N(t)$  in the six-dimensional cube around the particles is conserved and therefore

$$\begin{aligned}\Delta N(t) &= N(t + \Delta t) - N(t) \\ &= f(\vec{x} + \vec{v}\Delta t, \vec{v} + \frac{\vec{F}\Delta t}{m}, t + \Delta t)d^3\vec{x}'d^3\vec{v}' - f(\vec{x}, \vec{v}, t)d^3\vec{x}d^3\vec{v} \\ &= 0,\end{aligned}\tag{3.1}$$

where  $\vec{F}$  is an external, momentum independent, conservative force. The expression  $f(\vec{x} + \vec{v}\Delta t, \vec{v} + \frac{\vec{F}\Delta t}{m}, t + \Delta t)d^3\vec{x}'d^3\vec{v}'$  denotes the number of particles at the time  $t + \Delta t$  in the volume element  $d^3x'd^3v'$ . Since  $\vec{x}$  and  $\vec{v}$  are time dependent, the volume element  $d^3xd^3v$  also changes to  $d^3x'd^3v'$ . The two volume elements are related via the Jacobian  $\|J\|$  [31]:

$$d^3x'(t)d^3v'(t) = d^3x(t + \Delta t)d^3v(t + \Delta t) = \|J\|d^3x(t)d^3v(t).\tag{3.2}$$

The Jacobian is approximately given by [31]

$$\|J\| = 1 + \frac{\partial F_i}{\partial v_i} + \mathcal{O}[(\Delta t)^2].\tag{3.3}$$

As a second step, we allow collisions.

We Taylor-expand  $f(\vec{x} + \vec{v}\Delta t, \vec{v} + \frac{\vec{F}\Delta t}{m}, t + \Delta t)$  around  $f(\vec{x}, \vec{v}, t)$ :

$$\begin{aligned}f(\vec{x} + \vec{v}\Delta t, \vec{v} + \frac{\vec{F}\Delta t}{m}, t + \Delta t) &= f(\vec{x}, \vec{v}, t) + \frac{\partial f}{\partial t}\Delta t + \frac{\partial f}{\partial x_i}v_i\Delta t + \frac{\partial f}{\partial v_i}\frac{F_i\Delta t}{m} \\ &\quad + \mathcal{O}[(\Delta t)^2].\end{aligned}\tag{3.4}$$

---

We are interested in changes of the number of particles during a time  $\Delta t$ , i.e. in the difference quotient  $\frac{\Delta N}{\Delta t}$ .

Combining equations 3.1, 3.3 and 3.4 and neglecting terms of order  $(\Delta t)^2$  we get

$$\begin{aligned}\frac{\Delta N}{\Delta t} &= \frac{1}{\Delta t} \left[ f(\vec{x}, \vec{v}, t) + \frac{\partial f}{\partial t} \Delta t + \frac{\partial f}{\partial x_i} v_i \Delta t + \frac{\partial f}{\partial v_i} F_i \Delta t \right] d^3 x' d^3 v' \\ &- \frac{1}{\Delta t} f(\vec{x}, \vec{v}, t) d^3 x d^3 v \\ &= \left[ \frac{\partial f}{\partial t} + v_i \frac{\partial f}{\partial x_i} + \frac{\partial f F_i}{\partial v_i} \right] d^3 x d^3 v.\end{aligned}\tag{3.5}$$

Due to collisions  $\frac{\Delta N}{\Delta t}$  is not zero any more. Some particles are pushed into the small volume around  $(\vec{x}, \vec{v})$  while others are pushed out of this volume. This yields the following balance equation,

$$\left[ \frac{\partial f}{\partial t} + v_i \frac{\partial f}{\partial x_i} + \frac{\partial f F_i}{\partial v_i} \right] d^3 x d^3 v = \left[ \left( \frac{\partial f}{\partial t} \right)_- + \left( \frac{\partial f}{\partial t} \right)_+ \right] d^3 x d^3 v,\tag{3.6}$$

where  $\left( \frac{\partial f}{\partial t} \right)_- d^3 \vec{x} d^3 \vec{v}$  is the number of particles pushed out of the volume element and  $\left( \frac{\partial f}{\partial t} \right)_+ d^3 \vec{x} d^3 \vec{v}$  is the number of particles pushed into it. Therefore the Boltzmann equation has the following form:

$$\frac{\partial f}{\partial t} + v_i \frac{\partial f}{\partial x_i} + \frac{\partial f F_i / m}{\partial v_i} = \left( \frac{\partial f}{\partial t} \right)_- + \left( \frac{\partial f}{\partial t} \right)_+.\tag{3.7}$$

In order to resolve the detailed mathematical structure of those collision terms we need to make further assumptions. First of all, we only consider dilute gases consisting of hard sphere particles.

As the mean free path  $\lambda_l$  is given by

$$\lambda_l = \frac{1}{\sqrt{2} \sigma \rho},\tag{3.8}$$

with the scattering cross section  $\sigma$  and the density  $\rho$ , we observe that  $\lambda_l$  of a dilute gas is much bigger than the diameter of the gas particles  $q$  ( $l \gg q$ ). Therefore we can apply the concept of molecular chaos, i.e. the joint probability  $g(\vec{x}_1, \vec{p}_1, \vec{x}_2, \vec{p}_2)$  to find particle 1 at  $(\vec{x}_1, \vec{p}_1)$  while particle 2 is at  $(\vec{x}_2, \vec{p}_2)$ , can be written as a product.

$$g(\vec{x}_1, \vec{p}_1, \vec{x}_2, \vec{p}_2) = \frac{g_1(\vec{x}_1, \vec{p}_1)}{N} \times \frac{g_2(\vec{x}_2, \vec{p}_2)}{N}.\tag{3.9}$$

This factorization corresponds to the approximation that position and velocities of two arbitrary particles are statistically independent. Another approximation that follows from the dilute-gas-with-hard-sphere-particle regime is taking into account elastic two-particle-collisions only: The mean time  $\tau$  between two collisions is given by

$$\tau = \frac{1}{\bar{v}_{12}\sigma\rho}, \quad (3.10)$$

and the duration of the whole collision process  $t_d$  is estimated to be

$$t_d = \frac{q}{\bar{v}}, \quad (3.11)$$

$\bar{v}$  being the mean velocity. Therefore, the probability for a particle to collide with another  $P_{coll}$  is proportional to

$$P_{coll} \propto \frac{q}{\bar{v}\tau} = \frac{d}{\lambda_l}. \quad (3.12)$$

As we have a dilute gas, this probability is small and therefore it's a valid approximation to consider elastic two-particle-collisions only. In elastic collisions, energy and momentum are conserved. Assuming that all the particles have the same mass, we get

$$\vec{v} + \vec{v}_1 = \vec{v}' + \vec{v}_1', \quad \|\vec{v}\|^2 + \|\vec{v}_1\|^2 = \|\vec{v}'\|^2 + \|\vec{v}_1'\|^2. \quad (3.13)$$

We transform  $\vec{v}$ ,  $\vec{v}_1$ ,  $\vec{v}'$  and  $\vec{v}_1'$  to center of mass frame coordinates:

$$\vec{v} = \frac{\vec{v}_s + \vec{v}_r}{2}, \quad (3.14)$$

$$\vec{v}_1 = \frac{\vec{v}_s - \vec{v}_r}{2}, \quad (3.15)$$

$$\vec{v}' = \frac{\vec{v}_s + \vec{v}_r'}{2}, \quad (3.16)$$

$$\vec{v}_1' = \frac{\vec{v}_s - \vec{v}_r'}{2}, \quad (3.17)$$

where  $\vec{v}_r = \vec{v} - \vec{v}_1$  is the relative velocity and  $\vec{v}_s = \frac{\vec{v} + \vec{v}_1}{2}$  is the center of mass velocity. During the collision only the relative velocity changes from  $\vec{p}_r$  to  $\vec{p}_r'$ , hence the energy conservation is given by

$$\|\vec{v}_r\|^2 = \|\vec{v}_r'\|^2. \quad (3.18)$$

---

Now we do have enough information to evaluate  $\left(\frac{\partial f}{\partial t}\right)_- d^3x d^3v$  and  $\left(\frac{\partial f}{\partial t}\right)_+ d^3x d^3v$ . In our present setting the number of particles pushed out of the small volume element,  $\left(\frac{\partial f}{\partial t}\right)_- d^3x d^3v$  depends on the particles that inhabited  $d^3x d^3v$  before the collision, the sum over all particles that collide with those in  $d^3x d^3v$  per time and the total cross section in the center of mass frame.

We get:

$$\left(\frac{\partial f}{\partial t}\right)_- d^3x d^3v = d^3x d^3v f(\vec{x}, \vec{v}, t) \int d^3v_1 \|\vec{v} - \vec{v}_1\| f(\vec{x}, \vec{v}_1, t) \int d\Omega \frac{d\sigma}{d\Omega} (\|\vec{p} - \vec{p}_1\|, \theta). \quad (3.19)$$

Now we calculate the number of particles pushed into  $d^3x d^3v$ . From the transformation to the center of momentum frame follows that

$$d^3v d^3v_1 = \frac{d^3v_s d^3v_r}{8}, \quad (3.20)$$

and

$$d^3v' d^3v'_1 = \frac{d^3v_s d^3v'_r}{8}. \quad (3.21)$$

From energy conservation, we get

$$\|\vec{p}_r\| = \|\vec{p}'_r\|. \quad (3.22)$$

Therefore we can conclude that  $d^3v d^3v_1 = d^3v' d^3v'_1$ . Now we just have to exchange  $v$  and  $v'$ . In addition, we assume that the scattering-cross section for  $\vec{v}_r \rightarrow \vec{v}'_r$  and  $\vec{v}_r \rightarrow \vec{v}'_r$  remains the same (time reversal invariance),

$$\left(\frac{\partial f}{\partial t}\right)_+ d^3x d^3v' = d^3x d^3v' f(\vec{x}, \vec{v}', t) \int d^3v_1 \|\vec{v} - \vec{v}_1\| f(\vec{x}, \vec{v}_1, t) \int d\Omega \frac{d\sigma}{d\Omega} (\|\vec{p} - \vec{p}_1\|, \theta). \quad (3.23)$$

We use the following abbreviations

$$f = f(\vec{x}, \vec{v}, t), \quad f_1 = f(\vec{x}, \vec{v}_1, t), \quad f' = f(\vec{x}, \vec{v}', t), \quad f'_1 = f(\vec{x}, \vec{v}'_1, t), \quad (3.24)$$

and finally get the Boltzmann equation

$$\frac{\partial f}{\partial t} + v_i \frac{\partial f}{\partial x_i} + \frac{\partial f F_i}{\partial v_i} = \int d^3v_1 \|\vec{v} - \vec{v}_1\| \int d\Omega \frac{d\sigma}{d\Omega} (\|\vec{p} - \vec{p}_1\|, \theta) (f' f'_1 - f f_1). \quad (3.25)$$

Note that the collision integral is often abbreviated as  $Q(f, f_1)$ .

### 3.1.2 Moments of the Distribution Function

In order to relate the distribution function  $f(\vec{x}, \vec{v}, t)$  to macroscopic fields, one takes the integral over all velocities of the distribution function times the relevant quantity [31]:

mass density

$$\rho(\vec{x}, t) = \int m f(\vec{x}, \vec{v}, t) d^3v, \quad (3.26)$$

momentum density

$$\rho u_i(\vec{x}, t) = \int m v_i f(\vec{x}, \vec{v}, t) d^3v, \quad (3.27)$$

energy density

$$\rho e(\vec{x}, t) = \frac{1}{2} \int m v_i^2 f(\vec{x}, \vec{v}, t) d^3v. \quad (3.28)$$

### 3.1.3 Maxwellian Equilibrium Distribution

We seek an equilibrium distribution of the Boltzmann Equation. In equilibrium as many particles get pushed out of the small control volume as are pushed into it. Therefore the collision term must vanish for equilibrium distributions [31, 15],

$$Q(f^{eq}, f_1^{eq}) = \int d^3v_1 \|\vec{v} - \vec{v}_1\| \int d\Omega \frac{d\sigma}{d\Omega} (\|\vec{p} - \vec{p}_1\|, \theta) (f' f'_1 - f f_1) = 0. \quad (3.29)$$

We can conclude that

$$f f_1 = f' f'_1. \quad (3.30)$$

Taking the logarithm, we observe that  $\log(f)$  is an additive collisional invariant:

$$\log(f) + \log(f_1) = \log(f') + \log(f'_1). \quad (3.31)$$

In general, a collisional invariant  $\gamma$  is defined [31] as a quantity that fulfils

$$\gamma + \gamma_1 = \gamma' + \gamma'_1. \quad (3.32)$$

In kinetic theory exists a theorem [31, 53] that states that a continuous function  $\gamma(a)$   $a \in \mathbb{R}^3$  is an additive collisional invariant if and only if it can be written as

$$\gamma(a) = A + B_i a_i + C a_i^2, \quad (3.33)$$



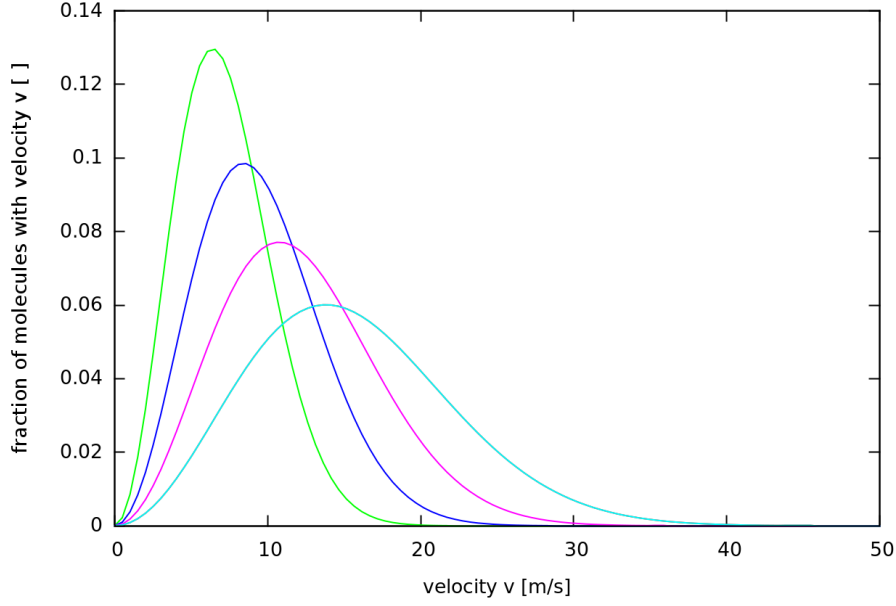


Figure 3.1: Velocity distribution of a Maxwell-Boltzmann distributed Nitrogen-gas at different temperatures: green line  $T = 0$ , blue line  $T = 200$ , pink line  $T = 500$ , turquoise  $T = 1000$ , temperatures  $T$  in degree Celsius

where  $A, C : \mathbb{R}^n \rightarrow \mathbb{R}$ ,  $B : \mathbb{R}^n \rightarrow \mathbb{R}^3$  and  $A, B, C$  are independent of  $a$ . Therefore  $\log(f)$  has the following form:

$$\log(f) = A + B_i v_i + \frac{1}{2} C v_i^2. \quad (3.34)$$

The final form of the Maxwellian is derived by inserting the above expression for  $f$  into the moments of the distribution function and calculating the integrals [31]. Having done so, we finally arrive at

$$f^{eq}(\vec{v}) = \left(\frac{\beta}{\pi}\right)^{\frac{D}{2}} \rho e^{-\beta(\vec{v}-\vec{u})^2}, \quad (3.35)$$

where  $\beta = \frac{m}{2k_B T}$ .

### 3.1.4 The H-Theorem

Back in 1872 Boltzmann derived the H-theorem from the Boltzmann equation.

**H-Theorem:** The functional  $H[f]$  given by [31, 15, 53]

$$H[f] = \int_V d^3x \int d^3v f \ln f, \quad (3.36)$$

fulfils

$$\frac{d}{dt}H[f] \leq 0, \quad (3.37)$$

and

$$\frac{d}{dt}H[f] = 0, \quad (3.38)$$

if and only if  $f = f^{eq}$ .

Here,  $f(\vec{x}, \vec{v}, t)$  is a distribution function that fulfils the Boltzmann Equation and  $f^{eq}$  is the Maxwell distribution.

The entropy of a system described by the distribution function  $f(\vec{x}, \vec{v}, t)$ , the so called Boltzmann entropy, is defined by

$$S = -k_B H[f] = -k_b \int_V d^3x \int d^3v f \ln f, \quad (3.39)$$

where  $k_B$  is the Boltzmann constant. For the equilibrium situation this relation can even be derived from basic thermodynamics [15].

In this view, the H-Theorem can be interpreted as a proof for the second principle of thermodynamics.

### Criticism

Since Boltzmann just assumed that the distribution functions are smooth, without having a proof for that, his proof of the H-theorem is not considered as rigorous today. Unfortunately, even nowadays there exists no known rigorous proof for the theorem [58].

Apart from that, there have been many discussions going on over the last century about the theorem's ability to predict the behaviour of real physical systems. For a detailed discussion see [15, 58, 28, 31].

The main objection in many of those discussions is that the H-theorem states irreversibility although Boltzmann equation and H-theorem were derived from reversible Newtonian mechanics. It turns out that the assumption of molecular chaos plays a key role in this emerging irreversibility [15]. In the last decades, the H-theorem was tested via molecular simulation and it was for example found that in hard disks systems the H-functional increased when all velocities were reversed at once but apart from that somewhat artificial situation, the H-theorem could be confirmed for this hard disk system. See [40] for the original paper.

### 3.1.5 Relaxation Time Approximation

The collision term proposed in the derivation of the Boltzmann equation is a complicated integral term. Therefore, quite a lot of approximations to

---

$Q$  were proposed. One of them is the relaxation time approximation, also known as BGK-model, where the collision term is approximated by

$$Q_{RT}(f, f^{eq}) = \frac{1}{-\tau} [f(\vec{x}, \vec{v}, t) - f^{eq}(\vec{x}, \vec{v}, t)]. \quad (3.40)$$

Here,  $f^{eq}$  is a Maxwellian that depends on  $f(\vec{x}, \vec{v}, t)$  and therefore also varies with time, space and velocity now. In literature  $f^{eq}$  is known as local equilibrium function or local Maxwellian [53]. The relaxation time  $\tau$  is a frequency of the order of the collision frequency. In most cases  $\tau$  is a constant, although sometimes it is made a function of time and space. [31, 15]

$Q_{RT}$  and every alternative collision term has to fulfil the same properties as the original  $Q$  [31, 15]:

1. For all summational invariants  $\xi = m, mv_i, \frac{mv^2}{2}$  and for all linear combinations of those, the following integral must vanish:

$$\int \xi Q_{apx} d^3v = 0. \quad (3.41)$$

2. The H-theorem has to be fulfilled:

$$\int \log(f) Q_{apx} d^3v \leq 0. \quad (3.42)$$

Though looking quite primitive, the BGK model is in fact more non-linear than the true collision term [15, 53]. While  $Q(f, f)$  is only quadratic in  $f$ ,  $f$  appears in the exponential of  $Q_{RT}(f, f^{eq})$ , since  $\rho, \vec{u}$  and  $T$  in the Maxwellian  $f^{eq}$  are functions of  $f$ . The advantage of  $Q_{RT}$  is that one directly obtains integral expressions for the macroscopic quantities  $\rho, v$  and  $T$ , and thereby the numerical solution procedure is simplified.

## 3.2 The Lattice Boltzmann Equation

As a special discretization of the discrete Boltzmann equation [64], the lattice Boltzmann equation has the following form:

$$f_i(\vec{x} + \vec{c}_i \Delta t, t + \Delta t) - f_i(\vec{x}, t) = Q, \quad 0 \leq i \leq p. \quad (3.43)$$

Here,  $f_i$  is the particle distribution function of the  $i^{th}$  velocity at the lattice point  $\vec{x}$  at the time  $t$  and  $Q$  denotes the collision term.

The lattice Boltzmann equation is discrete in time, space and velocity. To

every lattice point in discrete space  $p$  velocity directions are assigned (see figure 3.2). The value of the particle distribution function  $f_i(\vec{x}_j, t)$  at  $\vec{x}_j$  is the number of particles in a small three-dimensional cube around  $\vec{x}_j$  that have the velocity  $\vec{c}_i$  divided by the total number of particles in this small volume.

In each time step, we update the distribution function, i.e. we solve the lattice Boltzmann equation. Most of the current lattice Boltzmann models use the BGK approximation for the collision term:

$$f_i(\vec{x} + \vec{c}_i \delta t, t + \delta t) - f_i(\vec{x}, t) = -\frac{1}{\tau}(f_i(\vec{x}, t) - f_i^{eq}(\vec{x}, t)), \quad (3.44)$$

where  $\tau$  is a (often constant) relaxation time.

Note, that although we have introduced the three-dimensional lattice Boltzmann equation here, the basic formalism for the  $n$ -dimensional LB-equation is the same as for the three dimensional world. In the following subsections we will take a closer look at the concepts introduced above. The main literature sources for this section and section 3.3 are [64, 53, 47, 19, 20].

### 3.2.1 The Lattice

In lattice Boltzmann Simulations various lattice types are used. They are abbreviated as DnQp, where  $n$  denotes the dimension of the lattice and  $p$  is the number of different velocity directions. For example, D2Q9 is a two dimensional model with nine different velocity directions (see figure 3.2), where zero is also a velocity that stands for the rest particles.

### Lattice Tensors and the Isotropy of Lattice Models

As we will see later, every lattice Boltzmann model is verified by taking the macroscopic limit which should yield the Navier-Stokes equations. Since the Navier-Stokes equations are isotropic, i.e invariant under orthogonal transformations (rotations and reflections), the used lattice type should also have a "kind of" isotropy.

A discrete lattice can of course not be invariant under arbitrary orthogonal transformations but mathematicians have developed concepts that enable us to tell whether a lattice has sufficient isotropy. To be more precise, according to ref. [64] they introduced so called lattice tensors. For lattice Boltzmann models the lattice tensors are constructed in the following way [64]:

$$T_{n_1, n_2, \dots, n_m} = \sum_i c_{in_1} c_{in_2} \dots c_{in_m}, \quad (3.45)$$

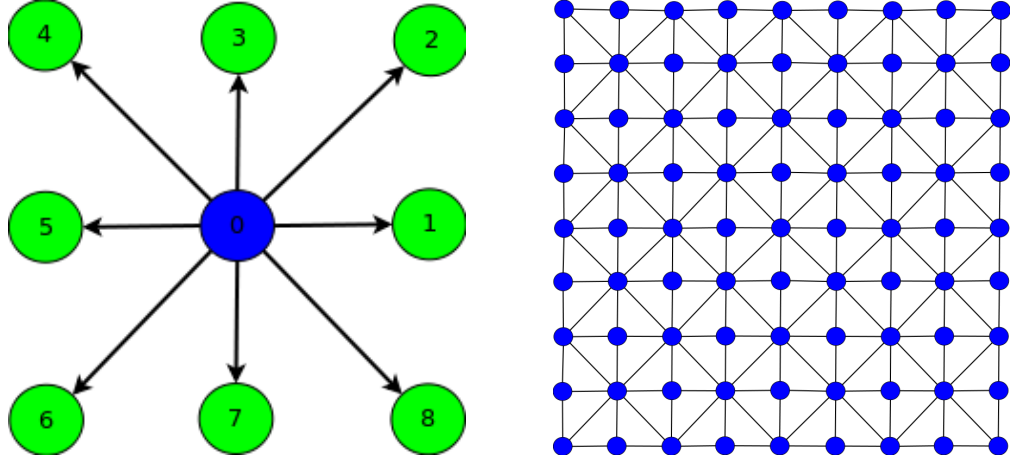


Figure 3.2: right-hand side: a D2Q9 lattice of a square-like simulation domain, left-hand side: a single lattice point with all its neighbours, the numbers denote the associated lattice velocity  $c_i$ ,  $0 \leq i \leq 8$

where the  $c_{inl}$  are the usual lattice velocities. Now we can construct lattice tensors for every DnQp model and check whether they are isotropic. Note that it is sufficient to check the corresponding lattice tensors up to the rank of the highest rank tensor occurring in the macroscopic equations.

### 3.2.2 Moments of the Distribution Function

The moments of the particle distribution function are defined such that the macroscopic equations can be derived in the thermodynamic limit. This leads to the following definitions:

$$\rho(\vec{x}, t) = \sum_i f_i, \quad (3.46)$$

for the density which is denoted as the zeroth moment, and

$$\vec{j}(\vec{x}, t) = \rho(\vec{x}, t) \vec{u}(\vec{x}, t) = \sum_i \vec{c}_i f_i, \quad (3.47)$$

for the momentum flux which is denoted as the first moment. This equation also defines  $\vec{u}$ , the average velocity.

The zeroth and the first moment are conserved quantities and have the same form for every lattice Boltzmann model. Higher Moments ( $\geq 2$ ) are chosen in order to model the physical behaviour of the system under interest.

### 3.2.3 The Structure of the Lattice Boltzmann Equation: Collisions and Streaming

The core of every lattice Boltzmann algorithm is the solution of the lattice Boltzmann equation in each time step. The solution process can be divided into three parts which are executed at every time step. First, we need to calculate the local equilibrium distributions  $f_i^{eq}(\vec{x}, t)$ . In the next step, the so called collision step, we solve the lattice Boltzmann BGK equation:

$$f_i^*(\vec{x}, t) = f_i(\vec{x}, t) - \frac{1}{\tau} (f_i(\vec{x}, t) - f_i^{eq}(\vec{x}, t)), \quad (3.48)$$

where the  $f_i^*$  are the distribution functions after the collision. In the last step, the streaming step, the newly calculated distribution functions are streamed to the neighbouring lattice sites according to the streaming rule:

$$f_i^*(\vec{x}, t) = f_i(\vec{x} + \vec{c}_i \Delta t, t + \Delta t). \quad (3.49)$$

In the lattice gas cellular automata theory, the collision rule represented particle collisions [64, 53, 47]. In lattice Boltzmann Theory not individual particles, but particle distributions are streamed to their next neighbours. As indicated above, the possible streaming directions are the discrete velocity directions. In addition, in most cases, the distribution functions are only streamed to their nearest neighbour, i.e., there is only next-neighbour coupling.

For illustration we take a look at the streaming in a D2Q9 lattice, which is numbered according to picture 3.2:

$$\begin{aligned} f_0^{new} &= f_0^{old}, & f_5^{new} &= f_1^{old}, \\ f_1^{new} &= f_5^{old}, & f_6^{new} &= f_2^{old}, \\ f_2^{new} &= f_6^{old}, & f_7^{new} &= f_3^{old}, \\ f_3^{new} &= f_7^{old}, & f_8^{new} &= f_4^{old}, \\ f_4^{new} &= f_8^{old}. \end{aligned} \quad (3.50)$$

### 3.2.4 Chapman Enskog Expansion: From Lattice Boltzmann to Navier-Stokes

In the last chapter, we learned that the Navier-Stokes equation and the continuity equation can be derived from the Boltzmann equation via the so

called Chapman Enskog method. Now, we sketch a derivation of the Navier-Stokes equation and the continuity equation from the lattice Boltzmann BGK model. The derivation closely follows the one in ref. [64]. The expansion parameter  $\epsilon$  corresponds to the Knudsen number  $Kn = \frac{\lambda}{l}$ , where  $\lambda$  is the mean free path and  $l$  the characteristic length scale of the flow. If the mean free path is fixed and the characteristic length scale grows, the Knudsen number tends to zero. Therefore the Knudsen number is a measure for the degree of coarse graining [64, 20].

We begin with writing down the distribution function as a deviation from the equilibrium distribution  $f_i^{eq}$ :

$$f_i(\vec{x}, t) = f_i^{eq}(\vec{x}, t) + \epsilon f_i^1(\vec{x}, t) + \epsilon^2 f_i^2 + \mathcal{O}(\epsilon^3). \quad (3.51)$$

Since the  $0^{th}$  and  $1^{st}$  moments are conserved quantities, they must vanish for  $f_i^n$  with  $n \geq 1$ :

$$\sum_i f_i^1(\vec{x}, t) = 0, \quad \sum_i \vec{c}_i f_i^1 = 0, \quad (3.52)$$

$$\sum_i f_i^2(\vec{x}, t) = 0, \quad \sum_i \vec{c}_i f_i^2 = 0. \quad (3.53)$$

In the next step we write  $f(\vec{x} + \vec{c}_i \Delta t, t + \Delta t)$  as Taylor series around  $(\vec{x}, t)$  up to second order:

$$\begin{aligned} f_i(\vec{x} + \vec{c}_i \Delta t, t + \Delta t) &= f_i(\vec{x}, t) + \Delta t \partial_t f_i + \Delta t c_{i\alpha} \partial_{x_\alpha} f_i \\ &+ \frac{(\Delta t)^2}{2} [\partial_t \partial_t f_i + 2c_{i\alpha} \partial_t \partial_{x_\alpha} f_i + c_{i\alpha} c_{i\beta} \partial_{x_\alpha} \partial_{x_\beta} f_i] \\ &+ \mathcal{O}(\partial^3 f_i). \end{aligned} \quad (3.54)$$

We insert equation (2.44) into the lattice Boltzmann BGK equation and arrive at

$$\begin{aligned} 0 &= f_i + \Delta t \partial_t f_i + \Delta t c_{i\alpha} \partial_{x_\alpha} f_i \\ &+ \frac{(\Delta t)^2}{2} [\partial_t \partial_t f_i + 2c_{i\alpha} \partial_t \partial_{x_\alpha} f_i + c_{i\alpha} c_{i\beta} \partial_{x_\alpha} \partial_{x_\beta} f_i] \\ &- f_i + \frac{1}{\tau} (f_i - f_i^{eq}). \end{aligned} \quad (3.55)$$

Now we replace  $f$  by the expansion around the equilibrium  $f_i^{eq}$ :

$$\begin{aligned} 0 &= \Delta t \partial_t (f_i^{eq} + \epsilon f_i^1 + \epsilon^2 f_i^2) + \Delta t c_{i\alpha} \partial_{x_\alpha} (f_i^{eq} + \epsilon f_i^1 + \epsilon^2 f_i^2) \\ &+ \frac{(\Delta t)^2}{2} [\partial_t \partial_t (f_i^{eq} + \epsilon f_i^1 + \epsilon^2 f_i^2) + 2c_{i\alpha} \partial_t \partial_{x_\alpha} (f_i^{eq} + \epsilon f_i^1 + \epsilon^2 f_i^2)] + \\ &+ \frac{(\Delta t)^2}{2} [c_{i\alpha} c_{i\beta} \partial_{x_\alpha} \partial_{x_\beta} (f_i^{eq} + \epsilon f_i^1 + \epsilon^2 f_i^2)]. \end{aligned} \quad (3.56)$$

Since we are interested in macroscopic scales we transform the differential operators  $\partial_t$  and  $\partial_{x_\alpha}$  to larger time and space scales. We consider one space and two time scales, where the  $\epsilon$ -term refers to a small hydrodynamic and the  $\epsilon^2$ -term to a large hydrodynamic time scale [19]:

$$\partial_t \rightarrow \epsilon \partial_t^1 + \epsilon^2 \partial_t^2, \quad (3.57)$$

$$\partial_{x_\alpha} \rightarrow \epsilon \partial_{x_\alpha}^1. \quad (3.58)$$

We now apply these new differential operators. Neglecting all terms higher than second order yields

$$\begin{aligned} 0 &= \epsilon \Delta t (\partial_t^1 f_i^{eq} + c_{i\alpha} \partial_{x_\alpha}^1 f_i^{eq}) \\ &+ \epsilon^2 \Delta t (\partial_t^1 f_i^1 + \partial_t^2 f_i^{eq} + c_{i\alpha} \partial_{x_\alpha}^1 f_i^1) \\ &+ \epsilon^2 \frac{(\Delta t)^2}{2} \left( \partial_t^1 \partial_t^1 f_i^{eq} + 2c_{i\alpha} \partial_t^1 \partial_{x_\alpha}^1 f_i^{eq} + c_{i\alpha} c_{i\beta} \partial_{x_\alpha}^1 \partial_{x_\beta}^1 f_i^{eq} \right) \\ &+ \frac{1}{\tau} \epsilon f_i^1 + \frac{1}{\tau} \epsilon^2 f_i^2. \end{aligned} \quad (3.59)$$

By grouping the different  $\epsilon$  orders, we get the following structure:

$$0 = \epsilon T_i^0 + \epsilon^2 T_i^1 + \mathcal{O}(\epsilon^3), \quad (3.60)$$

with

$$T_i^0 = \partial_t^1 f_i^{eq} + c_{i\alpha} \partial_{x_\alpha}^1 f_i^{eq} + \frac{1}{\tau \Delta t} f_i^1, \quad (3.61)$$

$$\begin{aligned} T_i^1 &= \partial_t^1 f_i^1 + \partial_t^2 f_i^{eq} + c_{i\alpha} \partial_{x_\alpha}^1 f_i^1 \\ &+ \frac{\Delta t}{2} \left( \partial_t^1 \partial_t^1 f_i^{eq} + 2c_{i\alpha} \partial_t^1 \partial_{x_\alpha}^1 f_i^{eq} + c_{i\alpha} c_{i\beta} \partial_{x_\alpha}^1 \partial_{x_\beta}^1 f_i^{eq} \right) \\ &+ \frac{1}{\tau \Delta t} f_i^2. \end{aligned} \quad (3.62)$$

From

$$\sum_i T_i^0 = 0, \quad \sum_i c_{i\alpha} T_i^0 = 0, \quad (3.63)$$

$$\sum_i T_i^1 = 0, \quad \sum_i c_{i\alpha} T_i^1 = 0, \quad (3.64)$$

and by inserting the  $T_i$  into the expression for the  $0^{th}$  moment we get

$$\begin{aligned} \sum_i T_i^0 &= \sum_i \partial_t^1 f_i^0 + c_{i\alpha} \partial_{x_\alpha}^1 f_i^1 + \frac{1}{\tau \Delta t} f_i^1 \\ &= \partial_t^1 \rho + \partial_{x_\alpha}^1 j_\alpha \end{aligned} \quad (3.65)$$



---

and corresponding to the continuity equation

$$\partial_t \rho + \nabla j = 0. \quad (3.66)$$

A similar calculation of the momentum term yields the incompressible Navier Stokes equation (for the whole derivation see [64])

$$\partial_t \vec{u}(\vec{x}) + \left( \vec{u}(\vec{x}) \nabla \right) \vec{u}(\vec{x}) = \frac{1}{-\rho} \vec{\nabla} p(\vec{x}), \quad (3.67)$$

where  $\vec{u}$  is the fluid velocity,  $\rho$  the constant fluid density and  $p(\vec{x})$  the pressure. A calculation that would involve first order as well as second order terms in  $\epsilon$  and where the form of the equilibrium distribution is important, would yield the full Navier-Stokes equation (see again [64]).

### 3.3 Modelling Lattice Boltzmann

In this section we will give a brief sketch of how a lattice Boltzmann model can be created. We start with the choice of kinetic equation, then turn to the calculation of the local equilibrium distribution and finally arrive at the discussion of the available boundary conditions and the question of how to implement a lattice Boltzmann model.

#### 3.3.1 The Kinetic Equation and the Lattice

At the beginning one chooses the form of the kinetic equation and the geometry of the lattice. In most applications the BGK-Approximation is used, also known as Single-Relaxation-Time-Approximation (SRT). A more stable alternative is the Multi-Relaxation-Time-Approximation (MRT) [18, 20, 19], which is described in section 3.4.

The decision which lattice to take is more sensitive: On the one hand one strives to keep the computational cost small which corresponds to choosing a lattice with few velocity directions, but, on the other hand, the physical problem should be treated as correctly as possible. Beside rotational isotropy [64], other, problem-dependent factors might influence the choice of the lattice type, see ref. [53] for examples.

#### 3.3.2 Derivation of the Equilibrium Distribution

All lattice Boltzmann models we deal with in this thesis, have a local equilibrium function. As the kinetic equation and the lattice are not very model-

specific, the problem inherent physics comes in through the equilibrium distribution function. As the equilibrium distribution is highly problem dependent, the derivation of the desired function is usually not straightforward. Nevertheless, there are at least two known methods of how to proceed: the maximum entropy method [20] and the ansatz method [64]. Here, we present the maximum entropy method.

**The Maximum Entropy Method** In the maximum entropy method we derive the equilibrium distributions by exploiting the concepts of statistical mechanics. We closely follow the derivation of ref. [19].

We recall that the distribution function  $f_i(\vec{x}, t)$  tells us what fraction of the density  $\rho$  at the lattice site  $\vec{x}$  has the velocity  $\vec{c}_i$  at time  $t$ . The actual number of particles that sit at the lattice point  $\vec{x}$  and has the velocity  $\vec{c}_i$  is then given by

$$z_i = \frac{f_i}{\mu_m}, \quad (3.68)$$

where  $\mu_m = \frac{m_p}{l^d}$  is the mass density parameter with  $m_p$  as the particle mass,  $l$  as the lattice spacing and  $d$  as the dimension.

At first we ask what is the probability that  $z_i^1$  particles sit at an arbitrary  $(\vec{x}^1, \vec{c}_i^1)$ , when the number of particles is independent of the number of particles at all other points  $(\vec{x}, \vec{c}_i)$ . The probability distribution is a Poisson distribution:

$$P(z_i) = \frac{\bar{z}_i^{z_i}}{z_i!} \exp(-\bar{z}_i), \quad (3.69)$$

where  $\bar{z}_i$  is the mean value of  $z_i$ .

In the next step, we want to find the probability density  $P(\{z_i\})$  in the configuration space  $\{z_i\}$  of velocities at a lattice point  $\vec{x}$ . In addition, we only allow those configurations with a special value for the density  $\rho(\vec{x}, t)$  and the momentum density  $\rho\vec{u}$ . We get

$$P(\{z_i\}) \propto \left( \prod_i \frac{\bar{z}_i^{z_i}}{z_i!} \exp(-\bar{z}_i) \right) \delta \left( \mu_m \sum_i z_i - \rho \right) \delta \left( \mu_m \sum_i z_i \vec{c}_i - \rho \vec{u} \right). \quad (3.70)$$

Assuming that  $z_i \gg 1$  and applying the Stirling approximation, we get for the entropy of the lattice configuration  $\{z_i\}$

$$S(\{z_i\}) = -z_i \log(z_i) - z_i - z_i \log(\bar{z}_i) + \bar{z}_i. \quad (3.71)$$

Now we can write  $P(\{z_i\})$  in terms of the entropy:

$$P(\{z_i\}) \propto \exp[S(\{z_i\})] \delta \left( \mu_m \sum_i z_i - \rho \right) \delta \left( \mu_m \sum_i z_i \vec{c}_i - \rho \vec{u} \right). \quad (3.72)$$

---

In order to calculate the equilibrium distribution we maximize  $S$ . The auxiliary conditions are set by the mass and momentum restrictions. We end up with the following set of equations:

$$\frac{\partial S}{\partial z_i} + \lambda_\rho + \left\langle \vec{\lambda}_{\rho\vec{u}}, \vec{c}_i \right\rangle = 0, \quad (3.73)$$

$$\mu_m \sum_i z_i - \rho = 0, \quad (3.74)$$

$$\mu_m \sum_i z_i \vec{c}_i - \vec{j} = 0. \quad (3.75)$$

where  $\lambda_\rho$  and  $\vec{\lambda}_{\rho\vec{u}}$  are Lagrange multipliers. Solving the first equation we get

$$z_i^{eq} = \bar{z}_i \exp \left( \lambda_\rho + \left\langle \vec{\lambda}_{\rho\vec{u}}, \vec{c}_i \right\rangle \right). \quad (3.76)$$

The Lagrange multipliers are calculated by inserting the expression for the equilibrium distribution  $z_i^{eq}$  into the auxiliary conditions. Since the exact calculation is difficult we make a power series expansion in  $u$  and neglect terms of order  $\mathcal{O}(u^3)$ . We finally arrive at

$$f_i^{eq} = \rho a^{c_i} \left( 1 + \frac{\vec{u}\vec{c}_i}{s_1} + \frac{(\vec{u}\vec{c}_i)^2}{2s_1^2} - \frac{u^2}{2s_1} \right). \quad (3.77)$$

For a detailed derivation see [20, 19].

### 3.3.3 Boundary Conditions

Every lattice Boltzmann model needs a strategy to treat the boundaries of its simulation domain. Since the simulation domain is built from elementary lattice Boltzmann cells, the form of the boundary depends on the special geometry of these cells just like the form of a Lego castle depends on its Lego bricks.

Lattice Boltzmann literature [53, 64] distinguishes between two types of boundaries, node boundaries and link boundaries. While in node boundaries the grid points are on the boundary line, in link boundaries the boundary lines go through the connecting line between the grid points.

By now, various classes of boundary conditions are established in lattice Boltzmann. Due to their simplicity, periodic boundary conditions and no slip boundary conditions are used in most lattice Boltzmann models.

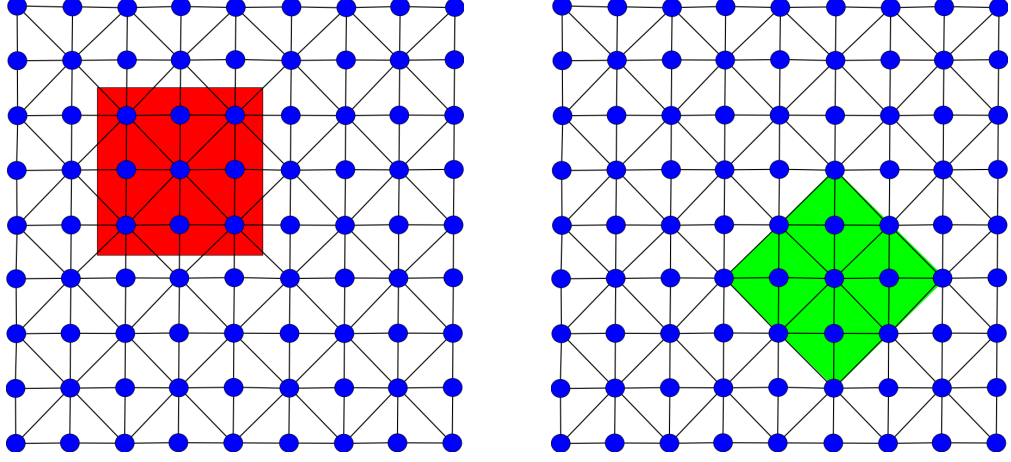


Figure 3.3: left-hand side: link boundary, right-hand side: node boundary

**Periodic boundary conditions** Periodic boundary conditions are chosen if boundary effects (wall or surface effects) are not of interest [53]. The simulation domain is assumed to be square or a rectangle. If a particle distribution now leaves the domain through the left boundary it appears again at the right boundary and, similarly if a particle distribution goes through the top boundary it appears again on bottom boundary line. The edges get a special treatment: On every edge the particle distributions in the direction of the walls are bounced back as in the no slip boundary condition [53, 64].

**No slip boundary conditions** The no slip boundary condition corresponds to a solid wall boundary with a certain roughness, so that there is zero fluid velocity parallel to the wall. The particles are just bounced back from the wall. The no slip boundary conditions solves this situation in the following way: There is no collision step for boundary particles and in the streaming step the particle distributions remain at the same grid point but are streamed to the opposite velocity direction [53, 64].

A general numerical remark that is valid also for lattice Boltzmann is that the accuracy of the boundary scheme should be the same as the accuracy of the actual numerical scheme. Since lattice Boltzmann is of a second order in accuracy, every lattice Boltzmann boundary scheme should be at least of second order. Otherwise the whole lattice Boltzmann model is down-graded to first order.

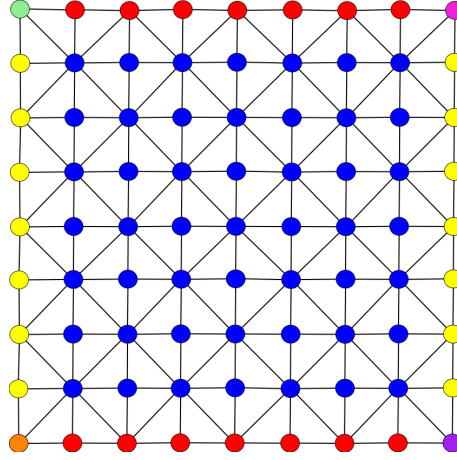


Figure 3.4: D2Q9 lattice with periodic boundary conditions, lattice points of the same colour are neighbours, the edge points get a special treatment: the particle distributions are bounced back from the wall like in the no slip boundary condition

### 3.3.4 Implementation

Now we have all the information to implement a standard lattice Boltzmann model. The box below sketches how such an implementation could look like.

- initialize fields: density, fluid-velocity, momentum density,...
- initialize neighbours: generate and save information about neighbourhood (with boundary conditions)
- calculate equilibrium distributions  $f_i^{eq}$  from initial fields
- (only in the first iteration step)  
set distributions:  $f_i = f_i^{eq}$
- collision step: we solve  $f_i^*(\vec{x}_j, t_0) = \frac{1}{-\tau} [f_i(\vec{x}_j, t_0) - f_i^{eq}(\vec{x}_j, t_0)]$
- streaming step: we stream  $f_i^*(\vec{x}_j, t_0)$  to its neighbours  
 $f_i^*(\vec{x}_j, t_0) = f_i(\vec{x}_{ni(j)})$  where  $ni$  is the  $i^{th}$  neighbour of  $\vec{x}_j$
- calculate new fields from the new distributions  $f_i$
- calculate the new  $f^{eq}$  from the newly calculated fields

Most lattice Boltzmann models have a core program structure similar to the one in the box above. The basic algorithm is then augmented to be

suitable the for specific problem it is applied on. For example in the lattice Boltzmann model for spinodal decomposition of Swift et al. [54] one has to define two lattice Boltzmann equations, one for the density of the whole fluid, and one for the density difference of fluid A and fluid B (see Chapter 2).

## 3.4 Fluctuating Lattice Boltzmann Method

It turns out that fluctuations are important for modelling physical effects at the mesoscopic scale. Therefore a lot of work has been done in order to include thermodynamically correct fluctuations into the lattice Boltzmann scheme. See for example refs. [20, 18, 1]. This section follows the formalism of ref. [19].

### 3.4.1 Multi-Relaxation-Time Model (MRT)

The multi-relaxation-time model can be viewed as generalization of the the lattice BGK model. Instead of multiplying  $(f_i - f_i^{eq})$  with the relaxation time factor  $-1/\tau$  we apply a linear transformation  $\mathcal{L}_{ij}$ . Subsequently, the lattice Boltzmann equation changes to

$$f_i^* = f_i + \sum_j \mathcal{L}_{ij} (f_j - f_j^{eq}). \quad (3.78)$$

The new collision operator  $\Delta_i = \sum_j \mathcal{L}_{ij} (f_j - f_j^{eq})$  offers the possibility to refine the collision process. In real fluids, the viscous modes and the stress modes are relaxed at different time scales, while the hydrodynamic modes mass density and momentum density are conserved. So, in order to be able to relax all those modes independently, the relaxation matrix needs to have a special form. Such relaxation matrices can then be diagonalized by an eigenbasis  $e_{ki}$  consisting polynomials in the normalized velocity vectors  $\hat{c}_i = \vec{c}_i / \|\vec{c}_i\|$ .  $\mathcal{L}_{ij}$  can then be written as

$$\mathcal{L}_{ij} = \sum_k \epsilon_k e_{ki} e_{kj}, \quad (3.79)$$

where the  $\lambda_k$  denote the eigenvalues. In addition, all distribution functions  $f_i$  can be mapped to an equal number of moments of the distribution functions  $m_k$

$$m_k = \sum_i e_{ki} f_i, \quad (3.80)$$

---

and vice versa the moments of the distribution functions can be mapped to the distribution functions

$$f_i = \sum_k e_{ki} m_k. \quad (3.81)$$

Note that this bijective mapping is of course only possible if the model has at least as many lattice velocities  $c_i$  as there are modes. While the eigenbasis is already orthogonal, we still need to normalize the  $e_{ki}$  by setting

$$\hat{e}_{ki} = e_{ki} \frac{\sqrt{a^{c_i}}}{\sqrt{w_k}}, \quad (3.82)$$

where  $w_k > 0$  is a weight given by

$$w_k = \sum_i a^{c_i} e_{ki}^2. \quad (3.83)$$

The normalized transformation then results in

$$\hat{m}_k = \frac{m_k}{\sqrt{w_k}} = \sum_i \hat{e}_{ki} \hat{f}_i, \quad (3.84)$$

$$\hat{f}_i = \frac{f_i}{\sqrt{w_k}} = \sum_k \hat{e}_{ki} \hat{m}_k, \quad (3.85)$$

for the distribution function and its moments and

$$\hat{\mathcal{L}}_{ij} = \sqrt{\frac{a^{c_j}}{a^{c_i}}} \mathcal{L}_{ij} \quad (3.86)$$

for the relaxation matrix. In table 3.1 a valid choice for the eigenbasis vectors for D2Q9 model is given as illustration. As stated before, the moments of the distribution functions are directly related to the modes as you can see in this example for a D2Q9 model:

$$\rho = m_0, \quad (3.87)$$

$$j_x = m_1 c, \quad (3.88)$$

$$j_y = m_2 c, \quad (3.89)$$

$$P_{xx} = (m_0 + m_3 + m_4) \frac{c^2}{3}, \quad (3.90)$$

$$P_{yy} = (2m_0 + 2m_3 - m_4 + 3m_5) \frac{c^2}{6}, \quad (3.91)$$

$$P_{xy} = m_6 c^2, \quad (3.92)$$

$$(3.93)$$

| $k$ | $e_{ki}$                           | $w_k$ |
|-----|------------------------------------|-------|
| 0   | 1                                  | 1     |
| 1   | $\hat{c}_{ix}$                     | 1/3   |
| 2   | $\hat{c}_{iy}$                     | 1/3   |
| 3   | $3\hat{c}_i^2 - 2$                 | 4     |
| 4   | $2\hat{c}_{ix}^2 - \hat{c}_i^2$    | 4/9   |
| 5   | $\hat{c}_{ix}\hat{c}_{iy}$         | 1/9   |
| 6   | $(3\hat{c}_i^2 - 4)\hat{c}_{ix}$   | 2/3   |
| 9   | $(3\hat{c}_i^2 - 4)\hat{c}_{iy}$   | 2/3   |
| 8   | $9\hat{c}_i^4 - 15\hat{c}_i^2 + 2$ | 1/16  |

Table 3.1: This table shows a valid choice of eigenvectors  $e_{ki}$  and corresponding weights  $w_k$  of the D2Q9 model. Table taken from [20].

where  $\rho$  denotes the density,  $J_x$  and  $J_y$  denote the components of the velocity density, and  $P_{xx}$ ,  $P_{yy}$  and  $P_{zz}$  denote the diagonal elements of the pressure tensor. Note that moments  $m_7$ ,  $m_8$  and  $m_9$  do not correspond to any physical modes. They are called kinetic or ghost moments and obviously, they are needed for a bijective mapping of the moments onto the distribution functions.

By combining equation 3.78, equation 3.84 and equation 3.85 we derive a lattice Boltzmann equation for the moments

$$\hat{m}_k^* = \hat{m}_k + \epsilon_k(\hat{m}_k - \hat{m}_k^{eq}). \quad (3.94)$$

For the conserved modes  $m_0, \dots, m_n$  it  $\gamma_k$  can be set to an arbitrary value since  $m_k^* - m_k^{eq} = m_k - m_k^{eq} = 0$ . For the modes  $m_k$  with  $k > n$   $\epsilon_k$  is restricted to  $-2 \leq \epsilon_k \leq 0$  because of stability issues.

### 3.4.2 Introduction of Fluctuations

One way to introduce fluctuations into an lattice Boltzmann model is to add a stochastic term  $\Delta'_i$  to the collision operator [19]. The operator then changes to

$$\Delta_i = \sum_j \mathcal{L}_{ij} (f_j - f_j^{eq}) + \Delta'_i. \quad (3.95)$$

The stochastic part of the collision operator has to fulfil conservation of momentum and mass:

$$\sum_i \Delta'_i = \sum_i \Delta'_i c_{i\alpha} = 0, \quad \alpha = 1, 2. \quad (3.96)$$



---

We require the mean value of the stochastic operator to be zero, i.e  $\langle \Delta'_i \rangle = 0$ , as this ensures correct thermodynamic behaviour in the macroscopic limit. Furthermore, the collision operator is constructed to be local in time and space. Drawn to the macroscopic limit via Chapman-Enskog expansion, a collision operator defined in this way yields the isothermal Navier Stokes equations with a Gaussian random stress term. The amplitude  $S_{rand}$  of this random stress is given by

$$S_{rand} = \sqrt{\mu_m \rho} c_s^2, \quad (3.97)$$

where  $\mu_m$  is the mass density parameter given by  $\mu_m = \frac{m_p}{l^d}$  with  $m_p$  as the particle mass,  $l$  as the lattice spacing and  $d$  as the dimension. The other quantities are the density  $\rho$  and the speed of sound,  $c_s$ . Note that the fluctuations in the density distribution functions then have an amplitude of  $s_{rand} = \sqrt{\mu_m \rho}$ . When normalizing the distribution functions and the moments, we have to account for the amplitude of the fluctuations:

$$\hat{f}_i = \frac{f_i}{\sqrt{a^{c_i} \mu_m \rho}}, \quad (3.98)$$

$$\hat{m}_k = \frac{m_i}{\sqrt{w_k \mu_m \rho}}. \quad (3.99)$$

**Implementation** An update rule, that is consistent with the constraints stated above, is given by

$$\hat{m}_k^* = \hat{m}_k + \epsilon_k (\hat{m}_k - \hat{m}_k^{eq}) + \phi_k r_k. \quad (3.100)$$

This is the linear relaxation equation 3.94 enhanced by a Gaussian random variable  $r_k$  multiplied by a variable  $\phi_k$ . The mean value of this Gaussian random variable has is zero and the variance is one. The variable  $\phi_k$  is chosen such that the transition  $m \rightarrow m^*$  fulfils detailed balance and is given by

$$\phi_k = \sqrt{-\epsilon(2 + \epsilon)}. \quad (3.101)$$

Detailed balance in fluctuating lattice Boltzmann ensures that the relaxation process is towards the correct thermal equilibrium. For the conserved modes  $m_k$ ,  $k = 0, \dots, d$  we apply  $\epsilon = 0$  which leads to  $m_k^* = m_k$  as intended. For the other hydrodynamic modes,  $\epsilon$  is restricted by the limits of linear stability with  $-2 \leq \epsilon \leq 0$ . Note for  $\epsilon = -1$  only the random term and the local equilibrium value  $m^{eq}$  remains in equation 3.100 and therefore the information of the previous value is almost completely lost.



# Chapter 4

## Simulation and Results

### 4.1 Deterministic Lattice Boltzmann Model for Binary Fluids

In this section, we give a detailed description of a lattice Boltzmann model for spinodal decomposition introduced by ref.[54].

A binary mixture of two ideal gases A and B is assumed. While the A-A and B-B interactions are set to zero, a repulsive interaction  $\lambda$  between fluid A and fluid B is assumed. Since no thermal fluctuations are included, only spinodal decomposition and no nucleation process should be observed at  $T < T_c$ .

We start with introducing the lattice Boltzmann equations for the particle distribution functions  $f_i(\vec{x}, t)$  and  $g_i(\vec{x}, t)$ . In this model we use two lattice Boltzmann equations, one for the total density  $\rho(\vec{x}, t)$  and one for the density difference  $\phi(\vec{x}, t)$ ,

$$f_i(\vec{x} + \vec{e}_i \delta t, t + \delta t) - f_i(\vec{x}, t) = \frac{-1}{\tau_1} (f_i - f_i^{eq}), \quad (4.1)$$

$$g_i(\vec{x} + \vec{e}_i \delta t, t + \delta t) - g_i(\vec{x}, t) = \frac{-1}{\tau_2} (g_i - g_i^{eq}). \quad (4.2)$$

Since the D2Q9 lattice yields higher stability and isotropy we chose the ansatz of [60] which is based on ref. [54]. The velocities of this D2Q9 model are given by  $e_i \in \{(0, 0), (\pm 1, 0), (0, \pm 1), (\pm 1, \pm 1)\}$ . The relation to macroscopic observables is given by the moments of the distribution function. The zeroth moments are the total density and the density difference,

$$\rho(\vec{x}, t) = \rho_A(\vec{x}, t) + \rho_B(\vec{x}, t) = \sum_i f_i = \sum_i f_i^{eq}, \quad (4.3)$$

and

$$\phi(\vec{x}, t) = \rho_A(\vec{x}, t) - \rho_B(\vec{x}, t) = \sum_i g_i = \sum_i g_i^{eq}, \quad (4.4)$$

where  $\rho_A$  denotes the density of fluid A and  $\rho_B$  the density of fluid B. The first moments are the total momentum density and the density difference momentum,

$$\rho u_\alpha = \sum_i f_i e_{i\alpha} = \sum_i f_i^{eq} e_{i\alpha}, \quad (4.5)$$

$$\phi u_\alpha = \sum_i g_i e_{i\alpha} = \sum_i g_i^{eq} e_{i\alpha}. \quad (4.6)$$

Note that the zeroth and the first moment are conserved quantities.

So far, everything has been straight-forward lattice Boltzmann scheme. In order to include the properties of the proposed binary fluid into the lattice Boltzmann model we turn to the macroscopic equations we want to simulate. That is the continuity equation for the density  $\rho(\vec{x}, t)$ ,

$$\frac{\partial \rho}{\partial t} + \frac{\partial \rho u_\alpha}{\partial x_\alpha} = 0, \quad (4.7)$$

and the Navier Stokes equation for the total momentum  $\rho \vec{u}(\vec{x}, t)$ ,

$$\rho \frac{\partial u_\alpha}{\partial t} + \rho u_\beta \frac{\partial u_\alpha}{\partial x_\beta} = \frac{\partial P_{\alpha\beta}}{\partial x_\beta} + \frac{\rho \theta_1 \Gamma}{3} \left( \frac{\partial}{\partial x_\beta} \left( \delta_{\alpha\beta} - 3 \frac{\partial P_{\alpha\beta}}{\partial \rho} \right) \frac{\partial u_\gamma}{\partial x_\gamma} + \frac{\partial u_\beta}{\partial x_\alpha} + \frac{\partial u_\alpha}{\partial x_\beta} \right). \quad (4.8)$$

The density difference obeys the Cahn Hilliard equation plus an advection term,

$$\frac{\partial \phi}{\partial t} + \frac{\partial}{\partial x_\alpha} (\phi u_\alpha) = \theta_2 \Gamma \nabla^2 \mu - \frac{\partial}{\partial x_\beta} \left( \frac{\phi}{\rho} \frac{\partial P_{\alpha\beta}}{\partial x_\alpha} \right), \quad (4.9)$$

with

$$\theta_{1,2} = \tau_{1,2} - \frac{\Delta t}{2}. \quad (4.10)$$

Now, the second moments of  $f_i^{eq}$  and  $g_i^{eq}$  which have the dimension of an energy density are chosen such that the Chapman-Enskog procedure yields the correct macroscopic equations. Subsequently the following form is proposed for the second moments,

$$\sum_i f_i^{eq} e_{i\alpha} e_{i\beta} = P_{\alpha\beta} + \rho u_\alpha u_\beta, \quad (4.11)$$

$$\sum_i g_i^{eq} e_{i\alpha} e_{i\beta} = \Gamma \mu \delta_{\alpha\beta} + \phi u_\alpha u_\beta. \quad (4.12)$$

---

The involved terms are  $P_{\alpha\beta}$ , the pressure tensor,  $\Gamma$ , the mobility and  $\mu$ , the chemical potential.

The pressure tensor and the chemical potential are connected to the Cahn-Hilliard free energy density functional  $\mathcal{F}[\rho, \phi, T]$  in the following way. The Cahn-Hilliard free energy density functional has the following form (see section 2.3 for a detailed description):

$$\mathcal{F}[\rho, \phi, T] = \int d\vec{r} \left( f_0(T, \rho, \phi) + \frac{\kappa}{2} (\nabla \rho)^2 + \frac{\kappa}{2} (\nabla \phi)^2 \right) \quad (4.13)$$

The equilibrium free energy density of a binary mixture is given by [45]

$$f_0(\phi, \rho, T) = \frac{\lambda}{4} \rho \left( 1 - \frac{\phi^2}{\rho^2} \right) - T \rho + \frac{T}{2} (\rho + \phi) \log \left( \frac{\rho + \phi}{2} \right) \quad (4.14)$$

$$+ \frac{T}{2} (\rho - \phi) \log \left( \frac{\rho - \phi}{2} \right). \quad (4.15)$$

The chemical potential is obtained by taking the functional derivative of  $\mathcal{F}[\rho, \phi, T]$ ,

$$\mu(\vec{x}) = \frac{\delta \mathcal{F}[\rho, \phi, T]}{\delta \phi}(\vec{x}) \quad (4.16)$$

$$\Rightarrow \mu(\vec{x}) = \frac{-\lambda \phi}{2 \rho} + \frac{T}{2} \log \left( \frac{1 + \phi}{1 - \phi} \right) - \kappa \nabla^2 \phi. \quad (4.17)$$

Since the calculation of the pressure tensor from the free energy takes more time and tricks, only the result is given here

$$P_{\alpha\beta}(\vec{r}) = p(\vec{r}) \delta_{\alpha\beta} + \kappa \frac{\partial \rho}{\partial x_\alpha} \frac{\partial \rho}{\partial x_\beta} + \kappa \frac{\partial \phi}{\partial x_\alpha} \frac{\partial \phi}{\partial x_\beta}, \quad (4.18)$$

with

$$p(\vec{r}) = \rho T - \kappa (\rho \nabla^2 \rho + \phi \nabla^2 \phi) - \frac{\kappa}{2} (\|\nabla \rho\|^2 + \|\nabla \phi\|^2). \quad (4.19)$$

For a full derivation see ref. [60].

Now we have all the information we need to calculate the equilibrium distributions. We arrive at the following second order expansions in  $\vec{u}$  and  $u\vec{e}_i$

$$f_i^{eq} = A_l + B_l u_\alpha e_{i\alpha} + C_l \|u\|^2 + D_l u_\alpha u_\beta e_{i\alpha} e_{i\beta} + G_{l\alpha\beta} e_{i\alpha} e_{i\beta}, \quad (4.20)$$

and

$$g_i^{eq} = H_l + K_l u_\alpha e_{i\alpha} + J_l \|u\|^2 + Q_l u_\alpha u_\beta e_{i\alpha} e_{i\beta}, \quad (4.21)$$

Appropriate but not unique expressions for the parameters are obtained by inserting equation 4.20 and equation 4.21 into the constraints 4.3 - 4.6 and 4.11 - 4.12. A suitable choice is:

$$A_2 = \frac{1}{8}p_0(\rho, \phi, \nabla^2\phi), A_1 = 2A_2, A_0 = \rho - 12A_2, \quad (4.22)$$

$$B_2 = \frac{\rho}{12}, B_1 = 4B_2, \quad (4.23)$$

$$C_2 = \frac{-\rho}{16}, C_1 = 2C_2, C_0 = \frac{-3\rho}{4}, \quad (4.24)$$

$$D_2 = \frac{\rho}{8}, D_1 = 4D_2, \quad (4.25)$$

$$G_{2xx} = \frac{\kappa}{16} \left( \left( \frac{\partial\phi}{\partial x} \right)^2 - \left( \frac{\partial\phi}{\partial y} \right)^2 \right), \quad (4.26)$$

$$G_{2xy} = G_{2yx} = \frac{\kappa}{8} \frac{\partial\phi}{\partial x} \frac{\partial\phi}{\partial y}, \quad (4.27)$$

$$G_{2yy} = -G_{2xx}, \quad (4.28)$$

$$G_{1xx} = 4G_{2xx}, G_{1xy} = G_{1yx} = 4G_{2xy}, G_{1yy} = 4G_{2yy}, \quad (4.29)$$

$$H_2 = \frac{\Gamma}{8}\mu(\rho, \phi, \nabla^2\phi), H_1 = 2H_2, H_0 = \phi - 12H_2, \quad (4.30)$$

$$K_2 = \frac{\phi}{\rho}B_2, K_1 = \frac{\phi}{\rho}B_1, \quad (4.31)$$

$$J_2 = \frac{\phi}{\rho}C_2, J_1 = \frac{\phi}{\rho}C_1, J_0 = \frac{\phi}{\rho}C_0, \quad (4.32)$$

$$Q_2 = \frac{\phi}{\rho}D_2, Q_1 = \frac{\phi}{\rho}D_1. \quad (4.33)$$

## 4.2 Validity of the Deterministic Model

Before including fluctuations into the model we test the validity of the implementation by reproducing some computer experiments done with that model by refs. [54, 60].

### 4.2.1 Phase Behaviour

First, we reproduce the spinodal line. At this point we should keep in mind, that, since the applied lattice Boltzmann model is based on Cahn-Hilliard theory, the Ginzburg criterion from section 2.3 holds. According to this criterion the spinodal line cannot be determined rigorously in Landau theories. Instead of an abrupt transition from nucleation to spinodal decomposition at

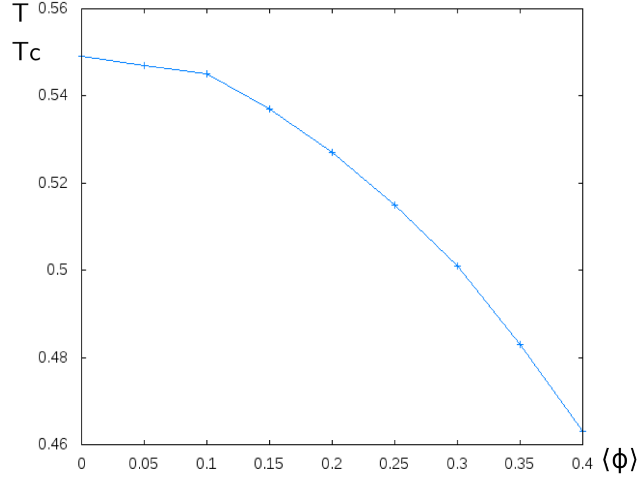


Figure 4.1: This spinodal line is obtained by the implemented version of the deterministic D2Q9 model of ref.[60, 54].

the spinodal a smooth crossover is observed. Hence, just above the spinodal line, the nucleation process adopts properties from spinodal decomposition and just below the spinodal line, spinodal decomposition adopts properties from nucleation. Subsequently, the spinodal we are going to determine can not be viewed as a strict line. Moreover, the obtained line lies in the crossover region from nucleation to spinodal decomposition. In addition, due the absence of fluctuations we should not observe nucleation. But according to the Ginzburg criterion we should expect the spinodal decomposition to show properties of nucleation.

Practically a point on the spinodal line  $(T_s, \phi_s)$  is obtained by performing simulations with fixed average density difference  $\langle\phi\rangle$  and varying the temperature. The first of these simulation runs starts with a temperature well above or below the spinodal line and in the subsequent runs temperature is step by step quenched or raised by a finite amount until phase separation is observed. The resulting phase diagram (see figure 4.1) coincides with the results obtained by refs. [54, 60]. Note that in all simulations, the lattice length was set to  $lx = 128$  and the mobility  $\Gamma = 2.0$ .

**Temperature Quenches at  $\langle\phi\rangle = 0$**  At first we look at the case where the average density difference  $\langle\phi\rangle$  is zero i.e where the fluid contains an equal amount of fluid A and fluid B. We start with a random initial configuration  $\phi(\vec{x}, 0)$  which corresponds to the mixed state and set the temperature to a value beneath the spinodal. Immediately, small domains of fluid A or

respectively fluid B form. When domains of the same kind meet they coalesce. The pattern that develops is meander-like. In the course of time this pattern coarsens until the fully phase separated equilibrium structure is formed. In the case of  $\langle\phi\rangle$ , the equilibrium pattern is represented by stripes (See figure 4.2 for the development of the patterns at  $\langle\phi\rangle = 0$ ).

When the binary fluid is quenched to the critical temperature  $T_c$  and if  $\langle\phi\rangle = 0$  we observe a second order phase transition. In ref. [61], Wagner and Yeomans showed that the domain coarsening follows a power law for intermediate times. To be precise they showed that a typical length scale grows according to the power law

$$R(t) \approx (t - t_0)^{1/3}. \quad (4.34)$$

At late times this growth law breaks down due to hydrodynamic effects. See section 2.1 and ref. [61] for more information. Note that we did not reproduce this scaling law results but wanted to point these findings out to the reader.

**Temperature Quenches at  $\langle\phi\rangle \neq 0$**  Now we deal with the situation where  $\langle\phi\rangle \neq 0$ , which means that the fluid either contains more particles of fluid A than of fluid B, or vice versa. Due to this asymmetry, we observe a different pattern than in the case where  $\langle\phi\rangle = 0$ . In fact, already a slight asymmetry in the composition results in the formation of bubbles of the minor phase with the major phase as environment. The growth of the bubbles lasts until the limit of interaction between the like-particles is reached. The equilibrium configuration of the case  $\langle\phi\rangle \neq 0$  is represented by one or more bubbles of the minor phase in the major phase (see figure 4.3). If the mobility is low we observe Lifshitz-Slyozov growth as described in [7]:

At the beginning there are a lot of clusters with different sizes. But in the course of time, the big clusters grow further while smaller clusters shrink and finally vanish. This growth and shrinking processes can be explained by the diffusion field that exists due to the random particle diffusion between the clusters. The gradient of this field then points to the larger clusters and therefore they tend to gain particles at the cost of the smaller clusters. Usually this growth also follows a power law but as we didn't test it we can not confirm the power law for this system.

Up to now, we described spinodal decomposition events after a deep quench into the spinodal region. Now we will turn to analyse quenches for  $\langle\phi\rangle \neq 0$  just beneath the spinodal. For this purpose we carried out simulations with  $\langle\phi\rangle = 0.3$  and as already suggested, the obtained results indicate that in this case, spinodal decomposition does also have properties of a nucleation process (see figure 4.4). The properties the transition inherits from nucleation



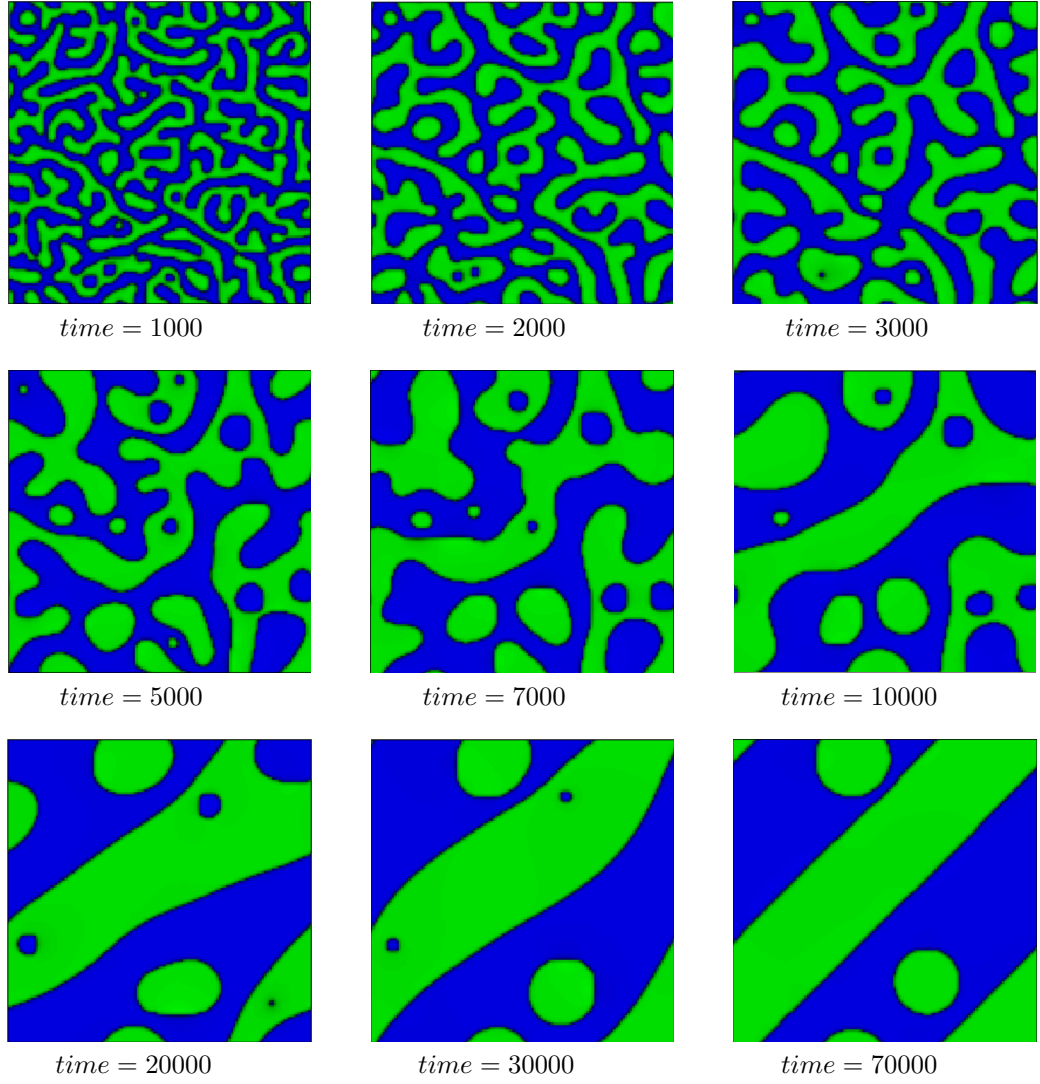


Figure 4.2: These figures show the development of the density difference field  $\phi(\vec{x}, t)$  during a the spinodal decomposition with different average density difference  $\langle\phi\rangle = 0$ . The choice of the other parameters is:  $T = 0.510$ ,  $\kappa = 0.010$ ,  $\Gamma = 2.0$ .

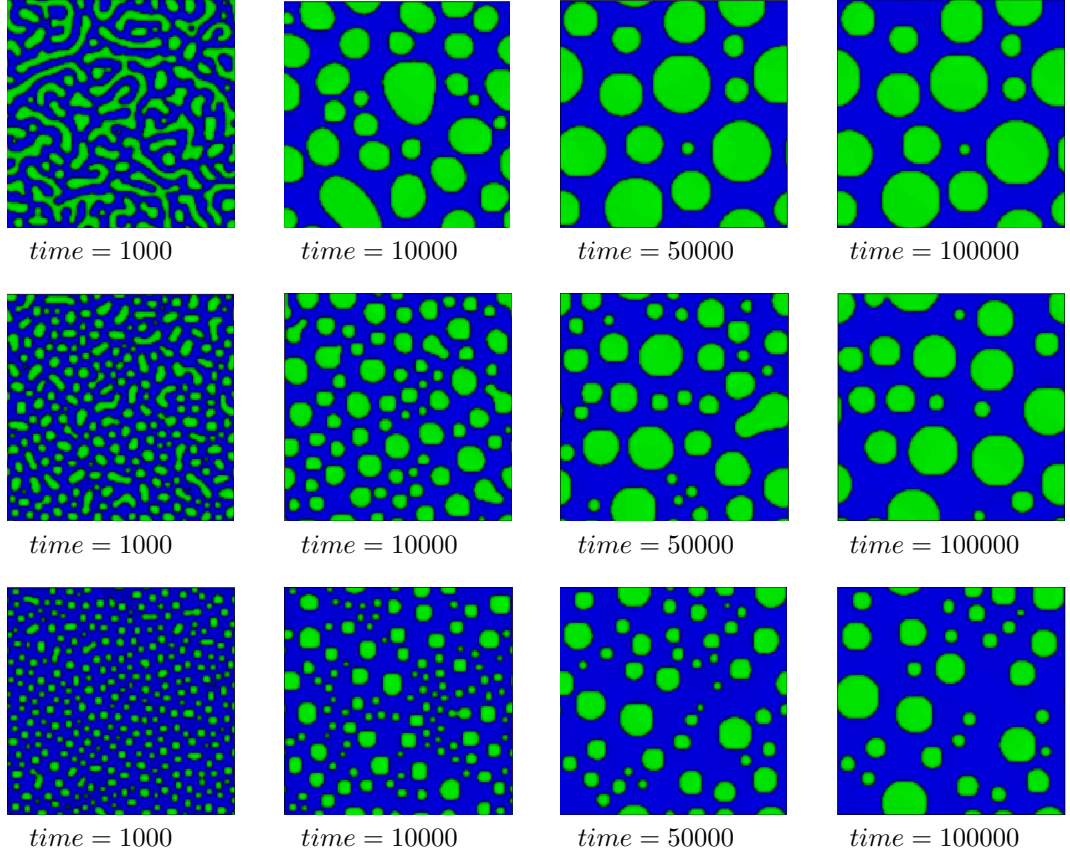


Figure 4.3: These figures show the development of the density difference field  $\phi(\vec{x}, t)$  during a the spinodal decomposition with different average density differences  $\langle \phi \rangle \neq 0$ . In the first line we have  $\langle \phi \rangle = 0.03$ , in the second line  $\langle \phi \rangle = 0.1$  and in the third line  $\langle \phi \rangle = 0.2$ . The choice for the other parameter is:  $T = 0.51$   $\kappa = 0.010$ ,  $\Gamma = 2.0$ .

are that the transition does not start at the beginning but only at  $t \approx 10000$  and that only one nucleus forms. In this sense, we interpret our observation as example for an non-physical crossover effect which occur near the spinodal in Landau theories (see ref.[6] and section 2.3).

#### 4.2.2 Influence of $\kappa$

Simulation experiments by ref.[54] show that the surface tension coefficient  $\kappa$  influences the thickness of the interface between fluid A and fluid B. To be precise, at high  $\kappa$  they found that the interface between the fluids is much thicker than at lower values. In order to further test the validity of the implemented version of the model proposed by ref. [54] we reproduced these measurements and indeed, the results in figure 4.6 are in agreement with

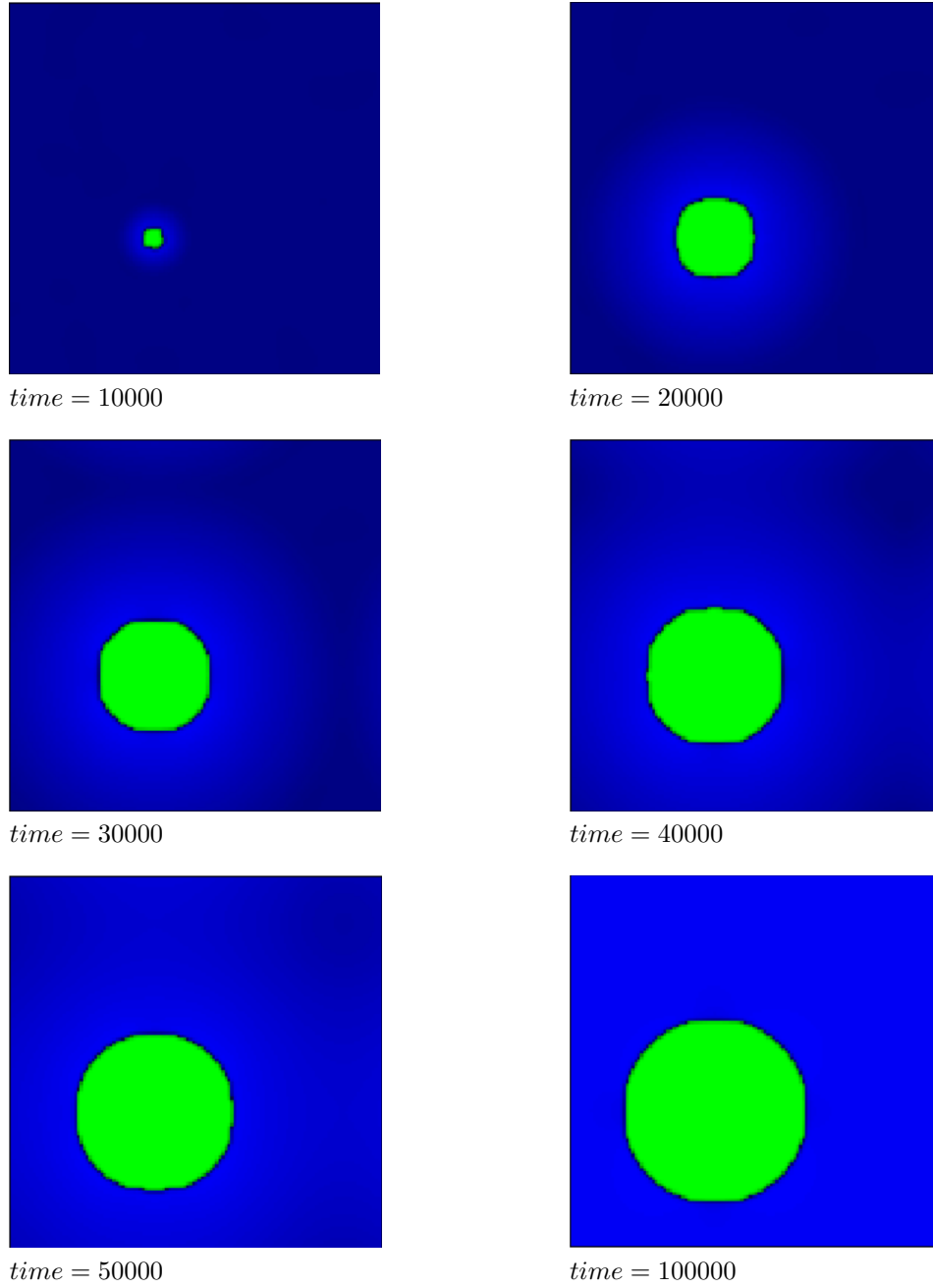


Figure 4.4: These plots show the development of the density difference field  $\phi(\vec{x}, t)$  during a the spinodal decomposition near to the spinodal. The average density difference is  $\langle \phi \rangle = 0.3$ . Since this simulation is carried out near to the spinodal, it is suggested that the transition is in the crossover region between spinodal decomposition and nucleation. Hence we interpret the fact that the transition only starts at  $time \approx 10000$  because this as property the transition inherited from as feature adopted from nucleation. The choice for the other parameters is: The lattice length is  $lx = 128$ , the surface tension coefficient is  $\kappa = 0.010$  and the temperature is  $T = 0.501$ .

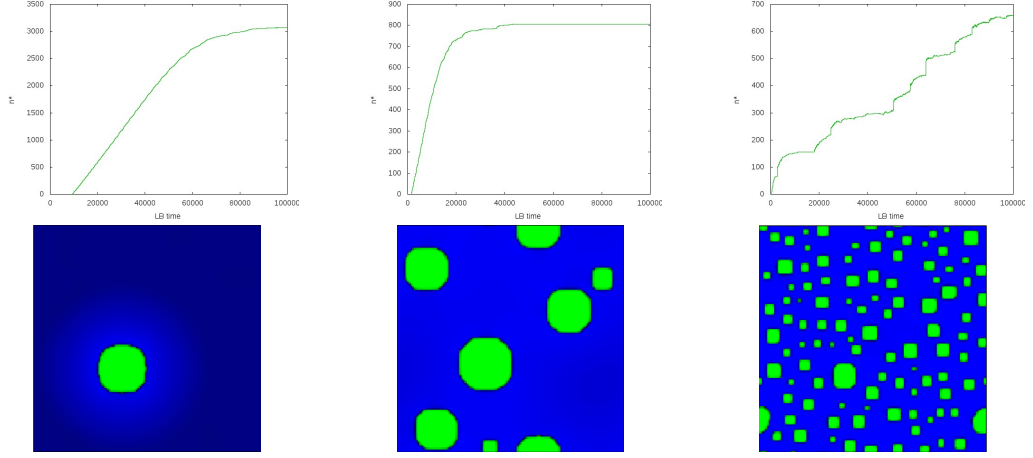


Figure 4.5: Comparison of simulation runs with  $\langle \phi \rangle = 0.3$  at different temperatures. In the first line the size of the largest cluster is plotted as function of time for  $T = 0.501$ ,  $T = 0.500$  and  $T = 0.495$  (from the left to the right). In the second line we plotted the corresponding density difference fields at  $time = 20000$ . While at  $T = 0.501$  we observe a crossover behaviour (see also figure 4.4.), at  $T = 0.500$  and  $T = 0.495$  we observe a typical spinodal decomposition.

ref. [54].

In addition we observe that at very low  $\kappa$  values the phase transition does not take place at all. In order to explain this we remark that the surface tension is proportional to  $\kappa$ . So, if the surface tension which is the force holding particles of the same kind together, is small, all developing clusters break apart again and no phase separation transition can take place.

### 4.2.3 Structure Factor

In simulations on the molecular level the dynamical structure factor  $S(\vec{k}, t)$  is often used to compare the simulation results with experiments as  $S(\vec{k}, t)$  can also be determined by scattering experiments [3]. Conventionally, the definition of the structure factor uses the microscopic density  $\rho(\vec{r}) = \sum_i^N \delta(\vec{r} - \vec{r}_i)$  and yields [3]

$$S(\vec{k}, t) = \frac{1}{N} \left\langle \hat{\rho}(\vec{k}, t) \hat{\rho}^*(\vec{k}, t) \right\rangle, \quad (4.35)$$

where  $\hat{\rho}(\vec{k}, t)$  denotes the spatial Fourier transform of the density and  $\hat{\rho}^*(\vec{k}, t)$  its complex conjugate. As the density is a coarse grained quantity in lattice systems, the structure factor has to be adapted to the form [60]

$$S(\vec{k}_m, t) = \left\langle \frac{1}{N} \left| \sum_{j=0}^{lx \cdot ly} \exp(i\vec{k}_m \cdot \vec{x}_j) \rho_{av}(\vec{x}_j, t) \right|^2 \right\rangle, \quad (4.36)$$

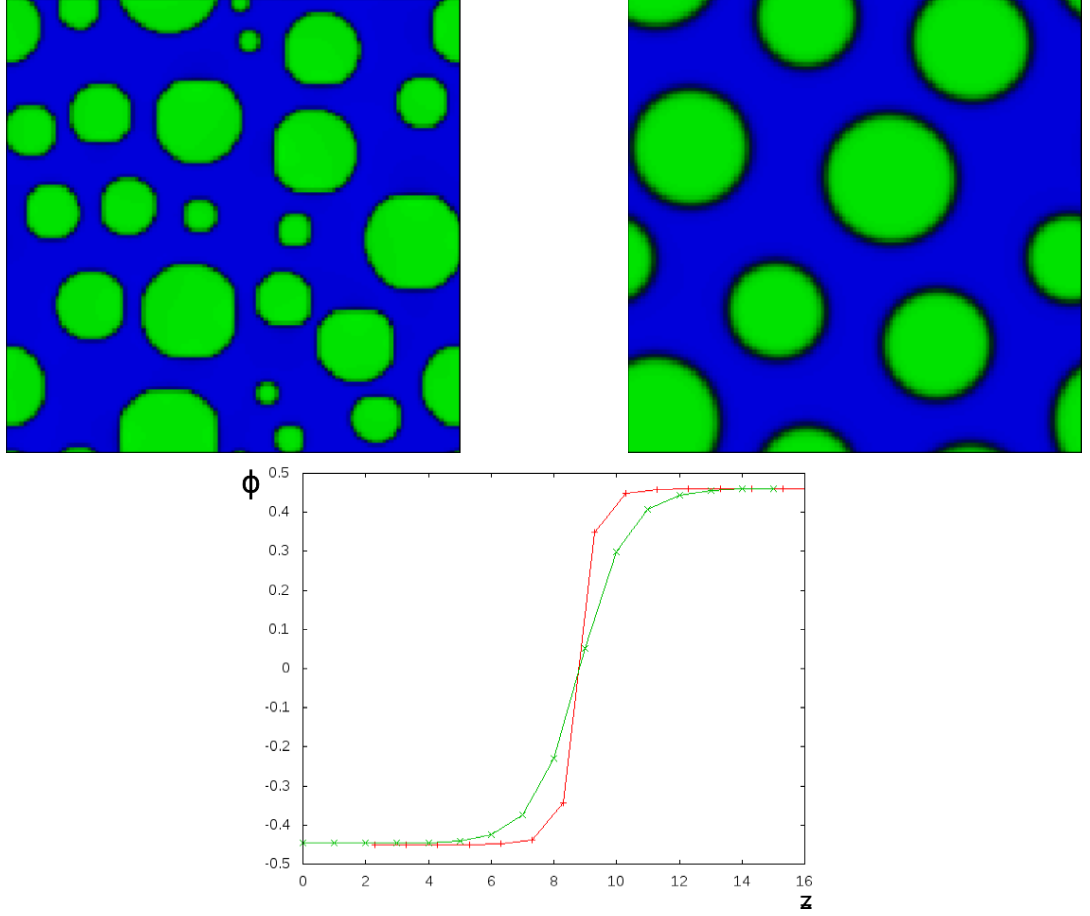


Figure 4.6: These figures show the dependence of the thickness of the interface on  $\kappa$ . The red line corresponds to the density difference field on the left picture and to  $\kappa = 0.010$ , and the green line corresponds to to the density difference field on the right picture and to  $\kappa = 0.050$ . Note that  $z$  denotes a direction perpendicular to the interface. The choice for the other parameter is:  $lx = 128$ ,  $\langle \phi \rangle = 0.1$ ,  $T = 0.510$ ,  $\Gamma = 2.0$ .

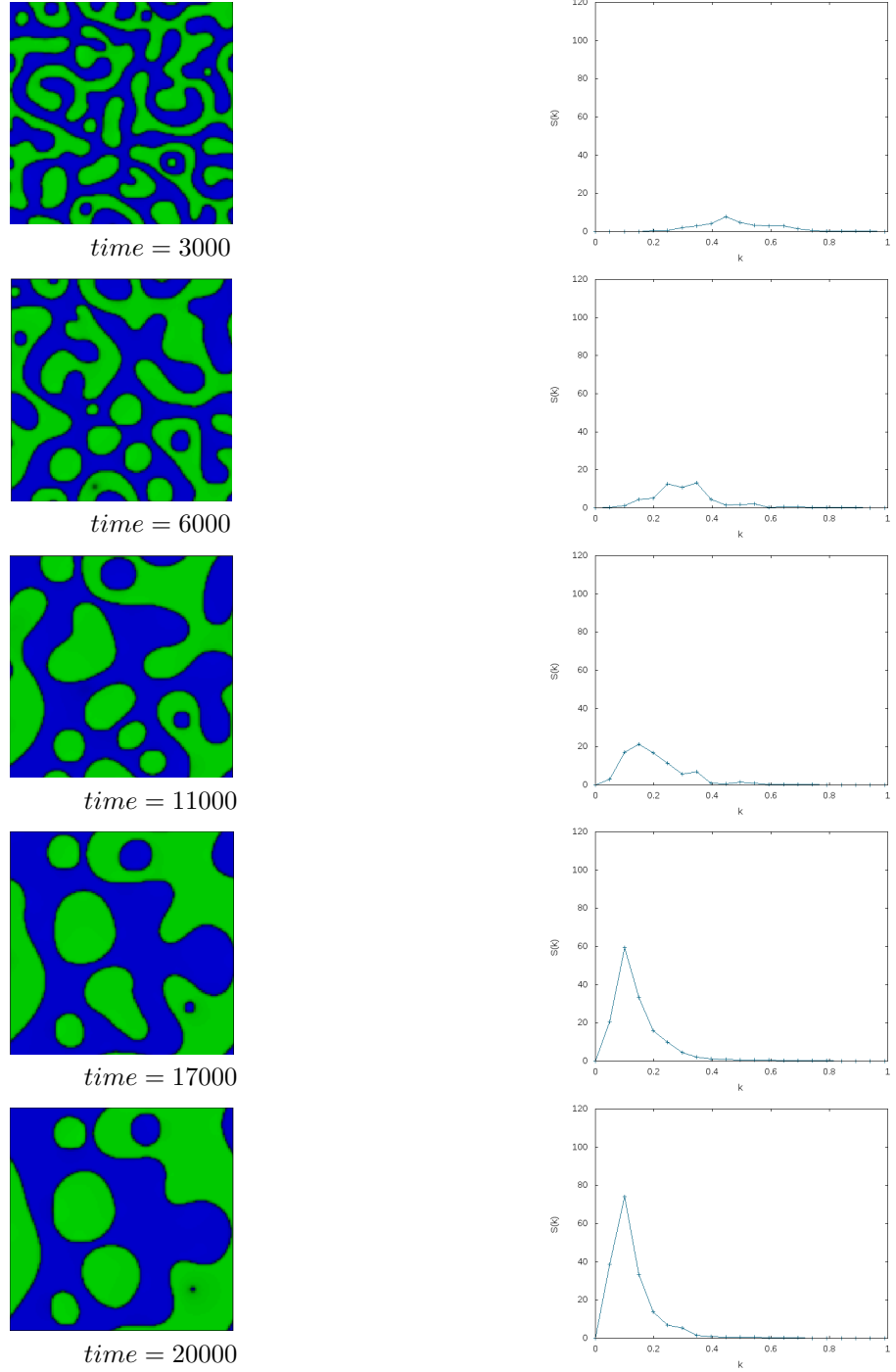


Figure 4.7: In this figure we tracked the development of the circularly averaged structure factor. The plots of the circularly averaged structure factor are on the right, while on the left can see the parallel development of the density difference field. At  $time = 3000$  a small peak has developed. At later times, the peaks transforms into a double peak and even later the double peak changes again to a single peak. Furthermore the peak grows and its maximum shifts gradually to smaller  $k$ -values.

---

where  $\vec{k}_m$  is given by

$$\vec{k}_m = 2\pi \left( \frac{x_m}{l_x^1} \hat{e}_x + \frac{y_m}{l_y} \hat{e}_y \right). \quad (4.37)$$

Note that  $\rho_{av}$  denotes an averaged density, in our case we set  $\rho_{av} \equiv \phi(\vec{x}, t)$ . From the structure factor we can easily obtain the circularly averaged structure factor

$$S(k, t) = \frac{\sum_{m^*} S(\vec{k}_{m^*}, t)}{\sum_{m^*} 1}, \quad (4.38)$$

where  $k = 2\pi a/l_{min}$  with  $a = 0, \dots, l_{min}$  and  $l_{min} = \min(l_x, l_y)$ . The sum over  $m^*$  denotes the summation over all  $\vec{k}_m$  in the shell between  $2\pi(a-0.5)/l_{min} \leq |k| \leq 2\pi(a+0.5)/l_{min}$ .

We again performed quenching experiments with the implemented model and thereby calculated the circularly averaged structure factor for different times. Figure 4.7 represents the typical development of the structure factor of the model during a spinodal decomposition. Shortly after the temperature quench a shallow peak develops in  $S(k, t)$ . At intermediate times, the peak transforms into a double peak and later it becomes a single peak again. In the course of time the peak gradually shifts to lower  $k$ -values and thereby grows. The described development of the structure factor of this model is in very good agreement with results obtained from similar lattice Boltzmann models [36, 16] and with results obtained from a Monte Carlo simulation of the non-linear Cahn-Hilliard equation [33].

### 4.3 Fluctuating Lattice Boltzmann Model for Binary Fluids

Having validated our implementation of the lattice Boltzmann model for binary fluids of Swift et al. [54] and Wagner [60], we now implement fluctuations into the model following the ansatz of Duenweg et al. [19] described in section 3.4. We start with the two deterministic lattice Boltzmann single relaxation time equations of the model,

$$f_i(\vec{x} + \vec{e}_i \delta t, t + \delta t) - f_i(\vec{x}, t) = \frac{-1}{\tau_1} (f_i - f_i^{eq}), \quad (4.39)$$

$$g_i(\vec{x} + \vec{e}_i \delta t, t + \delta t) - g_i(\vec{x}, t) = \frac{-1}{\tau_1} (g_i - g_i^{eq}), \quad (4.40)$$

and transform them into fluctuating multi relaxation time equations for the moments of the  $f_i$  and the  $g_i$ ,

$$\hat{m}_k(\vec{x} + \vec{e}_k \delta t, t + \delta t) = \hat{m}_k(\vec{x}, t) + \epsilon_k^1(\hat{m}_k - \hat{m}_k^{eq}) + \xi_k^1 r_k^1, \quad (4.41)$$

$$\hat{h}_k(\vec{x} + \vec{e}_k \delta t, t + \delta t) = \hat{h}_k(\vec{x}, t) + \epsilon_k^2(\hat{h}_k - \hat{h}_k^{eq}) + \xi_k^2 r_k^2, \quad (4.42)$$

where  $m_k$ , denote the moments of  $f_i$ , while  $h_k$  denote the moments of  $g_i$ . Again,  $\xi^1$  and  $\xi^2$  are variables that are adjusted so that the transformation  $m \rightarrow m^*$  and  $h \rightarrow h^*$  fulfils detailed balance,

$$\xi^1 = \sqrt{-\epsilon_k^1(2 + \epsilon_k^1)} \quad (4.43)$$

$$\xi^2 = \sqrt{-\epsilon_k^2(2 + \epsilon_k^2)}. \quad (4.44)$$

$$(4.45)$$

The  $r_k^1$  and  $r_k^2$  are Gaussian random variables with a zero mean value and and with a variance of one.

**Implementation** In order implement the fluctuating lattice Boltzmann model described above we need to make a few changes in our algorithm. Instead of the distribution functions  $f_i$  and  $g_i$  we now use the moments  $m_k$  and  $h_k$  to calculate the moments of the distribution function. Furthermore we need a certain amount of Gaussian random variables for every time step. We use an inbuilt random number generator which yields uniformly distributed random numbers and transform them into Gaussian random variables through a Monte Carlo process.

## 4.4 Analysis and Results

### 4.4.1 Cluster Analysis Tools

At each time step  $t_j$ , we calculate the density field,  $\rho(\vec{x}_i, t_j)$ , the density difference field  $\phi(\vec{x}_i, t_j)$  and the velocity vector field  $\vec{u}(\vec{x}_i, t_j)$  for the new time step. For cluster analysis, we need solely the density difference field as it tells us at which fraction the lattice site is occupied by fluid A and/or by fluid B. To be more specific, we are interested in the size of the biggest cluster  $n^*$  of the minor phase and in the distribution of cluster sizes  $n$  before the nucleation event. From distribution of cluster sizes we can calculate the scaled probability distribution of all cluster sizes  $P(n)$ . As the size of the biggest cluster dramatically changes when the nucleation process takes place,



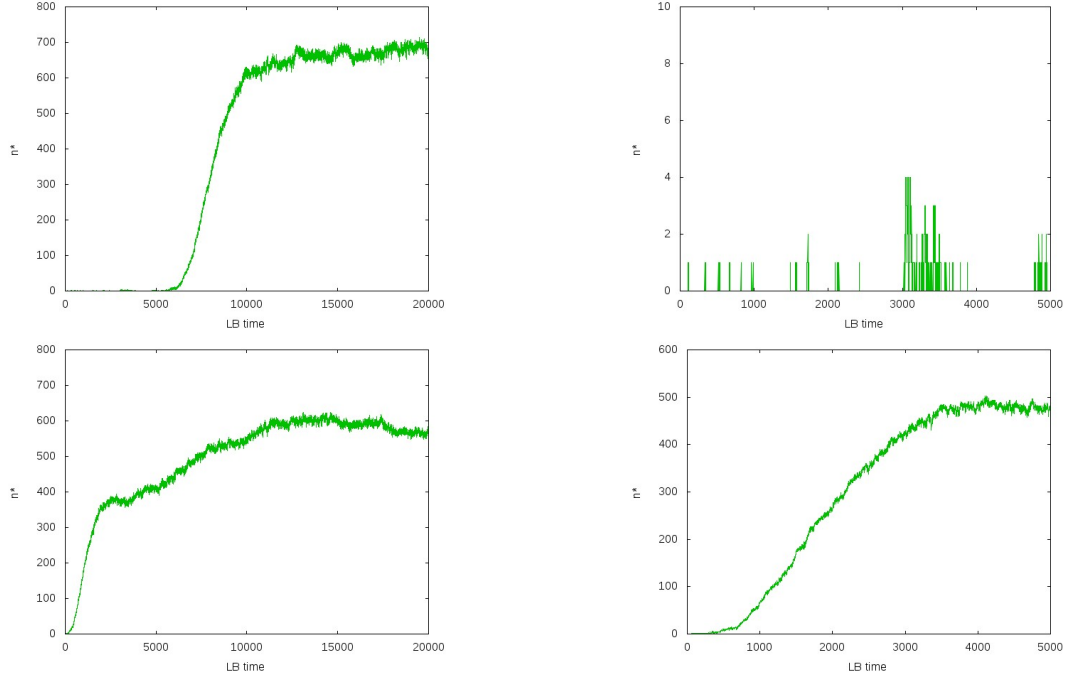


Figure 4.8: In the first line a typical form for  $n^*$  for a nucleation event is shown. At the first 5000 LB-time steps  $n^*(t)$  fluctuates around a cluster size of  $n^* = 3$ . After about 6000 time steps the system undergoes a nucleation process and then fluctuations around  $n^* = 7000$ . The second line shows a typical spinodal decomposition event. The transition starts right at the beginning.

$n^*$  can be viewed as an order parameter of the transition. Therefore we plot the size of the largest cluster as function of time,  $n^*(t_j)$  and assume the time where  $n^*$  starts to increase rapidly as the starting point of the nucleation event. Furthermore we can write down the free energy as function of  $n^*$ :

$$F(n^*) = -\log P(n^*). \quad (4.46)$$

In addition, we can calculate the probability distribution of the size of the largest cluster  $P(n^*)$

The free energy  $F(n^*)$  and the size of the largest cluster in time  $n^*(t)$  are useful measures to distinguish nucleation from spinodal decomposition. Spinodal decomposition occurs if there is no or only a very small free energy barrier of the order of  $k_B T$  between the current supercooled mixed state and the stable phase separated state, whereas nucleation occurs only at the presence of a noticeable energy barrier, i.e if  $\Delta F \gg k_B T$ . In simulations the problem is that, unless we apply special free-energy calculation methods, we will not obtain the whole free energy barrier.

Furthermore, when a system undergoes a nucleation process, we expect the

size of largest cluster,  $n^*(t)$  to fluctuate around a lower value until, all of a sudden,  $n^*$  begins to grow up to a certain equilibrium size.

On the other hand, if the system phase separates via spinodal decomposition we expect the phase transition to start right at the beginning of the simulation and in addition more than one nucleus should develop at once. Typical plots of  $n^*(t)$  where the system on the one hand phase separates via spinodal decomposition and on the other hand phase separates via nucleation are shown in figure 4.8.

We are also interested how spherical the simulated clusters are on the average. The related quantity is called asphericity  $A_s$  and can be determined via the eigenvalues of the gyration tensor [49, 59]

The components of gyration tensor are given by

$$Q_{\alpha\beta} = \frac{1}{2N^2} \sum_{i,j=1}^N (x_{i\alpha} - x_{j\alpha})(x_{i\beta} - x_{j\beta}), \quad \text{with } \alpha, \beta = 1, \dots, d, \quad (4.47)$$

where  $d$  is the dimension of the cluster,  $N$  is the number of particles in the cluster and the double sum runs over all pairs of particles in the cluster. The asphericity of a cluster is then calculated by using the eigenvalues  $\lambda_\alpha$  of the gyration tensor

$$\langle A_s \rangle = \left\langle \frac{\sum_{\alpha < \beta} (\lambda_\alpha - \lambda_\beta)^2}{\sum_\alpha (\lambda_\alpha)^2} \right\rangle. \quad (4.48)$$

For a two-dimensional system,  $\langle A_s \rangle$  is then given by

$$\langle A_s \rangle = \frac{(\lambda_1 - \lambda_2)^2}{(\lambda_1 + \lambda_2)^2}. \quad (4.49)$$

#### 4.4.2 Influence of $\kappa$ on the Nucleation Process

We investigated how a change in the surface tension coefficient  $\kappa$  influences the nucleation process. For this purpose we carried out simulations with surface tension coefficients ranging from  $\kappa = 0.001$  to  $\kappa = 0.025$ . For these tests, the value of the fluctuation amplitude was fixed to  $B_f = 0.008$  and the average density difference between fluid A and fluid B is set to  $\langle \phi \rangle = 0.4$ . For all simulation runs, the lattice length was set to  $lx = 128$  and the mobility was set to  $\Gamma = 2.0$ .

But, before starting with analysing the results we would like to state a general remark: We found that  $\kappa$  and the amount of fluctuations in  $n^*$  are coupled in the sense that as we set  $\kappa$  to a fixed high value and raise the fluctuation amplitude  $B$ , we observe that at higher fluctuations in  $n^*$ , the nucleation process

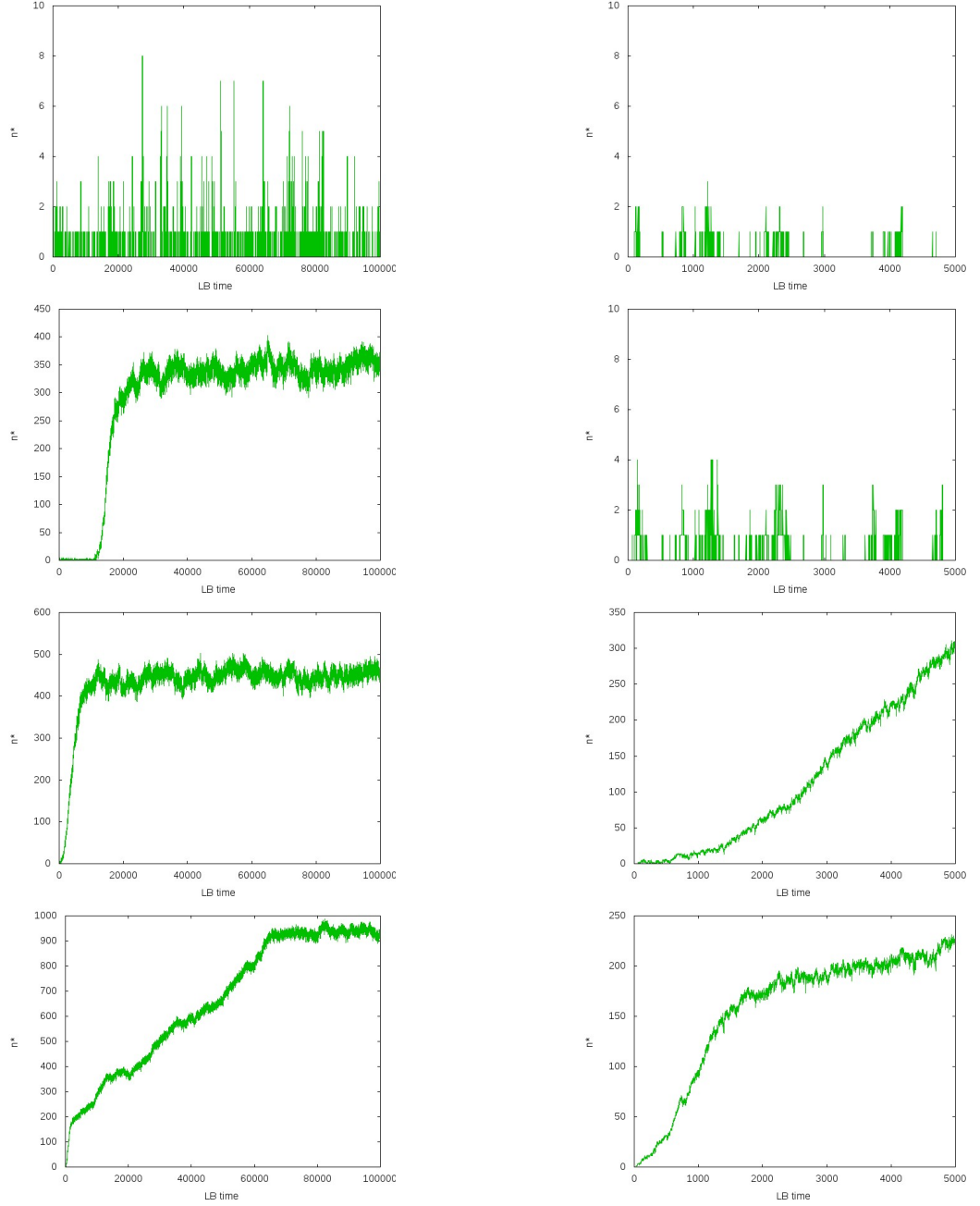


Figure 4.9: These plots show the size of the biggest cluster as function of time at different temperatures. The surface tension coefficient has the value  $\kappa = 0.007$ , the fluctuation amplitude  $B_f = 0.008$  and the mean density difference  $\langle \phi \rangle = 0.4$ . Each line represents one temperature run plotted for different time intervals. first line:  $T = 0.510$ , second line:  $T = 0.509$ , third line:  $T = 0.508$ , fourth line:  $T = 0.503$ . The only difference between these plots the plots in figure 4.13 is that here  $\kappa = 0.007$ , whereas in figure 4.13  $\kappa = 0.015$ . In comparison with figure 4.13, we observe more and frequent fluctuations in  $n^*(t)$  before the transition and that the transition occurs at  $T = 0.509$ , while in figure 4.13 it occurs at  $T = 0.507$ .

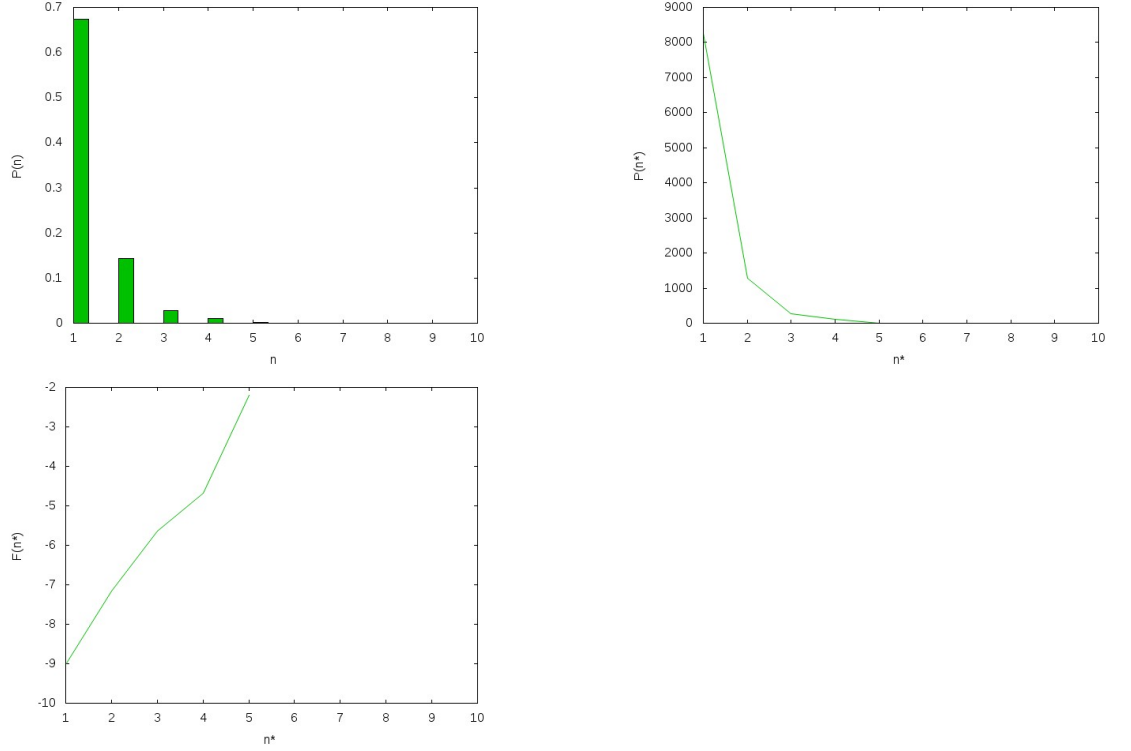


Figure 4.10: In this figure we see the probability distribution of cluster sizes  $P(n)$  (first line, on the left), the probability distribution of the size of the largest cluster,  $P(n^*)$  (first line, on the right) and the free energy  $F(n^*)$  (second line) as function of the size of the largest cluster  $n^*$ . Those three plots are taken from the simulation run of figure 4.9 with the temperature  $T = 0.509$ .

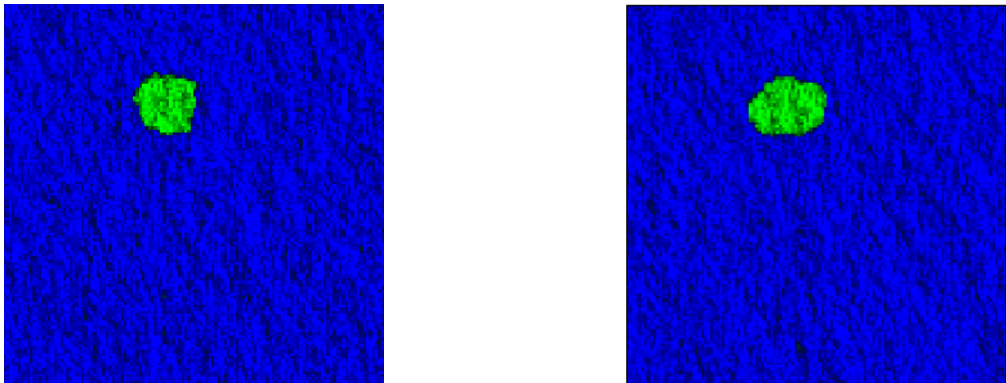


Figure 4.11: These are snapshots of the density difference field  $\phi(\vec{x}, t)$  taken at  $time = 20000$  (on the left) and  $time = 100000$  (on the right) from the simulation run of figure 4.9 at  $T = 0.509$ . We see an developed cluster after the nucleation process.



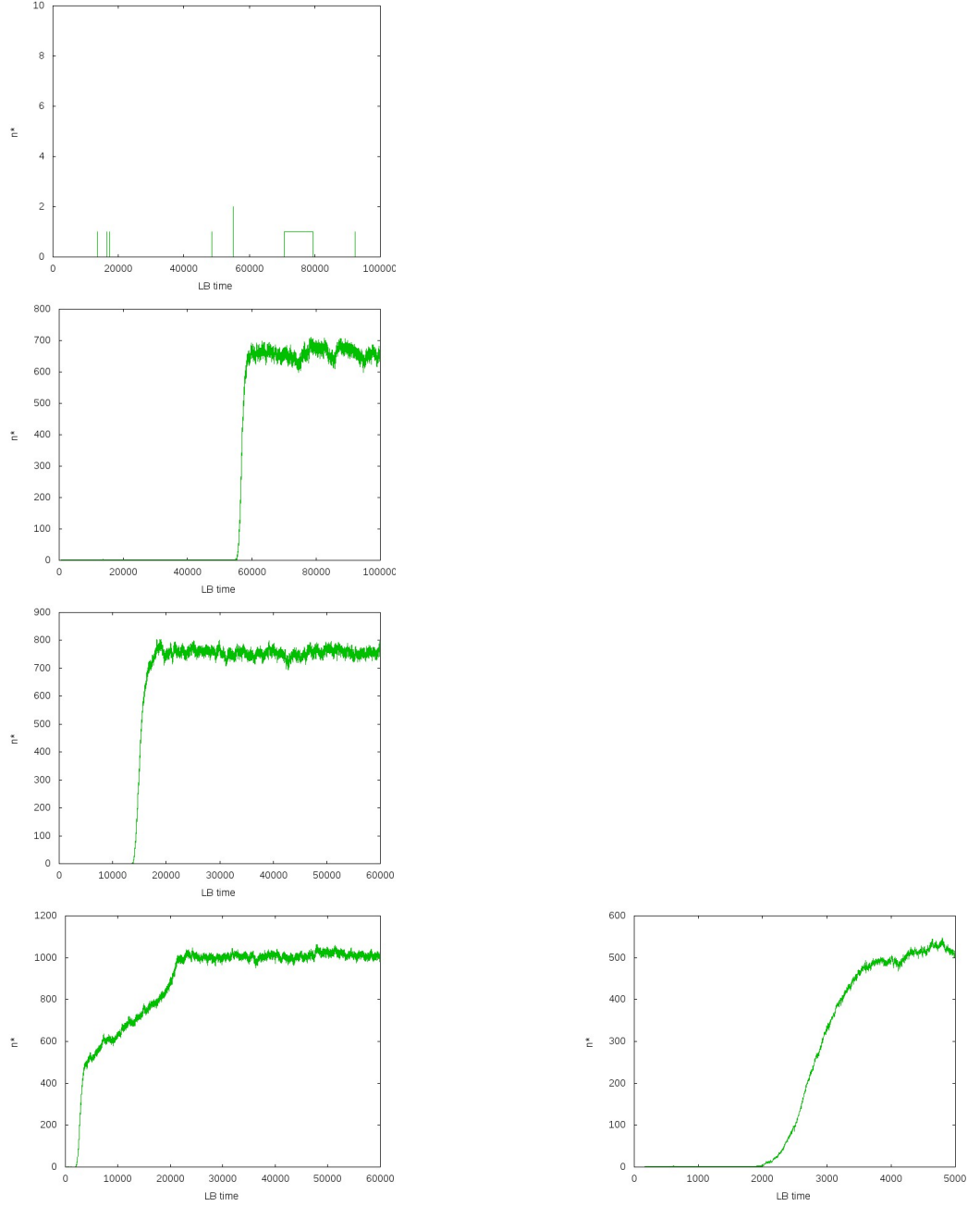


Figure 4.13: These plots show the size of the biggest cluster as function of time at different temperatures  $T$ . The surface tension coefficient has the value  $\kappa = 0.015$ , the fluctuation amplitude  $B_f = 0.008$  and the mean density difference  $\langle \phi \rangle = 0.4$ . Each line represents one temperature run plotted for different time intervals. first line:  $T = 0.507$ , second line:  $T = 0.506$ , third line:  $T = 0.505$ , fourth line:  $T = 0.502$ . The only difference between these plots the plots in figure 4.9 is that here  $\kappa = 0.015$ , whereas in figure 4.13  $\kappa = 0.007$ . In comparison with figure 4.13, we observe no or only very few and small fluctuations in  $n^*(t)$  before the transition. In addition the transition occurs at  $T = 0.507$ , while in figure 4.9 it occurs at  $T = 0.509$ .

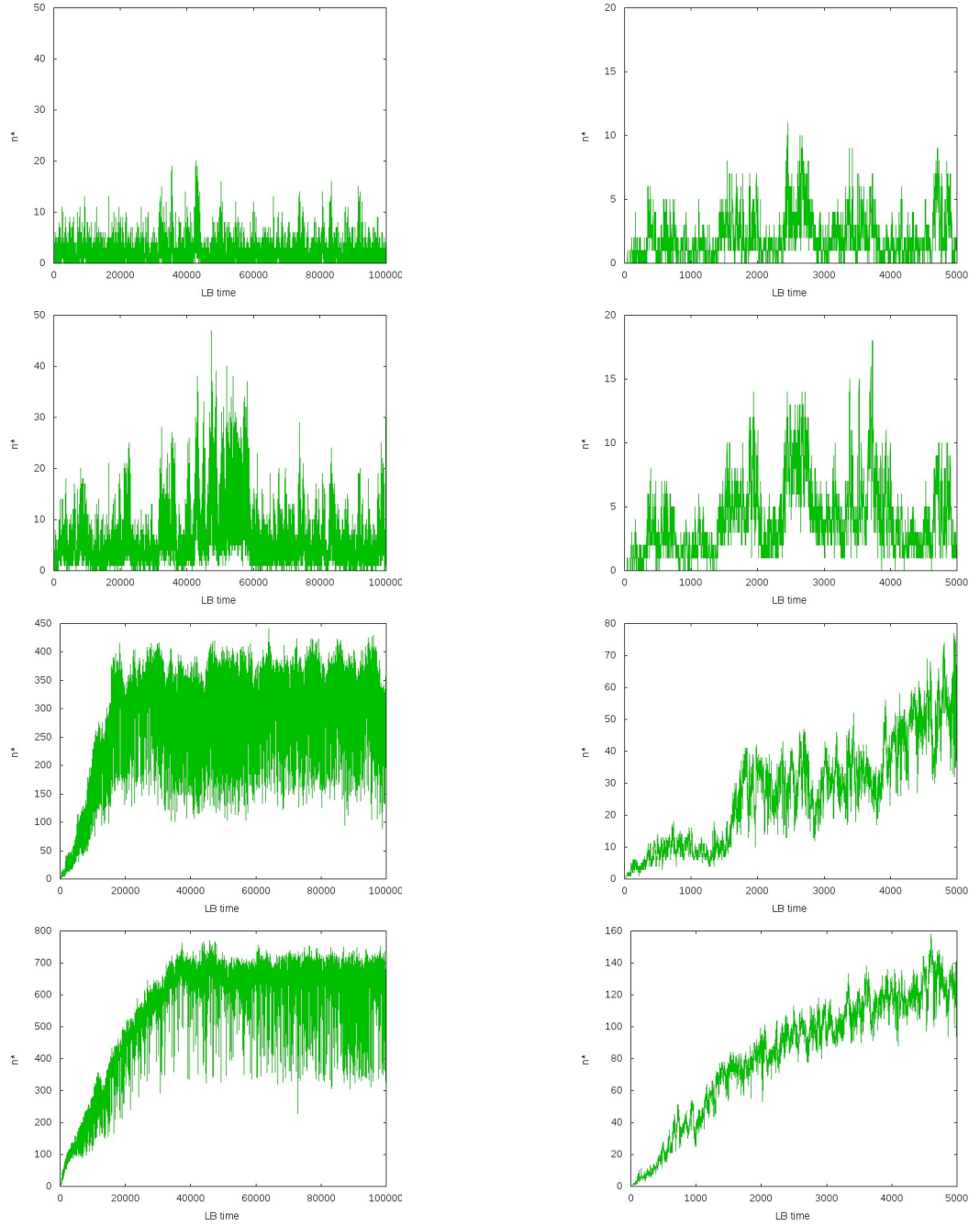


Figure 4.14: These plots show the size of the biggest cluster as function of time at different temperatures. The surface tension coefficient has the value  $\kappa = 0.007$ , the fluctuation amplitude  $B_f = 0.008$  and the mean density difference  $\langle \phi \rangle = 0.3$ . Each line represents one temperature run plotted for different time intervals. first line:  $T = 0.525$ , second line:  $T = 0.524$ , third line:  $T = 0.522$ , fourth line:  $T = 0.520$ . In this simulation runs, we only observe spinodal decomposition but not nucleation because the fluctuations are high in comparison to the  $\kappa$  value and therefore the barrier can be crossed easily.

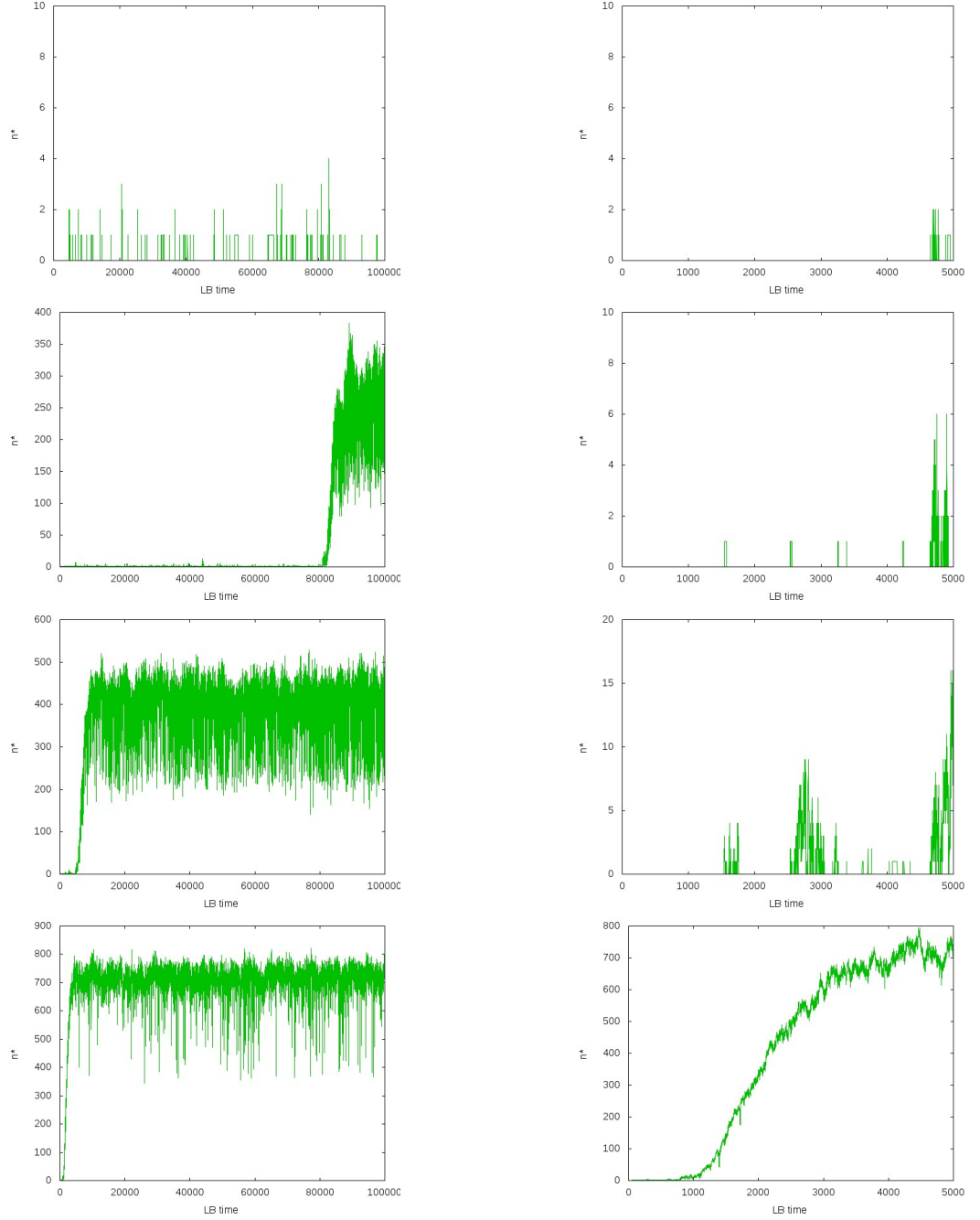


Figure 4.15: These plots show the size of the biggest cluster as function of time at different temperatures. The surface tension coefficient has the value  $\kappa = 0.019$ , the fluctuation amplitude  $B_f = 0.008$  and the mean density difference  $\langle \phi \rangle = 0.3$ . Each line represents one temperature run plotted for different time intervals. first line:  $T = 0.525$ , second line:  $T = 0.524$ , third line:  $T = 0.523$ , fourth line:  $T = 0.520$ . The only difference between these plots and the plots in figure x is that here  $\kappa$  is set to 0.019 whereas in figure 4.14  $\kappa = 0.007$ . Subsequently, fluctuations in  $n^*(t)$  are smaller and occur more infrequent than in figure 4.14 and in contrast to then, we observe a nucleation process.



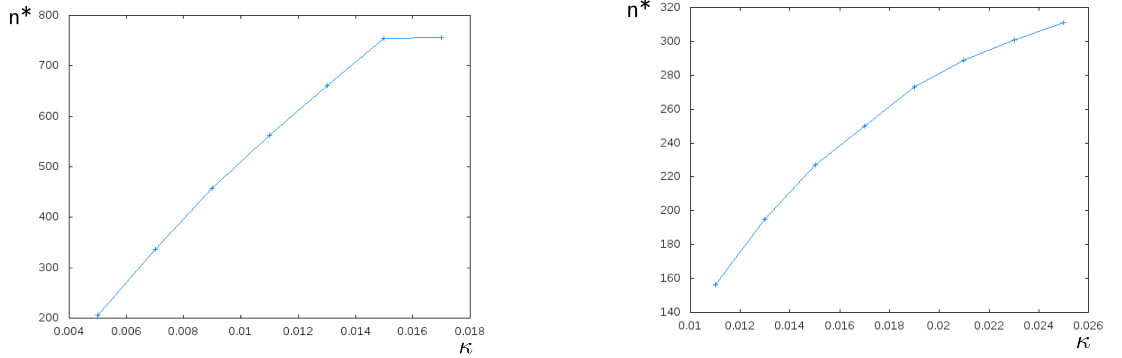


Figure 4.16: In this plot we see the dependence of the size of the cluster that crosses the nucleation barrier as function of  $\kappa$ . The simulation parameter for the plot on the left are:  $\langle \phi \rangle = 0.4$  and  $B_f = 0.008$ . The simulation parameter for the plot on the right are:  $\langle \phi \rangle = 0.3$  and  $B_f = 0.008$ .

is effectively the same than at a lower  $\kappa$  and a lower fluctuation amplitude. Therefore, from now on we will use the terms "effektive fluctuations" and "effektive  $\kappa$ " indicating that the resulting plots also depend on the relation of those two quantities.

Now, we start our analysis with very low  $\kappa$  values. In this case, no transition of any kind is observed, because all developing clusters break apart again. In this context, we remark that  $\kappa$  is the proportionality factor that tunes the gradient terms in the in the Cahn-Hilliard free energy density (see section ?? ). Therefore, if  $\kappa$  becomes very low, the binary fluid behaves like an homogeneous fluid and no phase transition can take place. At intermediate  $\kappa$  values e.g. at  $\kappa = 0.007$ , permanent fluctuations of  $n^*$  are observed (see figure 4.9) above as well as beneath the transition temperature. Comparing simulations at different temperatures reveals the transition from nucleation to spinodal decomposition: the system nucleates at earlier times as the temperature is set to lower values and finally the system starts to phase separate right at the beginning. What is more, if the transition starts at the beginning, the development of more than one cluster at the same time has been observed in all simulation runs (see for example the simulation run with  $T = 0.503$  from figure 4.9 and the corresponding snapshot of the density difference in 4.12). At high  $\kappa$  values, the development of clusters is suppressed. For example at  $\kappa = 0.015$ , we observe very small fluctuations in  $n^*$  above the transition temperature, whereas beneath the transition temperature no or very few and small fluctuations in  $n^*$  occur until the first significant fluctuation leads to the transition. In general we note that in the case of intermediate effective  $\kappa$  values, the non-physical crossover effects from Cahn-Hilliard theory are weaker

than at high effective  $\kappa$  values: At intermediate  $\kappa$  values the process that is identified as spinodal decomposition near the spinodal starts very close to the beginning of the simulation and in addition a couple of bubbles develop distributed over the whole simulation domain, whereas at high effective  $\kappa$  values, the a spinodal decomposition near the spinodal starts not directly at the beginning and most of the time only one bubble develops (compare figures 4.9 and 4.13 for illustration).

Another thing we observed is that at high  $\kappa$  values, the fully developed nucleus grows to a larger size in comparison with simulations done at intermediate values (see figure 4.16). In addition, the transition happens at a significantly later time and at a lower temperature compared to simulation runs carried out at a lower  $\kappa$  value. Over a certain  $\kappa$  value, the development of clusters becomes very unlikely and then a transition does not take place at all.

At high  $\kappa$  values where a transition is still observed, the only difference that remains between spinodal decomposition and nucleation events even far from the spinodal is that nucleation starts at a later times, whereas spinodal decomposition starts rather at the beginning.

Many of those observations can be explained using classical nucleation theory. We start with remarking that  $\kappa$  is proportional to the surface tension, and the numerical value of the surface tension sets the height of the nucleation barrier in classical nucleation theory,

$$\Delta F(R^*) = \frac{16\pi\gamma^3}{3\Delta\mu^2}, \quad (4.50)$$

where  $\gamma$  denotes the surface tension and  $\Delta\mu$  is the difference in the chemical potential between the old equilibrium state and the new metastable one. A higher  $\kappa$  yields a higher nucleation barrier and the higher the nucleation barrier is, the more difficult it becomes for the clusters to cross the barrier or even to form in the first place.

#### 4.4.3 Influence of the Fluctuation Amplitude on the Nucleation Process

As the presence of fluctuations is crucial for the nucleation process, we carried out simulations with different fluctuation amplitudes and compared them. At this point, we remark that fluctuations in  $n^*$  do not only depend on the fluctuation amplitude but also on  $\langle\phi\rangle$ , i.e. fluctuations in  $n^*$  are much larger at  $\langle\phi\rangle = 0.3$  than they are at  $\langle\phi\rangle = 0.4$  at the same fluctuation amplitude. For illustration, compare for example figure 4.14 and figure 4.9. The reason for

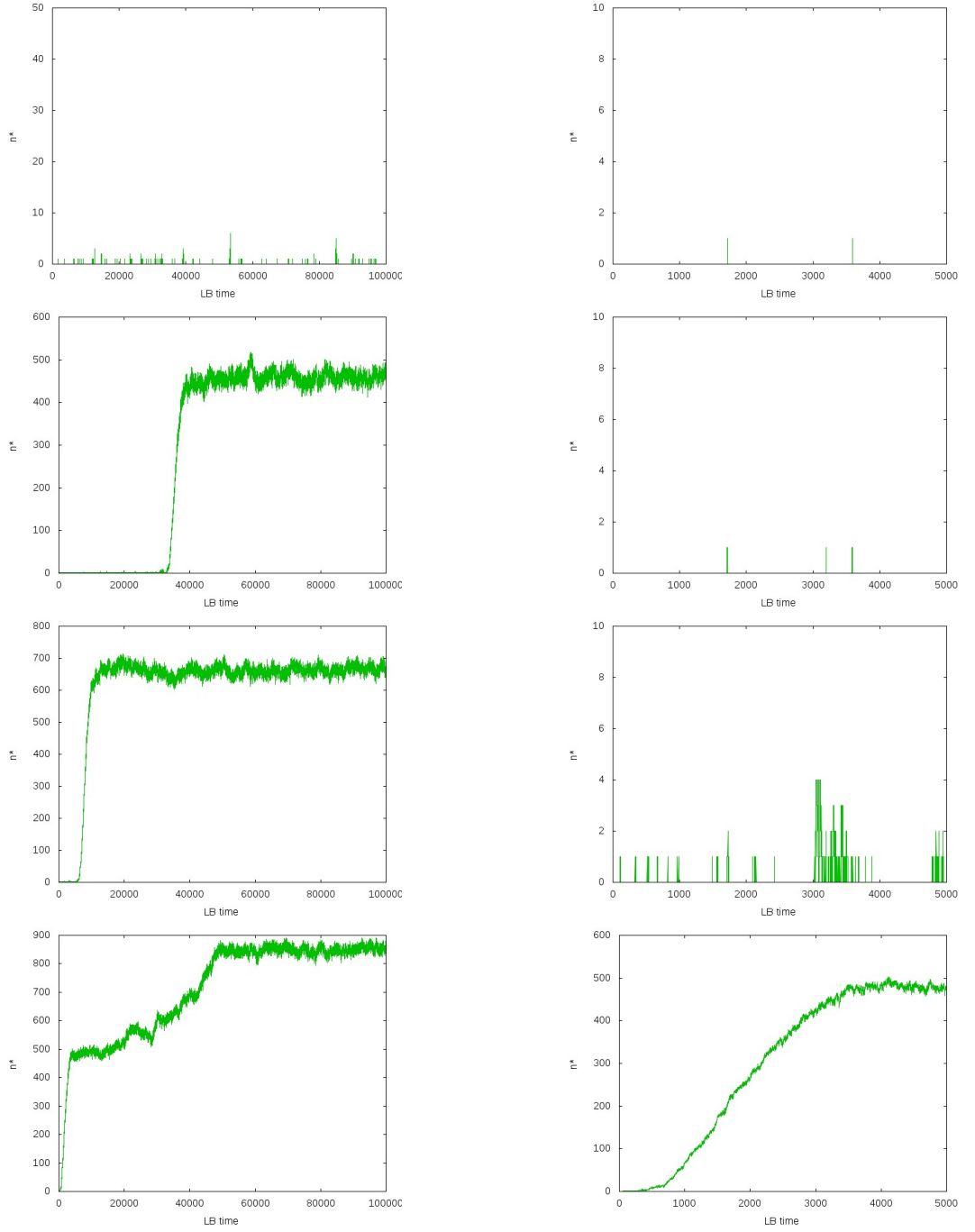


Figure 4.17: These plots show the size of the biggest cluster as function of time at different temperatures  $T$ . The surface tension coefficient has the value  $\kappa = 0.01$ , the fluctuation amplitude  $B_f = 0.008$  and the mean density difference  $\langle \phi \rangle = -0.4$ . Each line represents one temperature run plotted for different time intervals. first line:  $T = 0.509$ , second line:  $T = 0.508$ , third line:  $T = 0.506$ , fourth line:  $T = 0.504$ . The only difference between these plots and the plots in figure 4.19 is that here  $B_f$  is set to 0.008, whereas in figure 4.19  $B_f = 0.005$ .

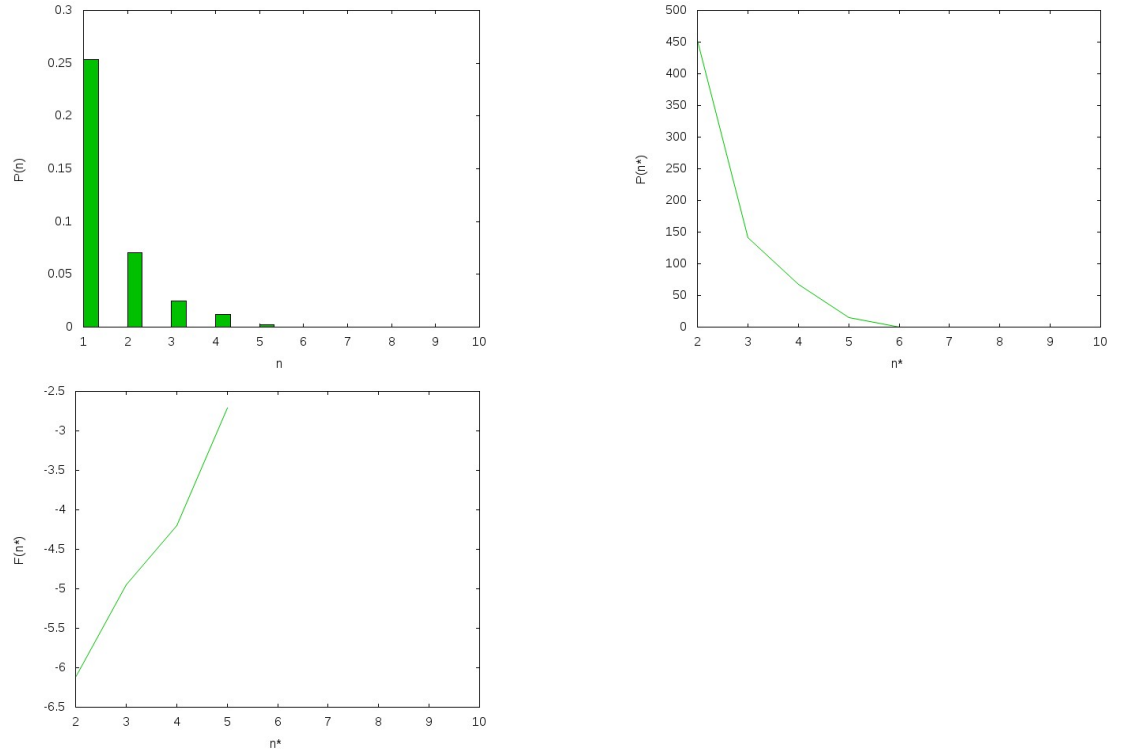


Figure 4.18: In this figure we see the probability distribution of cluster sizes  $P(n)$  (first line, on the left), the probability distribution of the size of the largest cluster,  $P(n^*)$  (first line, on the right) and the free energy  $F(n^*)$  (second line) as function of the size of the largest cluster  $n^*$ . Those three plots are taken from the simulation run of figure 4.17 with the temperature  $T = 0.506$ .

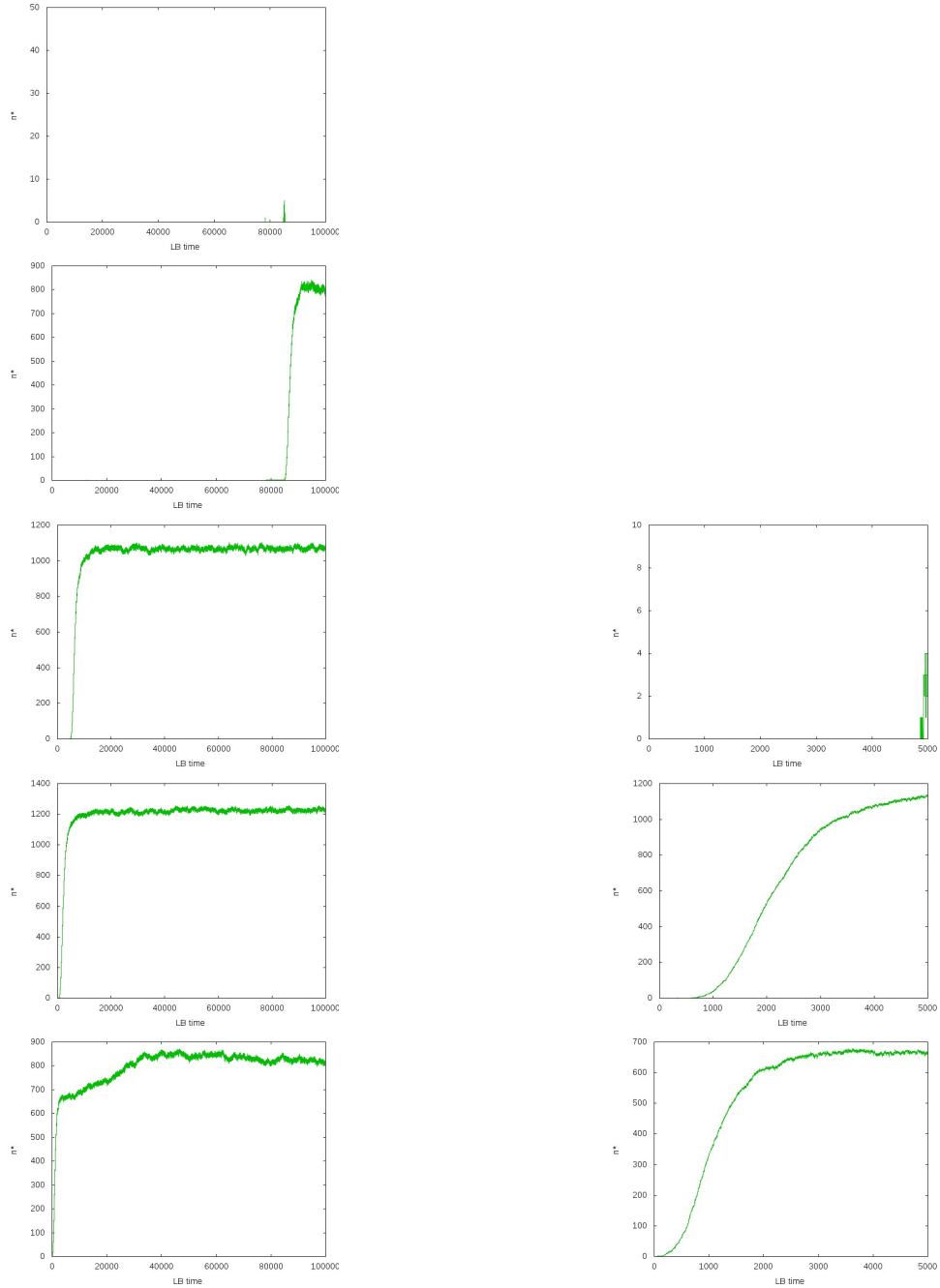


Figure 4.19: These plots show again the size of the biggest cluster as function of time at different temperatures  $T$  but with a smaller fluctuation amplitude,  $B_f = 0.005$ , than in figure 4.17. The surface tension coefficient has again the value  $\kappa = 0.01$ , and the mean density difference is  $\langle \phi \rangle = -0.4$ . Each line represents one temperature run plotted for different time intervals. first line:  $T = 0.508$ , second line:  $T = 0.507$ , third line:  $T = 0.504$ , fourth line:  $T = 0.502$ , fifth line:  $T = 0.500$ . The only difference between these plots and the plots in figure 4.17 is that here  $B_f$  is set to 0.008, whereas in figure 4.17  $B_f = 0.005$ .

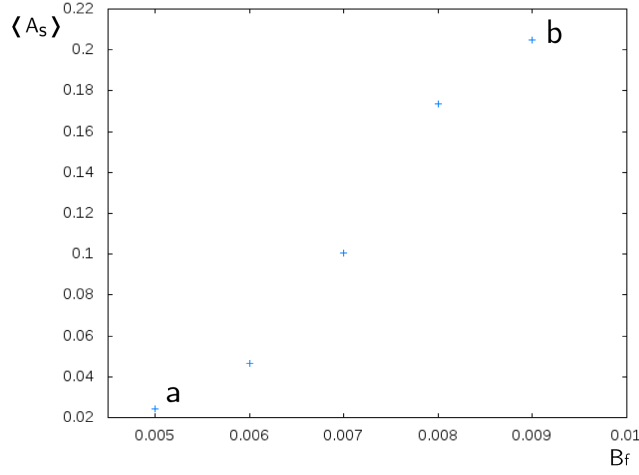


Figure 4.20: Dependency of the averaged asphericity  $\langle A_s \rangle$  on the amplitude of fluctuations  $B_f$ . For the indicated dots  $a$  and  $b$  snapshots of the density difference field  $\phi(\vec{x}, t)$  can be viewed in the figures below,  $a$  corresponds to figure 4.21,  $b$  corresponds to figure 4.22.

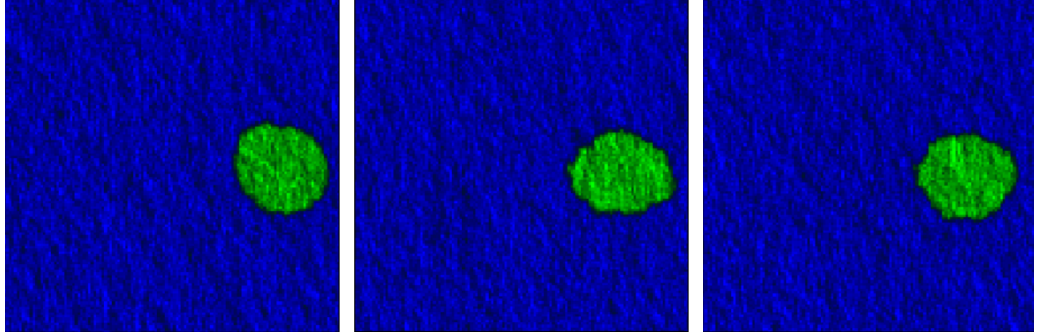


Figure 4.21: In this simulation the averaged asphericity is  $\langle A_s \rangle = 0.024$ . The other parameters are chosen to:  $B_f = 0.005$ ,  $\langle \phi \rangle = 0.3$ ,  $\kappa = 0.015$  and  $T = 0.524$ . The snapshots are taken at  $time = 10000, 40000, 70000$ .

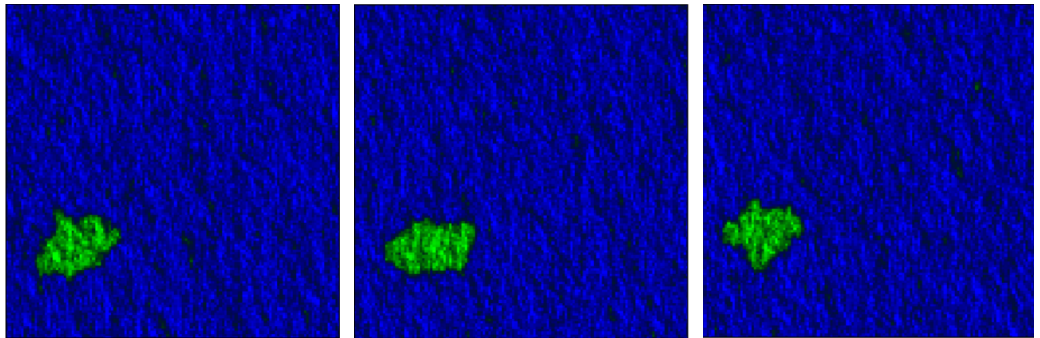


Figure 4.22: In this simulation the averaged asphericity is  $\langle A_s \rangle = 0.204$ . The other parameters are chosen to:  $B_f = 0.009$ ,  $\langle \phi \rangle = 0.3$ ,  $\kappa = 0.015$  and  $T = 0.523$ . The snapshots are taken at  $time = 10000, 40000, 70000$ .

---

this observation is that at  $\langle\phi\rangle = 0.3$ , the fluid mixture still contains more of the minor fluid than it contains at  $\langle\phi\rangle = 0.4$ . Therefore it is more likely that a cluster is formed when  $\langle\phi\rangle = 0.3$  than when  $\langle\phi\rangle = 0.4$ .

We first study simulations where the surface tension coefficient  $\kappa$  is set to 0.01 and the density difference is set to  $\langle\phi\rangle = 0.4$ . Note, that for all simulation runs, lattice length was again set to  $lx = 128$  and the mobility was set to  $\Gamma = 2.0$ .

We already treated the situation of intermediate fluctuation amplitude values, in the last paragraph where  $\kappa$  is set to 0.007 and  $B_f = 0.008$ : We observed small but frequently occurring fluctuations in  $n^*$  as well above as below the transition temperature. At the transition from nucleation to spinodal decomposition the transition time shifts to zero as the temperature is decreased until the phase transition starts at the beginning of the simulation. Next, we turn to analyse simulation runs where  $B_f$  is set to small values. Note that with decreasing  $B_f$  and fixed  $\langle\phi\rangle$  also the fluctuations in  $n^*$  decrease. At very small fluctuations, i.e for fluctuation amplitudes of  $B_f = 0.001$  or smaller, we do not observe nucleation at all, whereas spinodal decomposition still takes place.

At a fluctuation amplitude of  $B_f = 0.005$  fluctuations in  $n^*$  occur rarely and are small (see figure 4.19). Nevertheless, a transition occurs at the same temperature as at the presence of higher fluctuations, but at later times. Therefore, the situation at a low  $B_f$  and an intermediate  $\kappa$  is comparable with the situation of high  $\kappa$  and intermediate  $B_f$ : The fluctuations in  $n^*$  are suppressed and one of the first fluctuations drives the phase transition. Again, nucleation far from the spinodal is not really distinguishable from spinodal nucleation far from the spinodal.

Unfortunately, for  $B_f > 0.008$  and  $\langle\phi\rangle = 0.4$ , the algorithm becomes unstable, and therefore we cannot obtain results for the high fluctuation limit  $B_f > 0.008$  and  $\langle\phi\rangle$ .

Therefore, we set  $\langle\phi\rangle = 0.3$  and  $B_f = 0.008$ , where the fluctuations in  $n^*$  are higher than at  $\langle\phi\rangle = 0.4$  and subsequently we can study the case where the fluctuations in  $n^*$  are high. It turns out that at high effective fluctuations, we do not observe a nucleation process whereas spinodal decomposition still takes place (see figure 4.14 for illustration). The reason for this is that the fluctuations in  $n^*$  are so high that the clusters can cross the barrier easily, which effectively means that there is not really a barrier and therefore we only observe spinodal decomposition. Furthermore, we observe that the average asphericity of the clusters increases with the fluctuations in  $n^*$ . (see 4.20).

## 4.5 Summary

Now, we take the time to summarize and discuss the most important results obtained in section 4.4. The aim of the thesis in general and of the previous section in particular was to implement a fluctuating lattice Boltzmann model for binary fluids and determine whether nucleation is observed or not.

As a starting point, we used the models of ref. [54] and ref. [60] and included fluctuations according to ref. [20, 19].

After having successfully implemented the fluctuations into the binary fluid model, we analysed the results. Our main interest was thereby to distinguish the nucleation process from spinodal decomposition. For this purpose we investigated the dependence of the nucleation process on two parameters, the surface tension coefficient  $\kappa$  and the amplitude of the fluctuations  $B_f$ . Most importantly, we found out that the difference between nucleation and spinodal decomposition is most obvious at intermediate values of  $B_f$  and  $\kappa$ : Nucleation is then characterized by frequent fluctuations in the size of the largest cluster  $n^*$  until one cluster is large enough to cross the nucleation barrier and subsequently grows up to a certain size. spinodal decomposition, on the other hand, starts right at the beginning everywhere in the system, i.e., a couple of bubbles form distributed over the whole simulation domain. In the course of time, they grow by a Lifshitz-Slyozov mechanism and in the end, only one or two big bubbles remain.

At this point we remark that according to ref. [6] Landau theories in general suffer from problem that the spinodal line can not be obtained rigorously and therefore the transition from nucleation to spinodal decomposition occurs gradually in Landau theories. We also did observe this non-physical behaviour in the deterministic version of applied model (see section 4.2). In the fluctuating version, these crossover effects were still trackable but definitely weaker when the effective fluctuations were set to an intermediate value. At low effective fluctuations, on the other hand, the crossover effects were clearly visible. At high effective  $\kappa$  values, the development of clusters is suppressed and hence we observe no or very few small fluctuations in  $n^*$  and the first significant fluctuation in  $n^*$  leads to the transition. Hence, the only difference that remains at high effective  $\kappa$  values between spinodal decomposition and nucleation events far from the spinodal is that nucleation starts at a later times, whereas spinodal decomposition starts rather at the beginning. At low effective  $\kappa$  values or on the other hand, the the clusters cross the barrier at once and hence we only observe spinodal decomposition and no nucleation process.

These observations can be explained using classical nucleation theory. We start with remarking that  $\kappa$  is proportional to the surface tension, and the



---

numerical value of the surface tension sets the height of the nucleation barrier in classical nucleation theory. Subsequently, a higher  $\kappa$  yields a higher nucleation barrier and the higher the nucleation barrier is, the more difficult it becomes for clusters to cross the barrier or even to form in the first place. Finally we turn to the lower limit values of the parameters:

At very low  $\kappa$  no transition of any kind is observed as, due to the very small gradient terms, the binary fluid behaves like an homogeneous fluid. At very low  $B_f$  the system quasi falls back into the deterministic regime and we only observe spinodal decomposition.

Finally, we conclude that we successfully included fluctuations according to ref. [19] into the lattice Boltzmann model of [54]. In addition, we could demonstrate that the adapted algorithm is able to qualitatively model a nucleation process.



# Appendix A

## Zusammenfassung

Festkörper, Flüssigkeiten und Gase, welche aus zwei verschiedenen Arten von Molekülen, Kolloiden oder anderen Entitäten bestehen, werden unter dem Begriff binäre Materialien zusammengefasst.

Berühmte Beispiele für diese Klasse von Materialien sind binäre Legierungen, binäre Kolloide und Wasser-Öl-Mischungen. Diese Diplomarbeit befasst sich mit binären Flüssigkeiten, die nur unter bestimmten Temperaturen und Stoffmengenanteilen vermischbar sind. Wird die vermischte binäre Flüssigkeit etwa durch Temperaturänderung in einen Phasendiagramm-Bereich jenseits dieser Bedingungen gebracht, entmischt sie sich entweder durch spinodale Entmischung oder durch Keimbildung.

Bei einer spinodalen Entmischung bilden sich gleich nach der Temperaturänderung überall in der Flüssigkeit voneinander getrennte Bereiche der beiden Komponenten. Im Zuge des Phasenübergangs, wachsen diese getrennten Domänen weiter bis die Flüssigkeit vollständig separiert ist.

Bei einem Keimbildungsprozess hingegen, trennt eine Freie-Energie Barriere den aktuellen, metastabilen Zustand von dem entmischten Gleichgewichtszustand. Durch thermische Fluktuationen bilden sich kleine Keime der Komponente mit dem geringeren Stoffmengenanteil. Die meisten dieser Keime verschwinden allerdings wieder und nur wenn ein Keim die Größe erreicht, die notwendig ist um die Freie Energie Barriere zu überwinden, kann er weiterwachsen bis die binäre Flüssigkeit vollständig entmischt ist.

Das Ziel dieser Diplomarbeit ist es ein Lattice-Boltzmann-Modell für den Keimbildungsprozess in binären Flüssigkeiten zu erstellen und zu analysieren. Als Ausgangspunkt verwenden wir das Lattice-Boltzmann-Modell für spinodale Entmischung von Swift et al. [54]. Da Keimbildung ein Fluktuations-induzierter Phasenübergang erster Ordnung ist, inkludieren wir thermische Fluktuationen nach dem Verfahren von Dünweg [19]. Die mit dem so veränderten Algorithmus erzielten Simulationsergebnisse zeigen dass es möglich ist, mit

der mesoskopischen Lattice-Boltzmann-Methode Nukleationsprozesse von binären Flüssigkeiten zu modellieren.

# Appendix B

## Abstract

Condensed matter materials, which are composed of two different species of molecules, colloids or other entities, are widely known as binary materials. Binary alloys, binary colloids and water-oil-mixtures are prominent examples for this class of materials. In this thesis we deal with binary fluids that are miscible under certain temperatures and mole-fractions only. Beyond those temperatures and mole-fractions, these fluids will unmix.

This phase separation transition then proceeds either via spinodal decomposition or via nucleation. When undergoing spinodal decomposition, the binary fluid exhibits a characteristic coarsening behaviour. Shortly after the finite temperature quench from the mixed state, distinct domains of the different species form. After this initial phase separation, the domains start to grow until the fluid is fully phase separated.

On the other hand, when undergoing a nucleation process, a free energy barrier separates the actual state of the fluid from the phase separated equilibrium state. We observe that, due to thermal fluctuations, small droplets of the species with the minor mole-fraction appear now and then. Most of them will vanish again. Only if one droplet manages to cross the free energy barrier, it starts to grow until the fluid is separated.

The aim of this thesis is to model the nucleation process of a binary fluid with the lattice Boltzmann method. As starting point we use the lattice Boltzmann model of a binary fluid of ref. [54]. Since nucleation is a fluctuation induced process, thermal fluctuations need to be included into the binary fluid model. This is done by implementing the fluctuating lattice Boltzmann algorithm introduced by ref. [20]. Having successfully included fluctuations into the binary fluid model, we could demonstrate that the new algorithm is able to qualitatively model a nucleation process.



# Appendix C

## Curriculum Vitae

### Personal Information

Name: Carina Natalia Karner  
Current Address: Favoritenstraße 119/2/9, 1100 Wien, Austria  
Date and place of birth: 29 January 1987, Scheibbs (Austria)

### Education

2005 Matura, Realgymnasium Waidhofen/Ybbs (with Distinction)  
2005-2011 University of Vienna, Physics Diploma, expected in May 2011, Diploma Thesis: "Lattice Boltzmann Simulation of Nucleation in Binary Fluids"

### Working Experience

2007-2008 Tutor for Analysis for Physicists  
2008-2009 Tutor for Linear Algebra for Physicists  
2007-2011 Active member of the Austrian Student Union  
2009-2010 Intern-ship at the Austrian Institute of Technology, numerical modelling for applied fluid mechanical problems

### Research Interests

Theoretical and Computational Condensed Matter Physics





# Bibliography

- [1] R. Adhikari, K. Stratford, M.E. Cates, and A.J. Wagner. Fluctuating lattice Boltzmann. *Europhysics Letters*, 71:473–479, 2005.
- [2] F. Bai, C. M. Elliott, A. Spence, and A.M. Stuart. The viscous Cahn-Hilliard equation.i.computations. *Nonlinearity*, 8:131–160, 1995.
- [3] J.L. Barrat and J.P. Hansen. *Basic Conepts for Simple and Complex Liquids*. Cambridge University Press, 2003.
- [4] J.W Barrett, J.F. Blowey, and H. Garcke. Finite element approximation of the Cahn-Hilliard equation with degenerate mobility. *SIAM Journal on Numerical Analysis*, 37(1):286–318, 1999.
- [5] K. Binder. *Systems far from Equilibrium*, volume 132 of *Lecture Notes in Physics*. Springer Berlin/Heidelberg, 1980.
- [6] K. Binder. Nucleation barriers, spinodals, and the Ginzburg criterion. *Phys. Rev. A*, 29(1):341–, January 1984.
- [7] K. Binder. Theory of first-order phase transitions. *Rep. Prog. Phys.*, 50:783–859, 1987.
- [8] J.J. Binney, N.J Dowrick, A.J. Fisher, and M.E.J. Newman. *The Theory of Critical Phenomena*. Clarendon Press/Oxford, 1992.
- [9] J. F. Blowey and C. M. Elliott. The Cahn-Hilliard gradient theory for phase separation with non-smooth free energy part i: Mathematical analysis. *European Journal of Applied Mathematics*, 2(03):233–280, 1991.
- [10] P.G. Bolhuis, D. Chandler, C. Dellago, and P.L. Geissler. Transition path sampling: throwing ropes over rough mountain passes, in the dark. *Annu Rev Phys Chem*, 53:291–318–, 2002.

- [11] A. B. Bortz, M. H. Kalos, J. L. Lebowitz, and M. A. Zendejas. Time evolution of a quenched binary alloy: Computer simulation of a two-dimensional model system. *Phys. Rev. B*, 10(2):535–541, Jul 1974.
- [12] J.W. Cahn. Free energy of a nonuniform system. ii. thermodynamic basis. *The Journal of Chemical Physics*, 30(5):1121–1124, 1959.
- [13] J.W. Cahn and J.E. Hilliard. Free energy of a nonuniform system. i. interfacial free energy. *The Journal of Chemical Physics*, 28(2):258–267, 1958.
- [14] J.W. Cahn and J.E. Hilliard. Free energy of a nonuniform system. iii. nucleation in a two-component incompressible fluid. *The Journal of Chemical Physics*, 31(3):688–699, 1959.
- [15] C. Cercignani. *The Boltzmann Equation and its Applications*. Springer-Verlag, 1975.
- [16] J. Chin and P. V. Coveney. Lattice boltzmann study of spinodal decomposition in two dimensions. *Phys. Rev. E*, 66(1):016303, Jul 2002.
- [17] M. I. M. Copetti and C. M. Elliott. Numerical analysis of the cahn-hilliard equation with a logarithmic free energy. *Numerische Mathematik*, 63:39–65, 1992. 10.1007/BF01385847.
- [18] D. d’Humières. Multiple-relaxation-time lattice boltzmann models in three dimensions. *Philosophical Transactions of the Royal Society of London. Series A:Mathematical, Physical and Engineering Sciences*, 360(1792):437–451, March 2002.
- [19] B. Dünweg and A.J.C. Ladd. Lattice boltzmann simulations of soft matter systems. *Advances in Polymer Science*, 221:89, 2009.
- [20] B. Dünweg and U.D Schiller. Statistical mechanics of the fluctuating lattice boltzmann equation. *Phys.Rev. E*, 76, 2007.
- [21] P. Ehrenfest. Phasenumwandlungen im ueblichen und erweiterten Sinn, classifiziert nach dem entprechenden Singularitaeten des thermodynamischen Potentials. *Communications from the Physical Laboratory of the University of Leiden*, 36:153–157, 1933.
- [22] C. M. Elliott and D.A. French. Numerical studies of the Cahn-Hilliard equation for phase separation. *IMA Journal of Applied Mathematics*, 38(2):97–128, 1987.

- 
- [23] C. M. Elliott and Z. Songmu. On the Cahn-Hilliard equation. *Archive for Rational Mechanics and Analysis*, 96:339–357, 1986. 10.1007/BF00251803.
  - [24] Charles M. Elliott and Harald Garcke. On the Cahn-Hilliard equation with degenerate mobility. *SIAM Journal on Mathematical Analysis*, 27(2):404–423, 1996.
  - [25] W. Grimus. *Einführung in die statistische Physik und Thermodynamik*. Oldenbourg Verlag München, 2010.
  - [26] Dieter W. Heermann. Test of the validity of the classical theory of spinodal decomposition. *Phys. Rev. Lett.*, 52(13):1126–1128, Mar 1984.
  - [27] C.H. Hung, M.J. Krasnopoler, and J.L. Katz. Condensation of a supersaturated vapor. viii. the homogeneous nucleation of n-nonane. *The Journal of Chemical Physics*, 90(3):1856–1865, 1989.
  - [28] E.T. Jaynes. Violation of Boltzmann’s H-theorem in real gases. *Phys. Rev. A.*, 4:747–750, 1971.
  - [29] J. Julin, I. Napari, J. Merikanto, and H. Vehkamäki. Equilibrium sizes and formation energies of small and large lennard-jones clusters from molecular dynamics: A consistent comparison to monte carlo simulations and density functional theories. *The Journal of Chemical Physics*, 129(23):234506, 2008.
  - [30] V. I. Kalikmanov, J. Wolk, and T. Kraska. Argon nucleation: Bringing together theory, simulations, and experiment. *The Journal of Chemical Physics*, 128(12):124506, 2008.
  - [31] G. Kremer. *An Introduction to the Boltzmann Equation and Transport Processes in Gases*. Springer, 2010.
  - [32] J. Marro, A. B. Bortz, M. H. Kalos, and J. L. Lebowitz. Time evolution of a quenched binary alloy. ii. computer simulation of a three-dimensional model system. *Phys. Rev. B*, 12(6):2000–2011, Sep 1975.
  - [33] A. Milchev, D.W. Heermann, and K. Binder. Monte-carlo simulation of the Cahn-Hilliard model of spinodal decomposition. *Acta metallurgica*, 36:377–383, 1988.
  - [34] A. Miranville. Some generalizations of the Cahn-Hilliard equation. *Asymptotic Analysis*, 22(3):235–259, January 2000.

- [35] G. Mussardo. *Statistical Field Theory*. Oxford University Press, 2010.
- [36] M. Nekovee, P. V. Coveney, H. Chen, and B. M. Boghosian. Lattice Boltzmann model for interacting amphiphilic fluids. *Phys. Rev. E*, 62(6):8282–8294, Dec 2000.
- [37] A. Novick-Cohen. *Handbook of Differential Equations*, chapter 4, pages 201–228. Elsevier, 2008.
- [38] A. Novick-Cohen and L.A. Segel. Nonlinear aspects of the Cahn-Hilliard equation. *Physica D: Nonlinear Phenomena*, 10(3):277 – 298, 1984.
- [39] R.M. Nyquist, V. Talanquer, and D.W. Oxtoby. Density-functional theory of nucleation - a semiempirical approach. *Journal of Chemical Physics*, 103(3):1175–1179, 1995.
- [40] J. Orban and A. Bellemans. Velocity-inversion and irreversibility in a dilute gas of hard disks. *Physics Letters A*, 24(11):620 – 621, 1967.
- [41] D. W. Oxtoby. Nucleation of first-order phase transitions. *Accounts of Chemical Research*, 31(2):91–97, 1998.
- [42] D.W Oxtoby. Homogenous nucleation: theory and experiment. *Journal of Physics: Condensed Matter*, 4:7627–7650, 1992.
- [43] F. Peters and B. Paikert. Experimental results on the rate of nucleation in supersaturated n-propanol, ethanol, and methanol vapors. *The Journal of Chemical Physics*, 91(9):5672–5678, 1989.
- [44] R. Racke and S. Zheng. The Cahn-Hilliard equation with dynamic boundary conditions. *Advances Di. Equations*, 8:8–83, 2001.
- [45] L.E. Reichl. *A Modern Course in Statistical Physics*. John Wiley & Sons, Inc., 1998.
- [46] H. Reiss, J. L. Katz, and E. R. Cohen. Translation-rotation paradox in the theory of nucleation. *The Journal of Chemical Physics*, 48(12):5553–5560, 1968.
- [47] D. Rothman and S. Zaleski. *Lattice-Gas Cellular Automata*. Cambridge University Press, 1997.
- [48] M.M. Rudek, J.L. Katz, and H. Uchtmann. Homogeneous nucleation of supersaturated cesium vapor. *The Journal of Chemical Physics*, 110(23):11505–11510, 1999.

- 
- [49] J. Rudnick and G. Gaspari. The aspheringity of random walks. *Journal of Physics A: Mathematical and General*, 19:191–193, 1986.
  - [50] F. Schwabl. *Statistische Mechanik*. Springer Berlin/ Heidelberg/ New York, 2000.
  - [51] F.H. Stillinger. Rigorous basis of the Frenkel-Band theory of association equilibrium. *The Journal of Chemical Physics*, 38(7):1486–1494, 1963.
  - [52] R. Strey, P. E. Wagner, and T. Schmeling. Homogeneous nucleation rates for n-alcohol vapors measured in a two-piston expansion chamber. *The Journal of Chemical Physics*, 84(4):2325–2335, 1986.
  - [53] S. Succi. *The Lattice Boltzmann Equation*. Clarendon Press Oxford, 2001.
  - [54] M. Swift, E. Orlandini, W.R. Osborn, and J.M Yeomans. Lattice Boltzmann simulations of liquid-gas and binary fluid systems. *Phys.Rev.*, E 54:5041–5052, 1996.
  - [55] V. Talanquer and D.W. Oxtoby. Dynamical density-functional theory of gas-liquid nucleation. *Journal of Chemical Physics*, 100(7):5190–5200, 1994.
  - [56] G. M. Torrie and J. P. Valleau. Nonphysical sampling distributions in monte carlo free-energy estimation: Umbrella sampling. *Journal of Computational Physics*, 23(2):187–199, February 1977.
  - [57] Y. Viisanen, R. Strey, and H. Reiss. Homogeneous nucleation rates for water. *The Journal of Chemical Physics*, 99(6):4680–4692, 1993.
  - [58] C. Villani. *Handbook of Mathematical Fluid Dynamics, Vol.1*, chapter 2, pages 71–258. Elsevier, 2002.
  - [59] C. von Ferber, J. Y. Monteith, and M. Bishop. Shapes of two-dimensional excluded volume continuum star polymers. *Macromolecules*, 42(10):3627–3631, 2009.
  - [60] A. J. Wagner. *Theory and Applications of the Lattice Boltzmann Method*. PhD thesis, University of Oxford, 1997.
  - [61] A. J. Wagner and J. M. Yeomans. Breakdown of scale invariance in the coarsening of phase-separating binary fluids. *Phys. Rev. Lett.*, 80(7):1429–1432, Feb 1998.

- [62] P. E. Wagner and R. Strey. Measurements of homogeneous nucleation rates for n-nonane vapor using a two-piston expansion chamber. *The Journal of Chemical Physics*, 80(10):5266–5275, 1984.
- [63] J. Wei and M. Winter. Stationary solutions for the Cahn-Hilliard equation. *Annales de l'Institut Henri Poincaré (C) Non Linear Analysis*, 15(4):459 – 492, 1998.
- [64] A. Wolf-Gladrow. *Lattice Gas Cellular Automata and Lattice Boltzmann Models - an Introduction*. Springer, 2000.